

Fiber Amplifiers for Gravitational Wave Detectors: Temporal Dynamics and Coherent Beam Combining

Der Fakultät für Mathematik und Physik
der Gottfried Wilhelm Leibniz Universität Hannover
zur Erlangung des Grades
Doktor der Naturwissenschaften
Dr.rer.nat.
genehmigte Dissertation

von
Dipl.-Phys. Henrik Tünnermann
geboren am 06.12.1984 in Hannover

2013

Referent: Prof. Dr. Karsten Danzmann
Korreferenten: Prof. Dr. Uwe Morgner
Prof. Dr. Akira Shirakawa
Tag der Promotion: 04.02.2013

Abstract

Compact single frequency fiber amplifiers with superior efficiency will potentially supersede the bulk laser systems currently in use in gravitational wave detectors (GWDs). To realize high power fiber amplifiers with low noise, active stabilization is required. For an effective stabilization, a good comprehension of the amplifier's dynamic properties is necessary. Therefore, the temporal dynamics of single frequency fiber amplifiers and coherent beam combination are investigated in this thesis.

Knowledge of the frequency dependent amplification of signal and pump power fluctuations is essential for power stabilization of fiber amplifiers. These dynamic processes were modeled by means of the time dependent laser rate equations. The impact of the amplifier parameters was analyzed and the obtained results were confirmed with experimental data. Furthermore, it was shown that this dynamic model can be applied to determine the power noise of the amplified signal from the input power noise.

For interferometric precision measurements the signal phase is even more significant, as phase noise directly couples to the phase signal of the interferometer. The signal phase of a fiber amplifier also depends on the pump and seed power due to thermal effects and the frequency dependent gain. Since the refractive index of glass depends on the temperature, the fiber temperature influences the signal phase. In the frequency range from 2-1000 Hz the temperature induced phase shift was shown to be strongly influenced by the radial heat flow, while at the low frequencies the average temperature change is the dominating effect. The gain of the fiber amplifier changes the signal phase because of the Kramers-Kronig-Relations (KKR). It was shown that the temporal dynamics of this KKR phase shift can be described with the dynamic fiber amplifier model developed for power modulation. Both heat diffusion and KKR effects were observed in the investigated fiber amplifiers, therefore the prominence of each process depends on the fiber amplifier parameters.

Since power scaling of single amplifiers might not be sufficient to realize the high power single frequency sources required for 3rd generation GWDs, the prospects of relative phase stabilization – or coherent beam combination – as a power scaling method was analyzed. Two fiber amplifiers with an output power of 10 W each were combined in free space with diffraction limited beam quality. The power noise and frequency noise could also be preserved. Therefore, it could be shown that coherent beam combining is a very promising power scaling method to reach the high power levels required for third generation GWDs.

All-fiber coherent beam combining was realized as well. Using fiber stretchers as phase actuators a long term stable system could be demonstrated. Furthermore, it was shown that the phase shifting properties of fiber amplifiers can also be used as a phase actuator for coherent beam combining. In this way coherent beam combining of two 10 W ytterbium amplifiers without a dedicated phase actuator was demonstrated for the first time.

Keywords: Lasers, fiber amplifiers, laser stabilization, coherent beam combining

Kurzzusammenfassung

In Zukunft werden kompakte Faserverstärker mit besserer Effizienz die derzeit in Gravitationswellendetektoren (GWDs) verwendeten Festkörperlaser ersetzen. Um einfrequente Faserverstärker mit hoher Ausgangsleistung und niedrigem Rauschen zu realisieren, wird eine aktive Stabilisierung benötigt. Für diese aktive Stabilisierung ist ein gutes Verständnis der dynamischen Eigenschaften von Faserverstärkern notwendig. Deshalb werden in dieser Arbeit die zeitliche Dynamik von einrequenten Faserverstärkern und deren kohärente Kopplung untersucht.

Die Kenntnis der frequenzabhängigen Verstärkung von Signal- und Pumpleistungsfluktuationen ist essentiell für die Leistungsstabilisierung von Faserverstärkern. Diese dynamischen Prozesse wurden anhand der zeitabhängigen Laserratengleichungen modelliert. Der Einfluss der Verstärkerparameter wurde analysiert und durch experimentelle Daten bestätigt. Außerdem konnte gezeigt werden, dass dieses dynamische Modell verwendet werden kann, um aus dem Eingangsleistungsrauschen das Leistungsrauschen des verstärkten Signals zu bestimmen.

Für interferometrische Präzisionsmessungen ist die Signalphase sogar noch bedeutender, weil das Phasenrauschen direkt in das Phasensignal des Interferometers koppelt. Die Signalphase eines Faserverstärkers hängt aufgrund thermischer Effekte und der frequenzabhängigen Verstärkung ebenfalls von der Pump- und Seedleistung ab. Die Temperatur beeinflusst die Signalphase, weil der Brechungsindex von Glas von der Temperatur abhängt. Es konnte gezeigt werden, dass im Frequenzbereich von 2-1000 Hz die radiale Wärmeleitung eine wichtige Rolle spielt, während bei niedrigen Frequenzen die Veränderung der mittleren Fasertemperatur dominiert. Die frequenzabhängige Verstärkung verändert aufgrund der Kramers-Kronig-Relationen (KKR) ebenfalls die Signalphase. Die Dynamik dieser KKR-induzierten Phasenverschiebung konnte mit dem dynamischen Verstärkermodell beschrieben werden, das für die Leistungsmodulation entwickelt wurde. Sowohl thermische als auch KKR-Effekte wurden in den untersuchten Faserverstärkern beobachtet; daher ist es von den Verstärkerparametern abhängig, welcher Prozess dominiert.

Die mit einem einzelnen Faserverstärker erreichbare Ausgangsleistung ist möglicherweise nicht ausreichend für die GWDs der dritten Generation. Deshalb wurde die Leistungskalierung durch relative Phasenstabilisierung – oder kohärente Kopplung – mehrerer Faserverstärker untersucht. Zwei Faserverstärker mit einer Ausgangsleistung von je 10 W wurden mit Freistrahloptiken kombiniert. Dabei wurde beugungsbegrenzte Strahlqualität erreicht. Leistungs- und Frequenzrauschen blieben bei der Kombination ebenfalls erhalten. Daher konnte gezeigt werden, dass kohärente Kopplung eine vielversprechende Methode ist, um die benötigten Ausgangsleistungen für GWDs der dritten Generation zu erreichen.

Eine komplett faserbasierte kohärente Kopplung wurde ebenfalls realisiert. Langzeitstabilität wurde dabei mit Hilfe von Faserstreckern erreicht. Weiterhin konnte gezeigt werden, dass Faserverstärker als Phasenaktuatoren für kohärente Kopplung verwendet werden können. Auf diese Weise wurden erstmals zwei Ytterbium-Verstärker ohne einen dedizierten Phasenaktuator kombiniert.

Schlagwörter: Laser, Faserverstärker, Laserstabilisierung, kohärente Kopplung

Contents

1	Introduction	1
2	Lasers for Gravitational Wave Detectors	5
2.1	Bulk Lasers	5
2.2	Single Frequency Fiber Amplifiers	6
2.2.1	Noise and Temporal Dynamics of Fiber Amplifiers	7
2.2.2	Power Scaling	8
2.3	Coherent Beam Combining	11
3	Time Dependent Fiber Amplifier Model	15
3.1	Rate Equations	15
3.2	Analytic Model	18
3.3	Large Output Power Approximation	25
3.4	Design Guidelines	28
4	Experimental Results: Power Modulation	29
4.1	Erbium Doped Fiber Amplifier	29
4.2	Ytterbium Doped Fiber Amplifier	34
4.3	Summary	38
5	Power Noise	39
5.1	Power Noise of a Single Amplifier	40
5.1.1	Pump and Seed Noise	40
5.1.2	Low Power	42
5.1.3	High Power	45

5.2	Power Noise of Coherently Combined Beams	49
5.3	Summary	52
6	Phase Modulation	53
6.1	Phase Shift Induced by Kramers-Kronig-Relations	53
6.1.1	Erbium Fiber Induced Phase Shift at 1064 nm	55
6.1.2	Ytterbium Fiber Induced Phase Shift: Frequency Domain	61
6.2	Temperature Induced Phase Shift	64
6.2.1	Heat Diffusion in Fibers	65
6.2.2	Experimental Results	71
6.3	Summary	73
7	Collinear Coherent Combining of Two 10 W Fiber Amplifiers	75
7.1	Setup	76
7.2	Beam Quality	78
7.3	Power and Frequency Noise	79
7.4	Summary	82
8	All-Fiber Coherent Beam Combining	85
8.1	Erbium Doped Fiber Amplifier as a Phase Actuator at 1064 nm	86
8.2	All-Fiber CBC at Medium Power	89
8.3	Summary	98
9	Conclusion	99
10	Outlook	101
	Bibliography	105
	Publications in Peer-Reviewed Journals	115
	Publications in Conference Proceedings	117

1 Introduction

Interferometric gravitational wave detectors (GWDs) are able to detect small relative distance changes by means of a Michelson interferometer. Gravitational waves cause a strain in space as they pass, resulting in a relative length change of the interferometer arms which can then be measured. However, because the gravitational force is weak and the expected length changes are very small, a very high sensitivity is required. Since 2011, the 2nd generation GWDs advanced LIGO [1], advanced VIRGO and LCGT [2] are being assembled. Once these second generation detectors operate at their design strain sensitivity of $3 \cdot 10^{-24} \text{Hz}^{-1/2}$ at 100-1000 Hz, the first direct observation of a gravitational wave can be expected within a year.

Subsequent analysis of gravitational waves (GWs) will open an additional view on the universe. However, for precise astronomical studies, the signal to noise ratio of even the advanced detectors will not be sufficient. This is why even more sensitive detectors are planned. These 3rd generation detectors target a sensitivity improvement by factor of ten. To reach this goal, the experience from current and advanced detectors will be combined with further technology improvements. One fundamental limitation of GWDs is the quantum limit, which is given by shot noise for high frequencies and radiation pressure noise at low frequencies. The error caused by shot noise increases with the root of the optical power P , while the signal increases linearly with the power. Therefore, the relative error caused by shot noise is proportional to $1/\sqrt{P}$. Consequently, increasing the power in the interferometer with techniques such as signal recycling, power recycling [1] and more powerful lasers [3, 4] is an effective means to increase the sensitivity at high frequencies. To reduce the impact of thermal noise, which is yet another limitation in the low frequency region, the mirror substrates can be cooled to cryogenic temperatures. At these

temperatures the thermo-optical properties of crystalline silicon are much superior to the properties of silica. Therefore, a change to silicon substrates is in discussion for 3rd generation GWDs as well. However, this will also require the operating wavelength to be changed from 1064 nm to 1.5 – 2 μm .

Currently, there are several possible optical designs for 3rd generation GWDs in discussion and most of them require a new single frequency laser source. Two of them are described in the design study of the European 3rd generation detector, the Einstein Telescope (ET) [5, 6]. The ET-HF interferometer, which is designed for high sensitivity at high frequencies, allots 500 W at 1064 nm in the circular LG₃₃ mode. Due to losses of filter cavities, external stabilization and mode conversion losses, about 1 kW of power in the fundamental mode (TEM₀₀) will be required at the output of the laser. Additionally, the ET-LF interferometer, which is designed for a high sensitivity at low frequencies, will switch to cryogenically cooled silicon substrates and therefore requires a laser source operating at 1.55 μm . One of three possible 3rd generation LIGO designs requires up to 600 W at 1.55 μm or alternatively in the 2 μm region.

Regardless of the finalized detector design, it is quite clear that there is demand for even higher laser power than in second generation detectors. Fiber amplifiers offer significant improvements in terms of efficiency and system complexity compared to the bulk solid state laser systems, which are currently in use. Because of yearlong experience with these systems, the impact of external noise is quite well known for bulk lasers and their stabilization is quite mature. On the other hand the dynamics of fiber amplifiers is not as well explored. Additionally, the very high output power levels combined with the high long term stability required for 3rd generation GWDs have not been demonstrated by one single frequency fiber amplifier, yet. Hence, alternative power scaling methods are of great interest. Therefore, to realize the full potential of fiber amplifiers for 3rd generation GWDs in the future these two topics should be addressed.

Consequently, the impact of external influences on a fiber amplifier's output power and optical phase were analyzed within the framework of this thesis. Since relative phase stabilization of two or more fiber amplifiers can also be used to coherently

combine the output power, this offers a promising way to overcome the limitations of a single fiber amplifier and thus the suitability of this approach for laser systems for gravitational wave detectors was investigated as well.

The next chapter reviews the state of the art laser systems for GWDs and continues to discuss the prospects and challenges of single frequency fiber amplifiers and coherent beam combining (CBC) for gravitational wave detectors.

In chapter 3 the transfer of pump and seed power fluctuations to fiber amplifier output power is modeled theoretically and the results are related to easily accessible amplifier parameters. The results are then compared with experimental data obtained from core pumped fiber amplifiers in chapter 4.

Based on the relative pump power noise and relative seed power noise the amplifier's relative power noise (RPN) is calculated and compared with the measured RPN in chapter 5. Additional noise sources in high power amplifiers are discussed as well. Finally, the power noise of coherently combined beams in case of perfect phase stabilization and the impact of the phase control loop on the relative power noise of the combined beam is described.

The impact of fiber amplifiers on the optical phase of the signal beam is analyzed in chapter 6. Here, the impact of temporally varying gain and the heat deposited in the fiber are analyzed theoretically and experimentally.

In chapter 7 coherent combination of two ytterbium doped fiber amplifiers with an output power of 10 W each is presented. This prototype system is used to analyze the output beam quality and noise with respect to the requirements for gravitational wave detectors and to learn about possible challenges.

Several roads towards all-fiber CBC are explored in chapter 8. Since CBC requires active phase stabilization, the phase shift induced by fiber amplifiers can also be used, if the influence can be controlled properly. This approach is an alternative to classical phase actuators such as electro-optic modulators (EOMs), acousto-optic modulators (AOMs), mirrors mounted on piezo-electric transducers, and piezo based fiber stretchers. It is truly all fiber and completely avoids mechanical parts and high voltage sources and therefore potentially enables very simple CBC systems. It also illustrates the practical use of the results from chapter 6.

Finally, in chapters 9 and 10 the thesis is summarized and an outlook on possible future developments and experiments is given.

2 Lasers for Gravitational Wave Detectors

In GWDs only the power in the fundamental mode can be used¹. For this reason, the laser sources for GWDs are required to deliver diffraction limited beam quality. Additionally, very low power noise and frequency noise is required. Typically, single frequency laser sources with a free running linewidth of about 1 kHz are used and further stabilized.

In the following introduction a brief overview of bulk laser systems currently in use in GWDs is given. In the following section the prospects and limitations of fiber amplifiers are discussed. Finally, an introduction to coherent beam combining is given.

2.1 Bulk Lasers

So far the laser systems for gravitational wave detectors have been realized by bulk solid state lasers. Typically, a frequency stable low noise non-planar ring oscillator (NPRO) is used as a master laser and locked to a high power oscillator [7–9]. By this approach the favorable NPRO properties can be combined with high power operation. This principle was maintained in the laser system for advanced LIGO, the current state of the art laser system for GWDs [3, 10]. It combines a Nd:YVO₄ amplifier [11] injection locked to a Nd:YAG ring oscillator, which achieves a power level of 220 W. The output power is stabilized externally to make the system suitable for advanced LIGO [4].

¹ In ET-HF LG₃₃ will be used instead, however, direct generation of a pure LG₃₃ in a laser or amplifier is more difficult than amplification of a TEM₀₀ beam and subsequent conversion.

While injection locked lasers could theoretically be scaled further by using more laser crystals per resonator, they would become intolerably difficult to align in practice. This issue can be overcome with amplifiers. Effectively, an amplifier is similar to an injection locked laser, but with the important difference that there is no resonator used and therefore there is no slave laser oscillator. This decreases the optical power in the gain material and therefore amplifiers tend to require more seed power for efficient operation. Especially when Nd:YAG is used as a gain medium, very high seed power is required. On the other hand Nd:YVO₄ crystals can overcome this issue at the expense of lower damage thresholds. Therefore, at low output power Nd:YVO₄ amplifiers eventually replaced the injection locked lasers. Nowadays for output powers up to 40 W, a Nd:YVO₄ based four stage amplifier system [11] is most commonly used in GWDs. A solid state amplifier chain consisting of Nd:YVO₄ and Nd:YAG demonstrated a performance roughly comparable to the advanced LIGO laser [12]. While there is little reason to doubt that given enough crystals and pump power high power could be reached in such systems, the efficiency, complexity and footprint of such systems is unsatisfactory.

2.2 Single Frequency Fiber Amplifiers

On the other hand fiber amplifiers have shown that they can be very compact and very efficient. State of the art single frequency fiber amplifiers compete with the advanced LIGO system in terms of output power and beam quality at reduced size and system complexity [13, 14]. Their optical-to-optical efficiencies can reach more than 70%. Therefore, fiber amplifiers are currently the most efficient way to realize the high brightness single frequency sources required for 3rd generation GWDs. However, compared to the well understood bulk systems, they also introduce new challenges.

2.2.1 Noise and Temporal Dynamics of Fiber Amplifiers

For GWDs the noise properties of a laser system are a prime concern. The stability required for GWDs cannot be met by free running lasers or master laser power amplifier (MOPA) systems. Therefore, active stabilization is required in any case. However, this does not mean the free running noise properties are negligible as higher noise levels also mean higher requirements for the active control loop.

One of the most important building blocks for active power and phase stabilization is an appropriate actuator. For the power stabilization of the advanced LIGO laser, this is realized by an external acousto-optic modulator (AOM). The AOM allows the control loop to dump a variable fraction of the total power so the power can be stabilized. This approach constantly wastes output power and whenever possible alternative actuation methods would be preferred. In the case of a fiber amplifier this could potentially be realized by feedback to the pump diodes. While this system still needs a dynamic power reserve, this approach increases the optical-to-optical efficiency and does not require the additional AOM. However, usage of the amplifier pump power in a feedback loop requires detailed knowledge of the dynamic system behavior.

The dynamic system behavior was measured for an exemplary amplifier by Tröbs et al. [15]. However, a general description would be desirable and is probably possible using a time dependent model originally developed for telecom amplifiers by Novak et al. [16]. Combination of these results should be a good starting point to relate fiber amplifier parameters like pump power, seed power and output power to their dynamic behavior.

Since laser beams are electromagnetic waves, there can not only be power (or magnitude) but also phase fluctuations. These are even more important for lasers used in precision interferometers, as phase noise will directly couple to the phase signal of the interferometer. Fiber amplifiers can change the optical phase due to mechanical noise and because of thermal and gain effects. There have been measurements of the phase noise added by fiber amplifiers [17]. The coupling mechanisms were partly investigated in the time domain [18–20] but in the frequency domain, especially the frequency range relevant for GWDs (1 Hz to 10 kHz), these dynamic processes

were not analyzed yet. A brief overview of the coupling mechanisms, which are of particular interest, is shown in Fig. 2.1.

2.2.2 Power Scaling

The third generation GWDs will require extremely high single frequency laser power. A few years ago this did not seem to be a major obstacle for future fiber amplifiers but in more recent experiments it proved to be more challenging than originally anticipated. After single frequency fiber amplifiers were first introduced, their output power levels increased very rapidly. From only of 5.5 W in 1998 [21], a massive increase of the output power was reported by many groups [22–24] over the next few years, leading to up to 500 W in 2007 [25, 26] (Fig. 2.2). At this power level the exponential growth stopped and promising new fiber concepts such as photonic crystal fibers [27] or chirally-coupled core (CCC) fibers [28] were so far only able to match this output power.

On the other hand broadband diffraction limited multi kilowatt fiber laser systems are available commercially today [30]. This discrepancy is caused by Stimulated Brillouin Scattering (SBS), which is caused by inelastic scattering of the signal photons with acoustic phonons [31]. The most successful way to increase SBS thresholds of fiber amplifiers is linewidth broadening, which is obviously not an option for single frequency fiber amplifiers. Therefore, other techniques have to be used.

Since SBS is a nonlinear effect, it can be suppressed efficiently by increasing the fiber core and therefore modefield diameter. This requires the numerical aperture (NA) to be lowered to maintain single transversal mode operation. In standard step

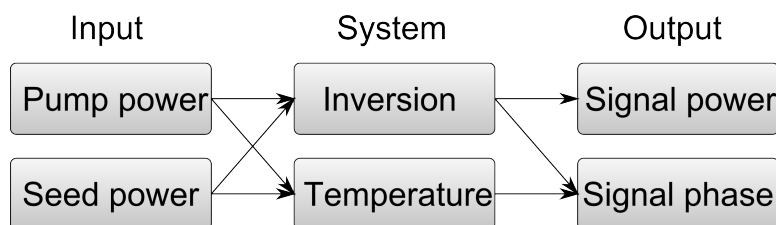


Figure 2.1: Coupling mechanisms in a fiber amplifier.

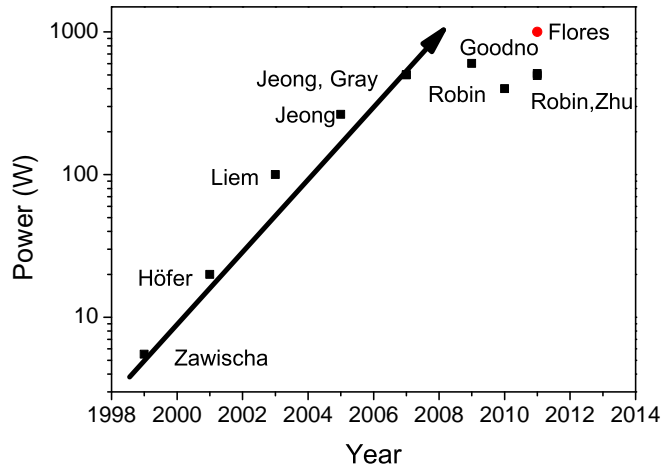


Figure 2.2: History of single frequency fiber amplifiers. The system presented by Flores et al. [29] (red dot) consists of three coherently combined fiber amplifiers.

index fibers this approach is limited to an NA of about 0.06, which corresponds to a core diameter of $10 \mu\text{m}$. With diameters up to $20\text{-}30 \mu\text{m}$, few mode fibers can be slightly larger and still yield nearly diffraction limited beam quality, if the fiber is coiled [32]. However, to maintain diffraction limited beam quality for even larger modefield diameter step index fibers are no longer an option. A lower NA can be achieved in photonic crystal fibers (PCF), alternatively, high losses for higher order modes are possible with chirally coupled core (CCC) fibers - both designs enable larger core diameters.

Other options to increase the SBS thresholds include thermal and stress gradients [33, 34], combination of different fiber types [35], acoustic tailoring [36], and counter propagating pump light [37].

Given high enough power, thermal damage can occur even in fiber amplifiers. Especially the acrylate coatings are prone to damage at high temperatures, which is the reason why an efficient cooling mechanism can be required. Especially erbium doped fiber amplifiers pumped at 976 nm and thulium doped fiber amplifiers pumped at 795 nm require efficient cooling, because their quantum efficiency is lower than for ytterbium doped fiber amplifiers and thus more heat is generated. In most cases

this is a technical problem, however, the maximum coating temperature also puts an upper limit on the SBS suppression by a thermal gradient.

Besides thermally induced coating damage, the temperature induced refractive index change can also lead to limitations. A change of the refractive index influences the signal phase as already discussed, but also changes the waveguide properties of the fiber [38, 39]. Additionally, refractive index changes combined with amplifier dynamics can lead to the formation of a thermally induced long period fiber grating (LPFG), which transfers power from the fundamental fiber mode to higher order modes [40–42]. This thermally induced grating leads to a sharp threshold from effectively single mode to chaotic multi mode behavior. There has been a lot of activity in this field recently, essentially the effect is explained by a beating between fundamental and a higher order mode causing a spatially varying heat load forming a LPFG [43–45]. For efficient power transfer between the fundamental and the higher order mode a moving grating is required for the phase matching; this can be explained by thermal diffusion [46].

These effects limit the output power of single frequency fiber amplifiers and are the reason why the highest power of a single amplifier is still 600 W obtained with a thulium doped amplifier [47]. Even though SBS is less of a concern at this wavelength, this achievement is especially remarkable because of the high heat load in thulium doped fiber amplifiers.

The highly customized fiber types used in many power scaling experiments have an additional disadvantage: a laser system for GWD is supposed to run for many years, but these highly customized fibers are often not available for such a long timespan. Even top of the line commercial fibers are regularly discontinued after a few years on the market (for example NKT DC-400-38-PZ). Although they are merely replaced by new fibers with potentially better performance, these new fiber types lead to significant changes to the system. Therefore, even if a single frequency fiber amplifier achieves significantly more than 500 W in the near future, such a system might not be the optimum choice for GWDs. A slightly more conservative approach using a proven fiber design might be more suitable. In this case the chance that the fibers will be discontinued decreases and thus long term stability is much

improved. However, with such components it is unlikely that the output power required for 3rd generation GWD will be reached in the foreseeable future.

2.3 Coherent Beam Combining

The discrepancy between required output power for GWDs and available output power from a single fiber amplifier can be solved by coherent beam combining. All-fiber amplifiers with simple step index fiber designs can reach up to 300 W [14]. Four of them would lead to 1.2 kW of total available output power with reasonable system complexity. However, the four beams have to be combined and the beam quality has to be preserved in the process. This can be achieved with CBC. As long as two output beams have the correct phase relationship, a 50:50 beam splitter can be used as a combining element (Fig. 2.3) and the complete output power is available at one output port. The most common geometry for coherent beam combining of fiber amplifiers is depicted in Fig. 2.3. It is essentially a Mach-Zehnder interferometer with amplifiers placed in the interferometer arms¹. Therefore, the equations known from for the Mach-Zehnder interferometer can also be applied for CBC.

To calculate the output power at one port² of the system, both electric fields have

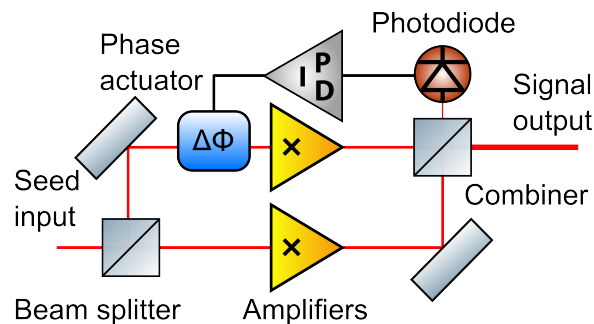


Figure 2.3: Principle of coherent beam combining.

- 1 For a combination of pulsed amplifiers the Sagnac geometry can be advantageous [48]. In this case the phase relationship of the beams is intrinsically stable.
- 2 At the other output port the relative phase between both waves is shifted by 180°.

to be overlapped. If both fiber amplifiers operate at the same output power P , this leads to

$$\begin{aligned}
 E_{\text{out}} &= \frac{1}{\sqrt{2}}(\sqrt{P} e^{i\omega t} + \sqrt{P} e^{i\omega t + i\Delta\Phi}) \\
 &= \sqrt{\frac{P}{2}} e^{i\omega t} (1 + e^{i\Delta\Phi}) \\
 &= \sqrt{2P} e^{i\omega t + i\Delta\Phi/2} \cos\left(\frac{\Delta\Phi}{2}\right).
 \end{aligned} \tag{2.1}$$

Here $\Delta\Phi$ is the total relative phase between both fields. Therefore, the detected power at this output port is

$$P_{\text{out}} = 2P \cos^2\left(\frac{\Delta\Phi}{2}\right). \tag{2.2}$$

The whole power is combined at this output port, if $\Delta\Phi = 2n\pi$ can be maintained with n being an integer. For this it is necessary to detect and actively stabilize the relative phase between both optical paths, because mechanical vibrations and amplifier phase noise lead to fluctuations.

If the interferometer is locked to maximum output power, there are important implications for the impact of residual phase noise. Expansion of the cosine in equation (2.2) leads to

$$P_{\text{out}}(t) \approx 2P \left(1 - \frac{\Delta\Phi(t)^2}{4} + \frac{\Delta\Phi(t)^4}{48}\right). \tag{2.3}$$

Therefore, the mean output power is $\langle P_{\text{out}} \rangle \approx 2P(1 - \langle \Delta\Phi(t)^2 \rangle / 4)$. Hence, for less than 1% combining loss a phase variance $\langle \Delta\Phi(t)^2 \rangle \leq 4 \cdot 10^{-2} \text{rad}^2$ is required. Of course the phase variance is not the only aspect to consider for combining efficiency. Other reasons for decreased combining efficiency include relative mis-modematching, nonuniform powers and polarization errors. A detailed analysis of those effects was reported by Goodno et al. [49].

The CBC concept can be extended to many amplifiers as shown in Fig. 2.4. In

this case there are different concepts concerning the combining element. A tiled aperture combining element only overlaps the beams in the far field [50, 51]. This results in imperfect beam quality, but the beam can be steered using phase control [52]. In the case of fiber amplifiers this can be realized by stacking the fiber ends close to each other. Since the resulting beam quality is limited, this is not a useful method for laser systems for GWDs. To realize the best possible beam quality, the beams have to be overlapped in both near and far field. This can be realized by stacking 2^n 50% splitters or by using gratings or fiber couplers [53, 54].

Until 2009, coherent beam combining was almost exclusively used with directed energy applications in mind [55, 56]. But over the last 3 years, coherent beam combining has gained a lot of momentum and it is now even used in ultrafast fiber amplifiers [57–59]. During the course of this thesis the suitability of coherently combined fiber lasers for GWD was verified in 2011. Kilowatt class single frequency filled aperture combining was demonstrated by Flores in the same year [29]. Although no noise or beam quality information is available for this system, this at least shows that the power requirement can be met with this approach.

Other laser development groups within the GW community integrated coherent beam combining in their laser designs and as of mid 2012, the laser system planned for advanced VIRGO will most likely consist of two coherently combined 100 W fiber amplifiers once this power level is required for the detector. While such a system does not deliver more output power than the solid state laser system used

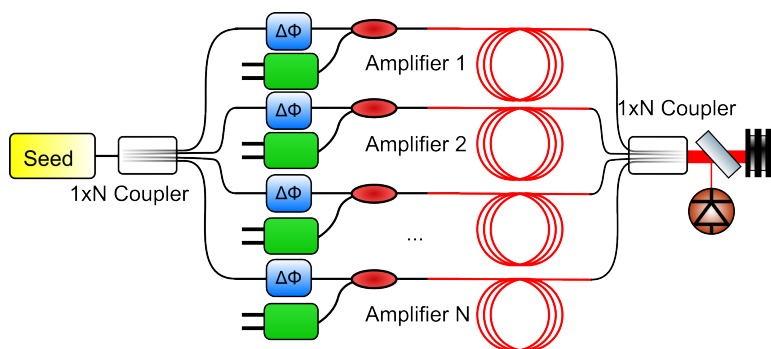


Figure 2.4: CBC of many fiber amplifiers.

for advanced LIGO, it will be the first productive use of fiber amplifiers and CBC in a GWD – which comes with all of the advantages such as reduced cost and much higher efficiency than the advanced LIGO pre-stabilized laser.

3 Time Dependent Fiber Amplifier Model

To model the noise and temporal dynamics of fiber amplifier, this chapter develops a theoretical description of single frequency fiber amplifiers using rate equations [60]. For many applications the steady state solution is sufficient, because only the achievable output power for a given configuration is of interest. However, if possible noise couplings – specifically the transfer of pump- and seed power fluctuations to output power – are of interest, the time dependence in the rate equations is critical.

3.1 Rate Equations

A change of seed and/or pump power eventually changes the population of the upper laser level N_2 , which in turn modifies the output power. The temporal dynamic of this effect is determined by the rate equations

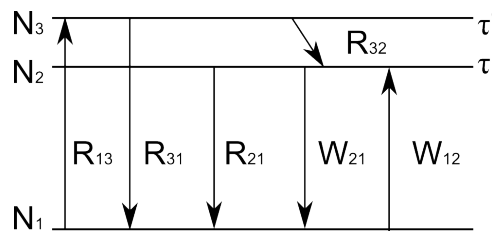


Figure 3.1: Transition rates in a 3 level system.

$$\begin{aligned}
\frac{\partial}{\partial t}n_1 &= -R_{13}n_1 - W_{12}n_1 + W_{21}n_2 + R_{21}n_2 + n_2/\tau + R_{31}n_3 + n_3/\tau' \\
\frac{\partial}{\partial t}n_2 &= W_{12}n_1 - W_{21}n_2 - R_{21}n_2 + R_{32}n_3 - n_2/\tau \\
\frac{\partial}{\partial t}n_3 &= R_{13}n_1 - R_{32}n_3 - R_{31}n_3 - n_3/\tau'.
\end{aligned} \tag{3.1}$$

Here n_i is the density of ions in the i th level, τ and τ' are the ion lifetimes, R_{ij} are the transition rates associated with the pump, and W_{ij} are those associated with the signal as depicted in Fig. 3.1. For most laser materials the transition from the third to the second level is much faster than the other transitions ($R_{32} \gg R_{31}$ and $R_{32} \gg 1/\tau'$). Therefore, it can be assumed that n_3 decays exclusively to n_2 . Together with the ion density $\rho = n_1 + n_2$ this simplifies the rate equations to a single equation

$$\begin{aligned}
\frac{\partial}{\partial t}n_2 &= W_{12}n_1 - W_{21}n_2 + R_{13}n_1 - R_{21}n_2 - n_2/\tau \\
&= W_{12}(\rho - n_1) - W_{21}n_2 + R_{13}(\rho - n_1) - R_{21}n_2 - n_2/\tau.
\end{aligned} \tag{3.2}$$

The transition rates can be calculated with the following equations

$$\begin{aligned}
W_{12} &= \int \frac{\Gamma_S \sigma_{ab}(\lambda)(P_s(\lambda) + P_{ase,f}(\lambda) + P_{ase,b}(\lambda))}{A} d\lambda \\
W_{21} &= \int \frac{\Gamma_S \sigma_{em}(\lambda)(P_s(\lambda) + P_{ase,f}(\lambda) + P_{ase,b}(\lambda))}{A} d\lambda \\
R_{13} &= \int \frac{\Gamma_P \sigma_{ab}(\lambda)P_p(\lambda)}{A} d\lambda \\
R_{21} &= \int \frac{\Gamma_P \sigma_{em}(\lambda)P_p(\lambda)}{A} d\lambda.
\end{aligned} \tag{3.3}$$

Here $P_p(\lambda)$ and $P_s(\lambda)$ are the power spectral densities of pump and signal light in photons per time and wavelength. Additionally, also amplified spontaneous emission (ASE) in forward ($P_{ase,f}(\lambda)$) and backward ($P_{ase,b}(\lambda)$) direction has to be included in case of very high gain. The wavelength is given by λ , Γ_S and Γ_P are the overlap of signal and pump light with the doped region, σ_{ab} and σ_{em} are the absorption and

emission cross sections, and A is the effective area of the core.

The evolution of pump, signal and ASE power along the fiber can be described by the following differential equations:

$$\begin{aligned}
\frac{\partial}{\partial z} P_p &= -\Gamma_p \sigma_{pa} n_1 P_p + \Gamma_p \sigma_{pe} n_2 P_p - \gamma_p P_p \\
\frac{\partial}{\partial z} P_s &= -\Gamma_s \sigma_{sa} n_1 P_s + \Gamma_s \sigma_{se} n_2 P_s - \gamma_s P_s \\
\frac{\partial}{\partial z} P_{ase,f} &= -\Gamma_s \sigma_{sa} n_1 P_{ase,f} + \Gamma_s \sigma_{se} n_2 P_{ase,f} - \gamma_s P_s \\
\frac{\partial}{\partial z} P_{ase,b} &= \Gamma_s \sigma_{sa} n_1 P_{ase,f} - \Gamma_s \sigma_{se} n_2 P_{ase,f} + \gamma_s P_s.
\end{aligned} \tag{3.4}$$

with the cross sections σ_{pa} , σ_{pe} , σ_{sa} and σ_{se} for pump absorption, pump emission, signal absorption and signal emission at the corresponding wavelength and γ_s and γ_p are absorption coefficients for signal and pump light.

In steady state the number of ions in the upper laser level does not vary with time ($\frac{\partial}{\partial t} n_2 = 0$). Therefore, equation (3.2) can be solved for n_2 and the result can be inserted into equations (3.4). In case of forward pumping and low (backward) ASE, these equations are essentially an initial value problem, which can directly be integrated numerically. Otherwise a two point boundary value problem has to be solved.

To analyze the coupling of seed and pump power modulation, the time dependent output power of an amplifier is required. Therefore, equation (3.2) has to be integrated for each point along the z-axis. One simplification is possible, because light waves travel through the fiber at more than 2/3 of the vacuum speed of light. Therefore, the time a photon stays in the fiber is small compared to the timescales which are of interest here ($f \leq 100$ kHz). Because of that, propagation times can be neglected and it is possible to first propagate all the light fields through the fiber, then calculate $\frac{\partial}{\partial t} n_2$ and update n_2 for the next time step. Alternating between updating n_2 and the fields will eventually lead to a time domain transient.

Such numerical simulations can yield accurate results, if the required parameters are known. However, this is still very computationally intensive, especially when modulations of few Hz are tracked. Additionally, the influence of specific system

parameters – which is required for design guidelines – cannot be analyzed directly.

3.2 Analytic Model

In a well designed fiber amplifier for GWD the amount of ASE should be low, since the presence of a large amount of ASE is usually an indication for too high gain and such amplifiers are prone to parasitic lasing and excess noise in the MHz region. Fortunately, modeling becomes much more simple, if ASE can be neglected. In this case even an analytic model is feasible [16]. This is much better suited to understand the influence of the system parameters.

As first shown by Bononi et al. [61], if ASE can be neglected the rate equations can be rewritten to

$$\begin{aligned}\frac{\partial}{\partial z}P_p &= -R_{13}An_1 + R_{21}An_2 - \gamma_p P_p \\ \frac{\partial}{\partial z}P_s &= -W_{12}An_1 + W_{21}An_2 - \gamma_s P_s.\end{aligned}\tag{3.5}$$

If now equation (3.2) is multiplied by the effective area A and the equations (3.5) are inserted, this leads to

$$\frac{\partial}{\partial t}n_2A = -\frac{\partial}{\partial z}P_p - \frac{\partial}{\partial z}P_s - \gamma_s P_s - \gamma_p P_p - n_2A/\tau.\tag{3.6}$$

Neglecting the loss terms, equation (3.6) can be integrated along the z -axis from the beginning ($z = 0$) to the end of the fiber ($z = L$):

$$\frac{\partial}{\partial t}N_2 = P_p(0) - P_p(L) + P_s(0) - P_s(L) - N_2/\tau\tag{3.7}$$

with N_2 being the total number of ions in the excited state.

Assuming monochromatic pump and signal light the integrals in equations (3.3) become equations of the form $W = \Gamma\sigma P/A$. For erbium doped fiber amplifiers pumped at 1480 nm or ytterbium fiber amplifiers pumped at 976 nm the upper laser level can be depleted by the pump light. On the other hand erbium doped fiber

amplifiers pumped at 976 nm will not be depleted. This has to be considered when calculating R_{21} from the absorption and emission cross sections. Neglecting the loss terms in equation (3.4) the signal and pump power at the end of the fiber can be calculated by

$$\begin{aligned} P_s(L) &= P_s(0) \exp(-\Gamma_s \sigma_{sa} N_1/A + \Gamma_s \sigma_{se} N_2/A) \\ P_p(L) &= P_p(0) \exp(-\Gamma_p \sigma_{pa} N_1/A + \Gamma_p \sigma_{pe} N_2/A). \end{aligned} \quad (3.8)$$

Here N_2 is the total number of ions in the excited state and N_1 is the number of ions in the ground state. Using $N_1 = \rho LA - N_2$ with ρ being the density of ions, equation (3.8) can be written as

$$\begin{aligned} P_p(L) &= P_p(0) \exp(B_p N_2 - C_p) \\ P_s(L) &= P_s(0) \exp(B_s N_2 - C_s) \end{aligned} \quad (3.9)$$

with the coefficients

$$\begin{aligned} B_p &= \Gamma_p (\sigma_{pa} + \sigma_{pe})/A \\ B_s &= \Gamma_s (\sigma_{sa} + \sigma_{se})/A \\ C_p &= \Gamma_p \sigma_{pa} \rho L \\ C_s &= \Gamma_s \sigma_{sa} \rho L. \end{aligned} \quad (3.10)$$

The equations (3.9) can be inserted into equation (3.7). For the occupation of the N_2 -level this means

$$\frac{\partial}{\partial t} N_2 = P_p(0)(1 - \exp(B_p N_2 - C_p)) + P_s(0)(1 - \exp(B_s N_2 - C_s)) - N_2/\tau. \quad (3.11)$$

This will be the major equation to obtain the information about the temporal behavior. The main idea is to obtain analytic expressions for the transfer of pump and signal power modulations to the output power from equation (3.11). In contrast to the derivation by Novak et al. [16], complex notation will be used here instead of cosine and sine, which makes the derivation more easy to follow.

In steady state the occupation of the upper laser level does not change ($\frac{\partial}{\partial t} N_2 = 0$).

So, equation (3.11) can be solved for N_2 numerically, after which output power, unabsorbed pump power and N_2 are known. But this only deals with constant input seed and pump power.

The next question to answer is what happens in case of a small modulation of the pump or seed power, i.e.

$$P_{s,p}(0, t) = P_{s,p}^0(0)(1 + m_{s,p} e^{i\omega t}) \quad (3.12)$$

with the modulation index $m_{s,p}$ and the average input power $P_{s,p}^0(0)$. This modulation will lead to a varying occupation of the upper laser level

$$N_2(t) = N_2^0(1 + \delta_{s,p} e^{i(\omega t + \Phi_{s,p})}), \quad (3.13)$$

with the modulation index $\delta_{s,p}$ and corresponding phase $\Phi_{s,p}$ ¹, and the average number of ions in the upper laser level N_2^0 . This modulation will eventually lead to a modulation of the output power

$$P_s(L, t) = P_s(0, t) \exp(B_s N_2(t) - C_s) = P_s^0(L)(1 + m'_{s,p} e^{i(\omega t + \phi_{s,p})}) \quad (3.14)$$

with the modulation index $m'_{s,p}$ and phase $\phi_{s,p}$. The average output power $P_{s,p}^0(L)$ is given by equation (3.9).

The first task is to relate $\delta_{s,p}$ and the corresponding phase $\Phi_{s,p}$ to the input modulation $m_{s,p}$. Starting with pump modulation, equations (3.12) and (3.13) are inserted into equation (3.11), which results in

$$\begin{aligned} iN_2^0 \delta_p \omega e^{i(\omega t + \Phi_p)} = & P_s^0(0) [1 - \exp(B_s N_2^0(1 + \delta_p e^{i(\omega t + \Phi_p)}) - C_s)] \\ & + P_p^0(0)(1 + m_p e^{i\omega t}) \cdot [1 - \exp(B_p N_2^0(1 + \delta_p e^{i(\omega t + \Phi_p)}) - C_p)] \\ & - \frac{N_2^0(1 + \delta_p e^{i(\omega t + \Phi_p)})}{\tau}. \end{aligned} \quad (3.15)$$

¹ In this definition $\delta_{s,p}$ is a real number. While this is an uncommon definition, it ensures that the delta used here is compatible to the definition of delta in the derivation by Novak et al.

Keeping only the first order terms in δ_p and m_p and subtracting the steady state solution leads to

$$iN_2^0\delta_p\omega e^{i(\omega t+\Phi_p)} = \left(-P_s^0(L)B_pN_2^0\delta_p - P_p^0(L)B_pN_2^0\delta_p - \frac{N_2^0\delta_p}{\tau} \right) e^{i(\omega t+\Phi_p)} + [P_p^0(0) - P_p^0(L)]m_p e^{i\omega t}. \quad (3.16)$$

Some rearranging allows to derive the phase and magnitude relationship

$$\frac{N_2^0\delta_p}{m_p} e^{i\Phi_p} = \frac{P_p^0(0) - P_p^0(L)}{[P_s^0(L)B_s + P_p^0(L)B_p + \frac{1}{\tau}] + i\omega} \quad (3.17)$$

which has the form of a low pass filter ($f = \frac{K}{1+i\omega/\omega_{\text{eff}}}$) with a pole at the corner frequency

$$\omega_{\text{eff}} = P_s^0(L)B_s + P_p^0(L)B_p + 1/\tau \quad (3.18)$$

and a frequency independent gain factor

$$K_p = \frac{P_p^0(0) - P_p^0(L)}{P_s^0(L)B_s + P_p^0(L)B_p + \frac{1}{\tau}}. \quad (3.19)$$

The physical meaning of the corner frequency ω_{eff} is the reciprocal of an effective ion lifetime in the amplifier, but should not be confused with the fluorescence lifetime τ . The gain K_p is simply the rate of ions getting excited divided by the decay rate. Since this is a standard low pass filter, it is simple to get to the magnitude and phase relationship of the non-complex form derived by Novak et al. [16]:

$$\tan(\Phi_p) = -\frac{\omega}{\omega_{\text{eff}}} \quad (3.20)$$

$$N_2^0\delta_p = m_p \frac{[P_p^0(0) - P_p^0(L)]}{\sqrt{\omega^2 + \omega_{\text{eff}}^2}}.$$

In case of seed modulation the derivation is identical and results in

$$\frac{N_2^0 \delta_s}{m_s} e^{i\Phi_s} = \frac{P_s^0(0) - P_s^0(L)}{\omega_{\text{eff}} + i\omega} \quad (3.21)$$

and the polar form

$$\begin{aligned} \tan(\Phi_s) &= -\frac{\omega}{\omega_{\text{eff}}} \\ N_2^0 \delta_s &= m_s \frac{[P_s^0(0) - P_s^0(L)]}{\sqrt{\omega^2 + \omega_{\text{eff}}^2}}. \end{aligned} \quad (3.22)$$

The impact of pump modulation on the output power can be calculated by simply neglecting the higher order modulation terms in equation (3.14)

$$\begin{aligned} P_s(L,t) &= P_s^0(0) \exp(B_s N_2^0 (1 + \delta_p e^{i(\omega t + \Phi_p)})) \\ &\approx P_s^0(L) (1 + B_s N_2^0 \delta_p e^{i(\omega t + \Phi_p)}) \end{aligned} \quad (3.23)$$

and inserting equation (3.17) into equation (3.23), which results in

$$\frac{m'_p}{m_p} e^{i\phi_p} = \frac{B_s [P_p^0(0) - P_p^0(L)]}{\omega_{\text{eff}} + i\omega}, \quad (3.24)$$

which is equivalent to the form derived by Novak et al. [16]:

$$\begin{aligned} \tan(\phi_p) &= -\frac{\omega}{\omega_{\text{eff}}} \\ m'_p &= m_p \frac{B_s [P_p^0(0) - P_p^0(L)]}{\sqrt{\omega^2 + \omega_{\text{eff}}^2}}. \end{aligned} \quad (3.25)$$

Besides the additional factor B_s , the relationship is the same as for the modulation of N_2 . The impact of seed modulation is not quite as simple, as the input seed

modulation has to be considered as well as the modulation of the upper laser level:

$$\begin{aligned} P_s(L,t) &= P_s^0(0)(1 + m_s e^{i\omega t}) \exp(B_s N_2^0(1 + \delta_s e^{i(\omega t + \phi_s)} - C_s)) \\ &\approx P_s^0(L)(1 + m_s e^{i\omega t} + B_s N_2^0 \delta_s e^{i(\omega t + \phi_s)}). \end{aligned} \quad (3.26)$$

Inserting equation (3.21) into equation (3.26) leads to

$$m'_s e^{i\phi_s} = m_s \frac{\omega_{\text{eff}} + i\omega + B_s[P_s^0(0) - P_s^0(L)]}{\omega_{\text{eff}} + i\omega} = m_s \frac{\omega_0 + i\omega}{\omega_{\text{eff}} + i\omega}. \quad (3.27)$$

This is a zero-pole transfer function with the zero at

$$\omega_0 = P_s^0(0)B_s + P_p^0(L)B_p + 1/\tau \quad (3.28)$$

and the pole at $\omega = \omega_{\text{eff}}$. Effectively, it is a damped high pass. Again, the magnitude and phase as given by Novak et al. [16] can be calculated:

$$\begin{aligned} \tan(\phi_s) &= -\frac{\omega}{\omega_{\text{eff}} + \frac{\omega^2 + \omega_{\text{eff}}^2}{B_s[P_s^0(0) - P_s^0(L)]}} \\ m'_s &= m_s \frac{\sqrt{\omega^2 + (\omega_{\text{eff}} + B_s[P_s^0(0) - P_s^0(L)])^2}}{\sqrt{\omega^2 + \omega_{\text{eff}}^2}} = m_s \sqrt{\frac{\omega^2 + \omega_0^2}{\omega^2 + \omega_{\text{eff}}^2}}. \end{aligned} \quad (3.29)$$

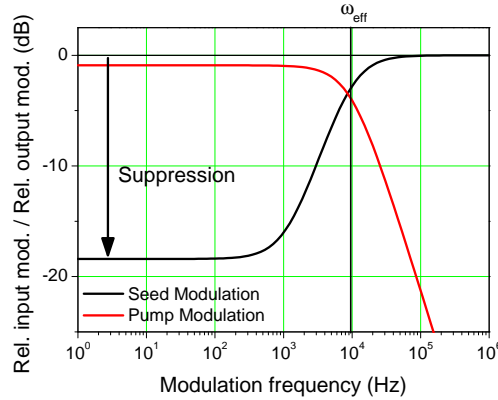


Figure 3.2: Exemplary transfer function for pump and seed power modulation.

Since the shape of the transfer functions is now known (Fig. 3.2), the important properties are the corner frequency ω_{eff} and the low frequency suppression factor in case of seed modulation. The corner frequency is the same for seed and pump power modulation and is given by equation (3.18). Only, if the modulation frequency is lower than the corner frequency ω_{eff} , the population of the upper laser level can adapt: therefore pump fluctuations couple to output power below the corner frequency but not above. On the other hand increased seed power means less amplifier gain, if the population adapts to the new situation, which is why relative seed fluctuations are suppressed at low frequencies. Because the underlying physical process – the population changes of the upper laser level – is identical for seed and pump modulation, the respective corner frequencies are identical. For seed modulation additionally either the frequency of the zero in equation (3.27) or the suppression factor at low frequencies as shown in Fig. 3.2 is required. Physically the more meaningful value is the suppression factor.

This section will be concluded with the transfer of signal and pump power modulation to the unabsorbed pump light. Their derivation is analogous to the transfer of seed and pump power modulation to output power described by equations (3.25) and (3.29), therefore just the results are stated here

$$m_s'' = m_s \frac{B_p(P_s^0(0) - P_s^0(L))}{\sqrt{\omega^2 + \omega_{\text{eff}}^2}} \quad (3.30)$$

$$\tan(\theta_s'') = -\frac{\omega}{\omega_{\text{eff}}}$$

$$m_p'' = m_p \frac{\sqrt{\omega^2 + (\omega_{\text{eff}} + B_p[P_p^0(0) - P_p^0(L)])^2}}{\sqrt{\omega^2 + \omega_{\text{eff}}^2}} \quad (3.31)$$

$$\tan(\theta_p'') = -\frac{\omega}{\omega_{\text{eff}} + (\omega^2 + \omega_{\text{eff}}^2)/(B_p(P_p^0(0) - P_p^0(L)))}$$

Here, m_s'' is the modulation index for seed power modulation and m_p'' is the modulation index for pump power modulation and $\theta_{s,p}''$ is the corresponding phase. Therefore, unabsorbed pump light behaves in the same way signal light does, but with the roles

of seed and pump power modulation exchanged. However, due to the absorption of the pump power ($B_p^0(0) > B_p^0(L)$), the transfer function from pump light to unabsorbed pump light is not a damped high- but a damped low pass.

3.3 Large Output Power Approximation

The remaining question is how typical design parameters of single frequency fiber amplifiers affect the critical parameters and how to reconstruct the behavior from experimentally accessible data. The corner frequency increases with output power. However, the design output power of single frequency amplifiers will have little impact on the corner frequency, as power scaling of single frequency amplifiers is usually achieved by scaling the core size to increase the SBS threshold. In most continuous wave fiber amplifiers the term $P_s^0(L)B_s$ is much larger than the others. For a typical erbium doped fiber amplifier (EDFA), one can estimate the corner frequency $f_{\text{eff}} = \omega_{\text{eff}}/2\pi$ to be in the range of 1-10 kHz. Compared to a fluorescence lifetime in the range of 10 ms, $f_{\text{eff}} = 1/(2\pi\tau) \approx 16$ Hz, this is a very large value. So, unless the ion lifetime is very small, which is not the case for erbium, or the fiber does not absorb a significant amount of pump light (which can be necessary in some cases, for example to increase the SBS threshold), $\omega_{\text{eff}} \approx P_s^0(L)B_s$ is a good estimation of the corner frequency.

To completely model the seed modulation, additional knowledge of the low frequency suppression is required. In an ideal amplifier with a seed power significantly larger than the saturation power, one would expect fast modulations to be amplified in the same way as the average power, because the inversion cannot follow in time. On the other hand low frequencies should not be amplified, as the inversion adapts to the changing power levels and decreases the amplification factor for higher seed power levels and vice versa.

Using equation (3.29), it can be investigated whether this intuitive picture is justified. For high frequencies $m'_s = m_s$, is true for all amplifier parameters. At

$\omega = 0$ and inserting the expression for ω_{eff} (3.18) this can be rewritten to

$$m'_s = m_s \left(\frac{P_s^0(0) \cdot B_s + P_p^0(L) \cdot B_p + 1/\tau}{P_s^0(L) \cdot B_s + P_p^0(L) \cdot B_p + 1/\tau} \right). \quad (3.32)$$

Now assuming the output power to be much larger than spontaneous emission and remaining pump light ($P_s^0(L) \cdot B_s \gg P_p^0(L) \cdot B_p + \frac{1}{\tau}$) one arrives at

$$m'_s = \frac{m_s}{P_s^0(L)} \left(P_s^0(0) + \frac{1}{\tau B_s} + P_p^0(L) \frac{B_p}{B_s} \right). \quad (3.33)$$

As long as the seed power is large compared to the saturation power and the unabsorbed pump power (second and third term in equation (3.33)), the suppression is indeed the inverse gain. It is worth noting that fiber parameters such as B_p , B_s and τ are only included in the second and third term and, therefore, not required for this first estimate. The second term is the low gain approximation of amplifier saturation power. Therefore, $m'_s \approx m_s P_s^0(0) / P_s^0(L)$ is only a good approximation, as long as the seed power is larger than the saturation power. More seed power decreases the amount of ions decaying spontaneously. It also reduces the amount of ASE, which decreases the suppression just like spontaneous emission [62].

According to the third term in equation (3.33), unabsorbed pump power has to be considered as well. Increasing the seed power cannot increase the amount of absorbed pump light, if the pump light is already completely absorbed. On the other hand, if there is a large amount of unabsorbed pump light, a small change in seed power at low frequencies changes how much pump light is absorbed. Therefore, more seed power causes more pump power to be absorbed and the gain for low frequencies increases, resulting in a lower suppression.

The effect itself is the same for all laser materials. For GWDs operating at 1550 nm or 1064 nm, erbium and ytterbium doped fiber amplifiers are of major interest. In an ytterbium doped fiber amplifier the cross sections are about one order of magnitude larger at 976 nm than at 1064 nm and therefore $B_p \gg B_s$, while in an erbium doped fiber amplifier the cross sections are similar ($B_p \approx B_s$). Thus, the pump contribution in equation (3.33), which is weighted by the cross sections,

has a larger impact in ytterbium doped fiber amplifiers. The same is also true for the saturation power, as the lifetime of ytterbium ions is one order of magnitude shorter than the lifetime of erbium ions. Therefore, similar power levels can lead to very different behavior.

High average seed power compared to saturation power of the amplifier and to unabsorbed pump power reduces the impact of both the second and third term. Therefore, increasing seed power and operating in the saturated regime is a suitable method to reduce the impact of the second and third term, which makes the transfer function simple.

The same approximations can also be applied to pump power modulation. The transfer function of pump power modulation is given by the equation (3.25). At $\omega = 0$ this equation can be rewritten to

$$m'_p = m_p \left(\frac{B_s [P_p^0(0) - P_p^0(L)]}{P_s^0(L)B_s + P_p^0(L)B_p + 1/\tau} \right) = m_p \left(\frac{B_s [P_s^0(L) - P_s^0(0) + N_2/\tau]}{P_s^0(L)B_s + P_p^0(L)B_p + 1/\tau} \right) \quad (3.34)$$

because in steady state the number of absorbed photons equals the number of emitted photons ($P_p^0(0) - P_p^0(L) = P_s^0(L) - P_s^0(0) + N_2/\tau$) according to equation (3.7). The large output power approximation ($P_s^0(L)B_s \gg P_p^0(L)B_p + 1/\tau$) then leads to

$$m'_p \approx m_p \left(1 - \frac{P_s^0(0)}{P_s^0(L)} + \frac{N_2/\tau}{P_s^0(L)} \right). \quad (3.35)$$

Neglecting $\frac{N_2/\tau}{P_s^0(L)}$ (corresponding to low spontaneous emission) it can be seen that, if $\frac{P_s^0(0)}{P_s^0(L)}$ is close to 0, e.g. if the amplification is large, $m'_p \approx m_p$ is valid. At the same time the suppression for seed modulation is large, unless the amplifier is unsaturated. On the other hand, if $\frac{P_s^0(0)}{P_s^0(L)} \approx 1$, pump modulation is suppressed, while seed modulation is not. More generally speaking, if the seed modulation is suppressed, there will be more pump modulation and vice versa.

3.4 Design Guidelines

To conclude this chapter some general design guidelines will be given. The corner frequency ω_{eff} depends on the ion lifetime, which cannot be changed except by choosing different dopants and thus operating wavelengths. On the other hand, it also depends on the fiber output intensities, which can be changed. When operating the fiber amplifier at its maximum output power ω_{eff} is also close to its maximum. Deliberately increasing the amount of unabsorbed pump power can further increase ω_{eff} , but is not always desirable.

If on the other hand a low ω_{eff} is required, this can be achieved with low intensities and is only limited by the fluorescence lifetime and practical detection levels.

In first order, increasing the low frequency suppression for seed power modulation is as simple as increasing the gain. However, this works much better, if the required saturation power is low (e.g. erbium). Also most of the pump light must be absorbed, especially, if the respective cross sections are larger than the seed cross sections. If seed suppression is high, this also results in a steeper slope of the transfer function and a larger associated phase shift. Low seed suppression is beneficial for low noise amplifiers as long as the seed source exhibits less noise than the pump source. In this case it is preferable to reduce the influence of the pump source, instead. This can be achieved with a high level of unabsorbed pump power, again. There is a practical limit, however, as too much unabsorbed pump power is usually undesirable.

4 Experimental Results: Power Modulation

In this chapter the predictions of the analytical model are compared with experimental data. The main advantages of the analytical model are the easy estimation of the dynamic behavior from experimentally accessible parameters and the possibility to derive design guidelines. However, exact quantitative predictions cannot be expected due to the lower efficiency of real fiber amplifiers. This is even the case in potentially more accurate numerical models, because the exact amplifier parameters – especially loss coefficients – are usually not known well enough. However, if the predicted trends are well reproduced and the transfer functions can be estimated from input and output power the analytic model is a very useful tool.

4.1 Erbium Doped Fiber Amplifier

To compare with the analytic model an erbium doped fiber amplifier (EDFA) was built. A 1550 nm distributed feedback (DFB) diode with up to 46 mW average power was amplified in 3.5 m erbium doped fiber (Liekki Er 30-4/125), which was co-pumped at 1480 nm (Fig. 4.1). At a pump power of 530 mW and an output power of about 400 mW, seed and pump power were modulated. The amplifier's signal output was separated from the residual pump light with a wavelength division multiplexer (WDM) and the resulting output power modulation was observed with a photodiode. During the measurement the modulation index was kept as small as possible to avoid nonlinearities.

In this measurement the magnitude and phase were derived from the corresponding signal voltages. Therefore, all involved circuits contributed to the measured gain. To compare the data with the model predictions, which only consider the optical

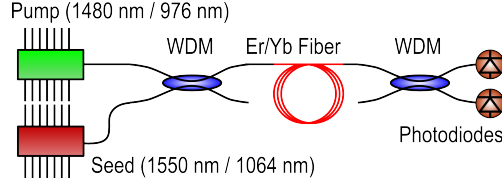


Figure 4.1: Amplifier setup.

amplifier, the data has to be calibrated. Instead of measuring the gain of all the components for each operating condition, there is a more practical way to calibrate the data in this case. The complex transfer functions from chapter 3

$$\frac{m'_s e^{i\phi_s}}{m_s} = \frac{\omega_{\text{eff}} + i\omega + B_s[P_s^0(0) - P_s^0(L)]}{\omega_{\text{eff}} + i\omega} \quad (4.1)$$

$$\frac{m'_p e^{i\phi_p}}{m_p} = \frac{B_s[P_p^0(0) - P_p^0(L)]}{\omega_{\text{eff}} + i\omega} \quad (4.2)$$

show why this is the case. For high frequencies the contribution from seed modulation can be estimated to be 1 according to equation (4.1). This already provides the correct scaling factor for the seed modulation transfer function. Adding the equations (4.1) and (4.2) leads to

$$\frac{m'_s e^{i\phi_s}}{m_s} + \frac{m'_p e^{i\phi_p}}{m_p} = \frac{\omega_{\text{eff}} + i\omega + B_s[P_s^0(0) - P_s^0(L)] + B_s[P_p^0(0) - P_p^0(L)]}{\omega_{\text{eff}} + i\omega}. \quad (4.3)$$

The number of absorbed pump photons is the same as the number of emitted signal photons and the number of spontaneously emitted photons ($[P_s^0(0) - P_s^0(L)] = -[P_p^0(0) - P_p^0(L)] + N_2/\tau$), which leads to

$$\frac{m'_s e^{i\phi_s}}{m_s} + \frac{m'_p e^{i\phi_p}}{m_p} = 1 + \frac{B_s N_2}{(\omega_{\text{eff}} + i\omega)\tau}. \quad (4.4)$$

Therefore, equation (4.4) can be approximated as 1 in case of low spontaneous emission. As long as $\omega \ll \omega_{\text{eff}}$ the phase is approximately zero ($\phi_s \approx \phi_p \approx 0$).

Therefore the equations $m'_s/m_s = 1$ at high frequencies and $m'_p/m_p = 1 - m'_s/m_s$ at low frequencies can be used to normalize the transfer functions. Essentially, all the influences to RPN have to add up to 100% of the RPN.

The measured normalized transfer functions are shown in Fig. 4.2 (solid lines). Their characteristics are as expected, i.e. the low frequency modulations were suppressed in case of seed modulation, and the high frequency modulations were suppressed in case of pump modulation. The general trends are well reproduced by the analytical curves (dashed lines), but in order to account for additional losses the overlap factors (I_p and I_s) were decreased to 0.4, which is slightly too low for a core pumped amplifier. The other parameters used are shown in Table 4.1.

To verify the high seed power approximation (chapter 3) the pump power was increased at fixed seed power of 46 mW. The transfer functions for seed power modulation are shown in Fig. 4.3. As predicted by the large seed power approximation, the seed modulations were only amplified at high frequencies.

The phase shift (Fig. 4.3, bottom) is directly related to the slope of the amplification because of causality. The largest phase shift is possible for the largest slope.

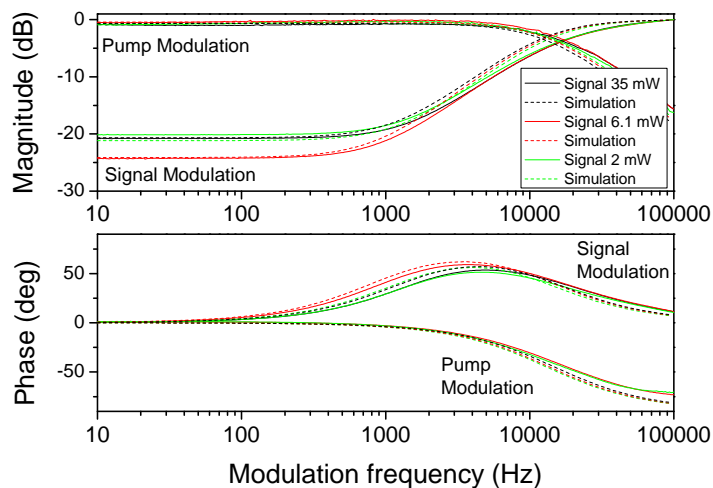


Figure 4.2: Normalized frequency response of the erbium fiber amplifier for different seed power levels. Note that in all graphs we use the field dB scale for the magnitude as it is common in signal processing.

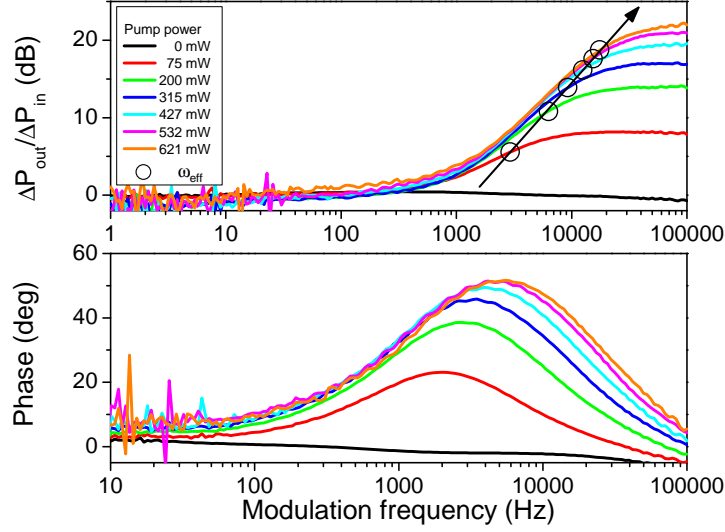


Figure 4.3: Output power for the erbium doped fiber amplifier with seed modulation and 46 mW average seed power. Top: $\Delta P_{\text{out}}/\Delta P_{\text{in}}$, not normalized, bottom: corresponding phase. The circles denote the corner frequency ω_{eff} .

This also corresponds to the highest suppression of low frequency modulations. Since an undamped high pass causes a 90° phase shift, this is the principal limit for the achievable phase shift with a single amplifier.

It can be seen from Fig. 4.3 that the corner frequency was shifted to higher frequencies, when the pump power was increased. This effect is explained by the equation $\omega_{\text{eff}} = B_s P_s^0(L) + B_p P_p^0(L) + 1/\tau$. Accordingly, the corner frequency should increase proportionally to the output power as long as the amount of residual pump power is low. To verify this, the corner frequency $\omega_{\text{eff}} = 2\pi f_{\text{eff}}$ was obtained by fitting a zero-pole transfer function $G = \sqrt{(f^2 + f_0^2)/(f^2 + f_{\text{eff}}^2)}$ to the magnitude of the measured transfer functions. Here, f_0 corresponds to the zero frequency. The result is shown in Fig. 4.4, which shows the linearity. From the slope the factor B_s was determined to be $B_s = 3.45 \cdot 10^{-14}$. The parameters used for the simulation in Fig. 4.2 lead to a value of $B_s = 2.42 \cdot 10^{-14}$. This was lower than the experimentally determined value due to the low overlap factor assumed for simulation. In theory Fig. 4.4 could also be used to obtain the fluorescence lifetime at $P_s = 0$ mW, but the expected value for $1/\tau$ is only 100 Hz (Table 4.1) and therefore the relative error

is very large. The zero frequency ω_0 is shown as well and almost stays constant. As shown in chapter 3 it increases linearly with the residual pump light, which is low in this case.

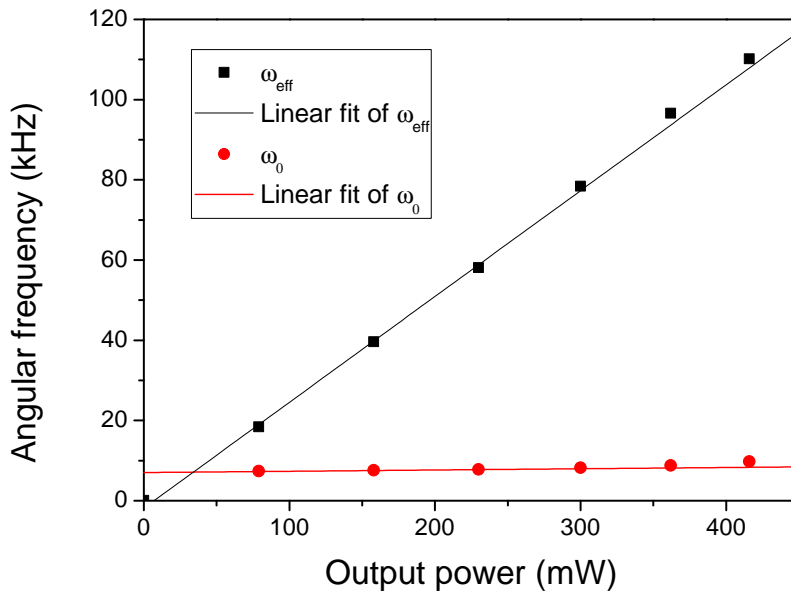


Figure 4.4: Corner frequency ω_{eff} and zero frequency ω_0 in dependence of output power.

Table 4.1: Fiber amplifier parameters.

	Erbium	Ytterbium
Core diameter (μm)	4	6
Fluorescence lifetime (ms)	10	0.7
λ_s (nm)	1550	1064
λ_p (nm)	1480	976
σ_{13} (m^2)	$2.88 \cdot 10^{-25}$	$2.35 \cdot 10^{-24}$
σ_{31} (m^2)	$1.00 \cdot 10^{-25}$	$2.39 \cdot 10^{-24}$
σ_{12} (m^2)	$3.13 \cdot 10^{-25}$	$2.38 \cdot 10^{-27}$
σ_{21} (m^2)	$4.46 \cdot 10^{-25}$	$2.81 \cdot 10^{-25}$
Saturation power (mW)	0.2	10

4.2 Ytterbium Doped Fiber Amplifier

To investigate the influence of the saturation power, an ytterbium amplifier with comparable parameters was used. In principle, the setup was the same as in Fig. 4.1, but now using a 976 nm pump diode, a 1064 nm seed operating at 10 mW and 30 mW average power and an ytterbium doped fiber (Liekki Yb1200-6/125DC, 40 cm). Due to the one order of magnitude larger saturation power of ytterbium, it is better suited to investigate the regime besides the simple saturated amplifier. In fact, the seed power is in the range of the saturation power (Table 4.1). The resulting transfer functions shown in Fig. 4.5 reveal why the different saturation power levels have to be considered: the low frequency modulations are amplified as well and their amplification increases with pump power.

According to equation (3.33) this increase could only be caused by the third term, the residual pump power, because the second term is a constant. However, this was not the case, as there was no significant amount of unabsorbed pump power at low

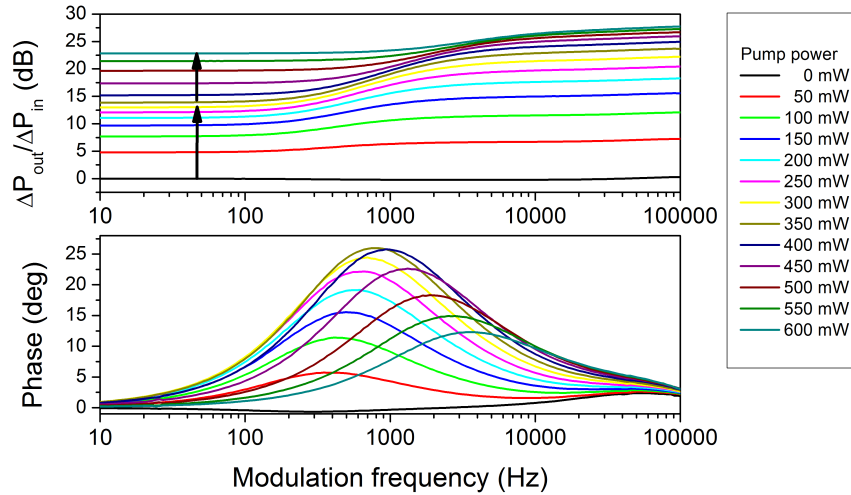


Figure 4.5: Frequency response of the ytterbium doped fiber amplifier for seed modulation and 10 mW average seed power. Even low frequency modulations are amplified. The two arrows show the different regimes: the upper one shows the low frequency gain caused by residual pump light, while the lower one shows the limitations of the large output power approximation.

pump power. Thus, one has to keep the limitations of the approximation in mind, which relies on $P_s^0(L)$ being significantly larger than the saturation power.

However, if $P_s^0(0)$ is at the level of the saturation power and the gain is small as well, the approximation does not hold and overestimates the saturation contribution. Fortunately, this will only happen for very low field intensities in the fiber, which are very unlikely in any realistic cw amplifier design. On the other hand, the increase at higher pump power levels was caused by a rapid increase of unabsorbed pump light, i.e. term 3 in equation (3.33), starting at a pump power level of approximately 350 mW.

The different contributions for low frequency gain at 10 mW and 30 mW seed power are shown in Fig. 4.6. The measured low frequency gain (squares) and the high frequency amplifier gain (bullets) are shown in dependence of output power. The lines are calculated values according to equation (3.32) and the approximation according to equation (3.33) is also shown (dashed lines). Naturally, compared to 10 mW the amplification factor is smaller for the 30 mW seed and the achievable output power levels are higher. At the same time the achievable low frequency suppression is comparable. For the 10 mW seed the low frequency gain increases

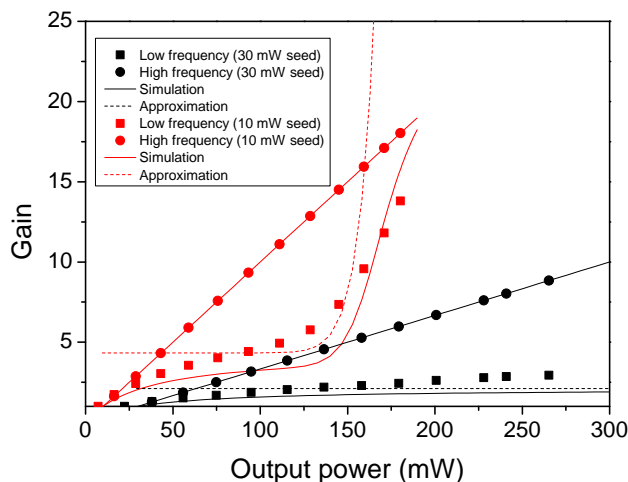


Figure 4.6: Gain of low frequency (10 Hz) and high frequency (100 kHz) modulation in dependence of output power in the ytterbium doped fiber amplifier.

up to an output power of 75 mW. At this point the low frequency gain starts to saturate, but only to increase dramatically at an output power beyond 150 mW. The regime up to 150 mW is dominated by the saturation power of the ytterbium doped fiber, beyond that unabsorbed pump power increases and becomes the dominating effect. As discussed before, equation (3.33) does not properly reflect the increase of the saturation contribution with increasing gain, which can be clearly seen in the parts where the approximated low frequency gain is larger than the measured amplifier gain. As one can see, the approximation fits well as long as the amount of unabsorbed pump power is small and the output power is large compared to the saturation power.

The measured transfer functions shown in Fig. 4.5 were also used to obtain the corner frequency ω_{eff} , as described for the erbium doped fiber amplifier before. In this case no linear behavior can be expected once the residual pump power starts to increase significantly. This is shown in Fig. 4.7. However, when plotting the zero-frequency $\omega_0 = B_s P_s^0(0) + B_p P_p^0(L) + 1/\tau$ against the residual pump power, the result should be linear because the fluorescence lifetime and the seed power are constant. This is shown in Fig. 4.8 (a). Removing the constant part in ω_0 allows

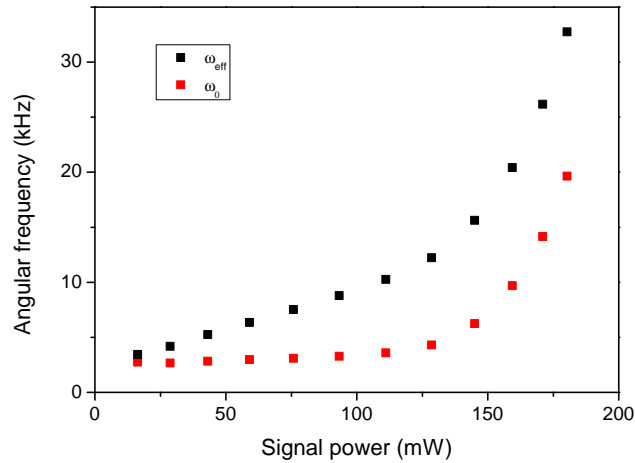


Figure 4.7: Corner frequency ω_{eff} and zero frequency ω_0 in dependence of output power.

to obtain $B_p P_p^0(L)$. With this, a linearized corner frequency $\omega_l = \omega_{\text{eff}} - B_p P_p^0(L)$ can be calculated. Since ω_l does not depend on the residual pump power anymore, it should be linear again, which is confirmed in Fig. 4.8 (b). From the slopes in Fig. 4.8 B_s and B_p can be determined to $B_s = 1.3 \cdot 10^{-14}$ and $B_p = 8.3 \cdot 10^{-14}$. This is comparable to the values obtained from the fiber parameters $B_s = 1.0 \cdot 10^{-14}$ and $B_p = 1.7 \cdot 10^{-13}$. The same process was also carried out for 20 and 30 mW of seed power. In this case the amount of unabsorbed pump light is small, so no reasonable data for B_p can be expected. The results derived for the different seed power levels are shown in Table 4.2.

In chapter 3 the dynamic behavior of the residual pump power was derived as well. Accordingly the dynamic behavior is qualitatively different from the output power. Since no experimental evidence existed, the unabsorbed pump light's frequency response was measured (Fig. 4.9, ytterbium doped fiber, 10 mW average seed power, 155 mW average pump power). The transfer functions show the difference between pump and seed power modulation. Between signal and pump power modulation the phase is flipped by 180° , which corresponds to m_s'' in equation (3.30) being negative. Increasing the seed power decreases the amount of unabsorbed pump power, while increasing pump power also increases the amount of unabsorbed pump power. Since this is exactly as predicted, this measurement is an additional confirmation of the theory.

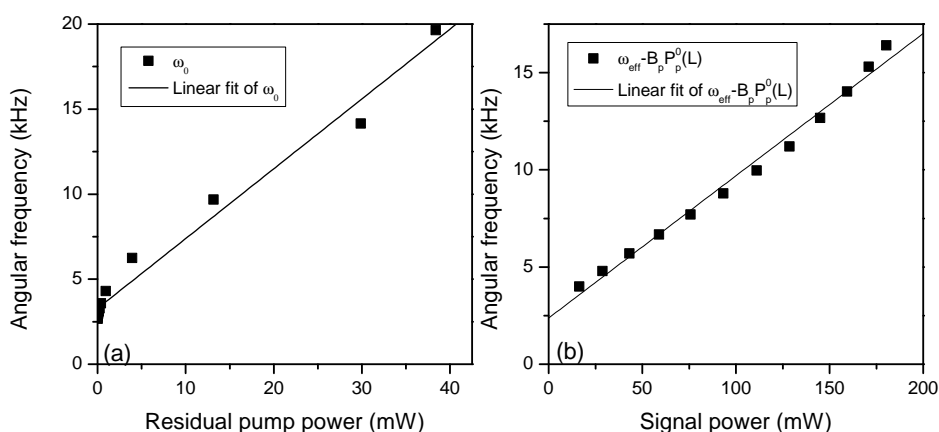
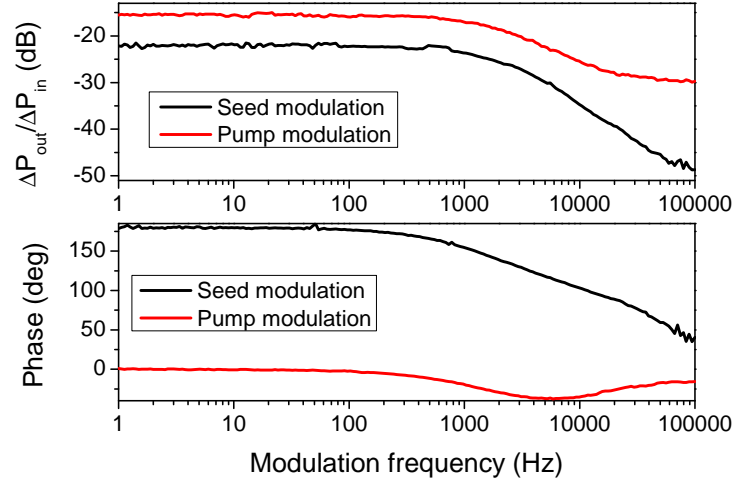


Figure 4.8: (a) ω_0 against residual pump power (b) ω_l in dependence of output power.

Table 4.2: Experimentally obtained parameters for the ytterbium fiber.

Seed power (mW)	B_s	B_p	τ (s)
10	$1.37 \cdot 10^{-14}$	$8.38 \cdot 10^{-14}$	$4.23 \cdot 10^{-04}$
20	$1.12 \cdot 10^{-14}$	$(7.29 \cdot 10^{-13})$	$3.49 \cdot 10^{-04}$
30	$1.16 \cdot 10^{-14}$	$(1.48 \cdot 10^{-12})$	$3.69 \cdot 10^{-04}$

**Figure 4.9:** Ytterbium doped fiber amplifier's frequency response of unabsorbed pump power.

4.3 Summary

The impact of dynamic gain in fiber amplifiers on fiber amplifier output power and residual pump light was analyzed. The simplified estimations based on the analytic model originally developed by Novak and Moesle [16] were used to explain dynamic effects in our ytterbium and erbium fiber amplifiers. It was shown that this approximation is valid as long as the unabsorbed pump power and the (amplified) spontaneous emission is low, which should be the case in most well designed amplifiers.

5 Power Noise

In single frequency laser beams there are two potentially noisy observables: the signal power and the signal phase. While phase noise is relevant when multiple fiber amplifiers are coherently combined (see chapters 6, 7 and 8), the contribution of a fiber amplifier to the output beam's phase/frequency noise is usually negligible compared to the contribution of the free running seed laser (see Tröbs et al. [17] and chapter 7). On the other hand due to the transfer of pump power fluctuations to amplified seed power, the power noise changes significantly in an amplifier and therefore this chapter concentrates on power noise in fiber amplifiers.

Noise sources can be difficult to identify. For example the primary power noise source of the free running advanced LIGO laser system [3] and the very similar amplifier design [12] is still unclear today. Active stabilization is still possible, even if the noise origin is not completely understood. So, this is not necessarily a problem. However, a good comprehension of the major effects helps to develop intrinsically more stable lasers and efficient stabilization schemes.

One major contribution to the amplifier power noise are seed and pump power noise, although at high power levels additional effects like spectral pump noise and incoupling noise might have to be considered as well. Additionally, coherent combination of multiple fiber amplifiers can also influence the relative power noise (RPN)¹ because of residual phase noise and due to the coherent addition of multiple uncorrelated sources.

¹ Throughout this thesis the linear power spectral density is used to describe noise, as it is most commonly used in the GWD community.

5.1 Power Noise of a Single Amplifier

The most obvious noise source in a fiber amplifier is the noise of the launched seed and pump power. Their influences can be related to the output power according to the transfer functions derived in chapter 3. If this is the most significant contribution, the amplifier RPN can be calculated from just seed and pump RPN.

5.1.1 Pump and Seed Noise

The RPN of seed and pump laser diodes is characteristic for each diode type, but it can also be influenced by the environment the diode is operated in. The RPN of three representative fiber coupled 976 nm diodes are shown in Fig. 5.1. The power noise varies greatly between different types, but even among the same type some variation is possible. One major issue are back reflections: the RPN can vary significantly due to back reflected power and therefore different couplers and fiber end faces can already lead to significantly different behavior. While such issues should be avoided as much as possible, some differences even between the diodes of the same type usually have to be accepted. It should be noted that the RPN of the diodes shown in Fig. 5.1 cannot be compared directly as the very stable LC95 diodes are single mode diodes with a maximum power of 600 mW, while the multimode pump module BMU25 delivers 25 W and the nLight Pearl module even 100 W. While a RPN comparable to the LC95 diodes would be desirable, the RPN of fiber coupled high power 976 nm diodes tends to be significantly worse. Better performance should be possible in principle, as the fiber coupled 808 nm diodes used in the laser system for advanced LIGO (JOLD-30-CPXF-1L) reach a performance similar to the LC95 types [63].

In the low power single mode experiments described in the next section the LC95 diodes were used. Before the actual amplifier experiments, the RPN of the diode was characterized. The power of the diode was increased and the output relative power noise was measured (Fig. 5.2). The RPN decreased as the average power was increased. Therefore, the RPN also depends on the output power, and the optimum performance is reached at the design output power.

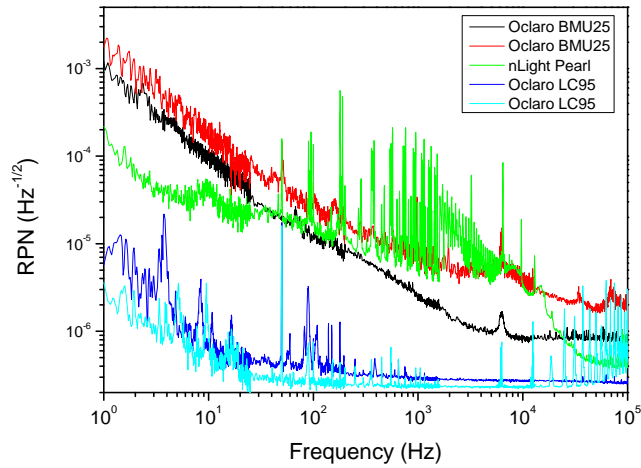


Figure 5.1: RPN of different pump laser diodes. In case of the BMU25 and the LC95 different units of the same type were used at the same operating conditions.

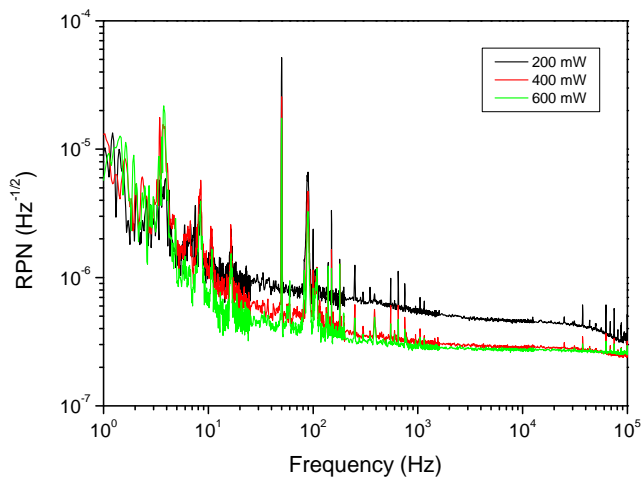


Figure 5.2: RPN of a single mode 976 nm pump diode for different output power.

Generally, one would assume that the noise of two different laser diodes driven by two independent current drivers is uncorrelated. However, this is not obvious, since the diodes are operated in the same laboratory, thus, there could be environmental noise coupling to both diodes symmetrically leading to correlated noise. As this could lead to different results, the assumption was tested by overlapping two pump diodes incoherently on a photo detector (Fig. 5.3). In case of uncorrelated noise, the individual noise contributions S_i can be added geometrically ($S_{\text{total}}(f)^2 = S_1(f)^2 + S_2(f)^2$). As one can see in Fig. 5.4, assuming uncorrelated noise leads to good results and therefore uncorrelated RPN from different pump diodes can be assumed.

5.1.2 Low Power

With this information and the model for the transfer of seed and pump modulation it should be possible to calculate the output power noise from the pump and seed power as long as other contributions are small. The total relative power noise can then be calculated by weighting the RPN of seed and pump by the corresponding transfer function and adding them assuming uncorrelated noise:

$$\frac{S_{\text{amp}}(f)}{P_{\text{amp}}} = \sqrt{\left(\frac{S_{\text{seed}}(f)T_{\text{seed}}(f)}{P_{\text{seed}}}\right)^2 + \left(\frac{S_{\text{pump}}(f)T_{\text{pump}}(f)}{P_{\text{pump}}}\right)^2}. \quad (5.1)$$

Here, $S_{\text{amp}}(f)$, $S_{\text{seed}}(f)$ and $S_{\text{pump}}(f)$ are the linear power spectral densities of the signal, seed and pump power noise and T_{seed} and T_{pump} are the normalized transfer functions.

This was tested using a single mode all-fiber ytterbium doped amplifier operating

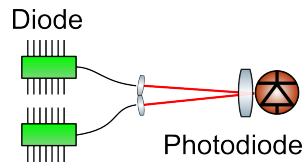


Figure 5.3: Setup to measure the combined RPN of two laser diodes.

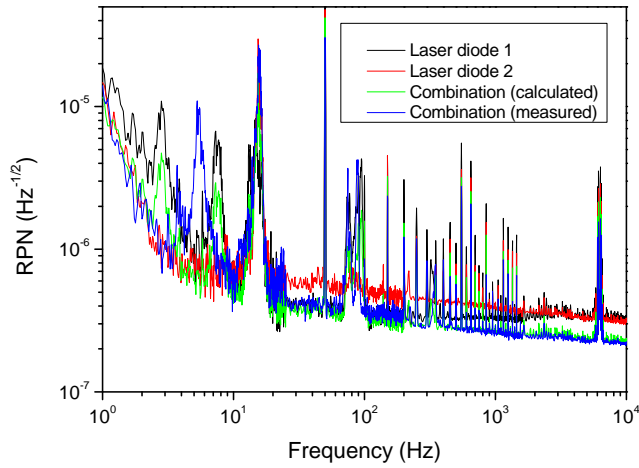


Figure 5.4: RPN of incoherently combined laser diodes.

at 1064 nm (6 μm core diameter). At a seed power of 13 mW and an output power of 160 mW the relative power noise of seed, pump, and amplifier was measured. The transfer functions for seed and pump power modulation were measured and normalized as described in chapter 4. The results are shown in Fig. 5.5. The

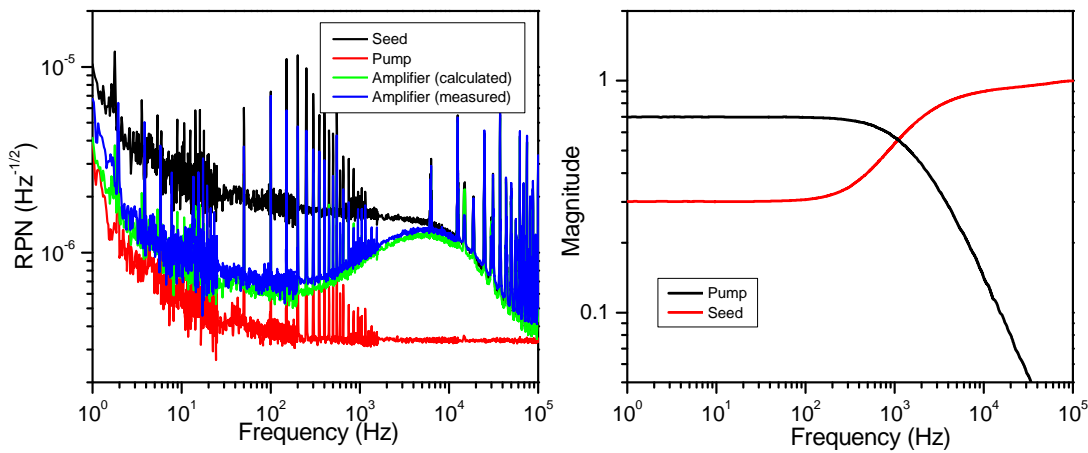


Figure 5.5: Left: RPN of seed laser, pump laser and fiber amplifier and calculated RPN. (13 mW seed, 160 mW output power). Right: Measured normalized transfer functions.

noise can be calculated from the measured transfer functions as described and the calculated amplifier RPN is in excellent agreement with the measured data. However, the transfer function cannot be estimated with the method established in chapter 3, because the output power was 160 mW and the launched seed power was only about 13 mW, which is not enough for a reasonably good estimate of the seed suppression. This is especially important due to the rare case of the seed RPN being a factor of 5 larger than the pump noise. For this reason only the measured transfer function was used.

In a different measurement 35 mW of seed was used with an output power of 250 mW and a launched pump power of 500 mW (Fig. 5.6). In this case the transfer function can be estimated from input and output power. When directly comparing the transfer functions, the error still seems to be quite large. However, the measured amplifier RPN, the RPN calculated with measured transfer functions, and the RPN calculated only from output power are well within the error margin. The mismatch in the affected frequency region is less than a factor of 1.3, which is completely acceptable.

Therefore, the noise coupling in purely single mode all fiber amplifiers is well

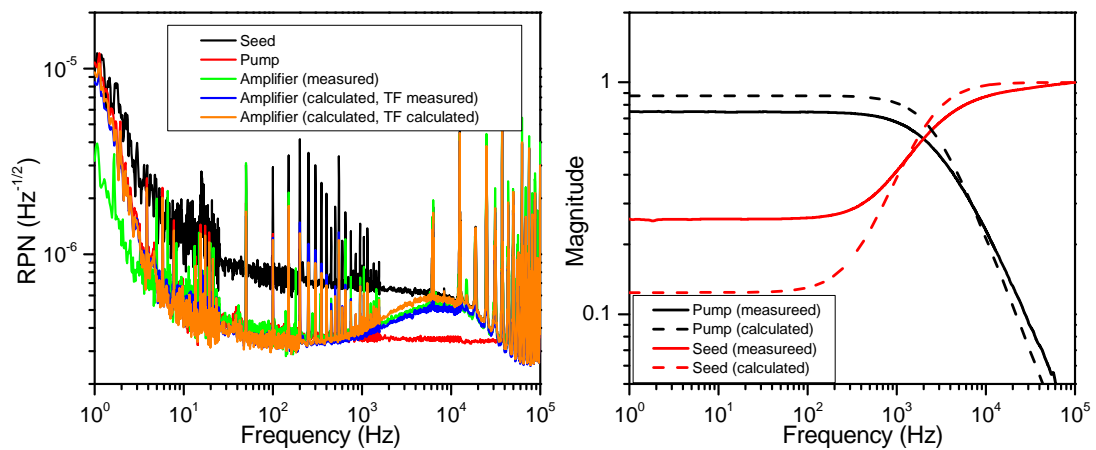


Figure 5.6: RPN of seed laser, pump laser and fiber amplifier (35 mW seed, 250 mW output power). The RPN was calculated using a measured normalized transfer function (blue) and the transfer function (TF) derived from output and input seed power (orange).

understood and the main origins of technical noise are seed and pump power noise. As long as the fiber amplifier is well saturated, there is not even a need to measure the transfer functions.

5.1.3 High Power

For high power fiber amplifiers single mode pump diodes cannot be used due to their limited output power. This also means wavelength division multiplexers cannot be used to couple the pump light into the fibers. These can be replaced either by multimode pump couplers or dichroic mirrors with free space coupling to the fiber. To evaluate the noise properties of such a system, a backward pumped free space coupled single frequency fiber amplifier as depicted in Fig. 5.7 was used [64]. Its maximum output power was 50 W. The pump power was up to 80 W and the seed power was about 1 W. The RPN of the pump, seed (measured at the amplifier output without pumping the amplifier) and the amplifier output at 50 W are shown in Fig. 5.8. As a seed source a non planar ring oscillator (NPRO) was used. However, the measured RPN was above that of a typical NPRO in the low frequency region. This is to be expected as any coupling to a single mode fiber converts beam pointing to power noise. The coupling can probably be optimized, but this was not the limiting factor as will be shown in the following sections. Therefore, no additional attempts to improve the coupling of the NPRO to the fiber were made. The pump diode used here was an nLight Pearl module with significantly higher RPN than the single mode diodes used before.

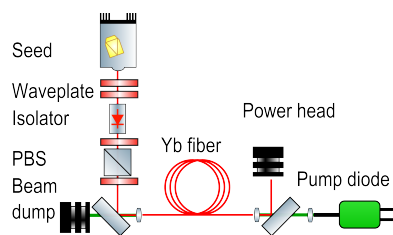


Figure 5.7: Backward pumped free space amplifier.

To calculate the output power noise, the transfer functions were estimated from the output power and the seed suppression factor was approximated by the inverse gain. This is a very good approximation in this case, because output power and launched seed power are very high and the effective area was only a factor of 2.8 larger than in the low power experiments described before ($10\ \mu\text{m}$ instead of $6\ \mu\text{m}$ core diameter). The corner frequency can be estimated to be 120 kHz and the suppression factor should be $1/50$. This combination suggests a very low impact of seed RPN in the measured frequency region. The only noticeable difference between pump RPN and calculated amplifier RPN was near 100 kHz and it matches with the measured amplifier RPN. However, there is a large difference between calculated and measured RPN in the low frequency region. This cannot be caused by direct coupling of seed or pump power noise, because it is larger than either of them. Therefore additional noise contributions must be present in this system.

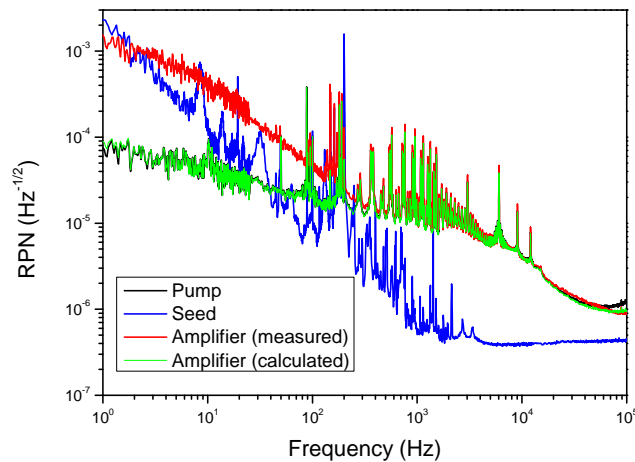


Figure 5.8: Power noise of a free space coupled single frequency, single mode amplifier.

Spectral Pump Noise

Besides power noise there is also frequency or spectral noise of the pump diodes. The coupling of spectral noise to fiber amplifier power noise is easy to understand in principle: small wavelength shifts of the pump diode lead to different pump power absorption, which then couples to the population of the upper laser level and finally the amplifier output power noise. Fortunately, the absorption bands in rare earth doped glass are quite broad compared for example to Nd:YAG, so in a well designed fiber amplifier the impact of spectral noise should be less than that for solid state amplifiers. However, when operating the pump diode on the edge of a strong absorption band (e.g. ytterbium at 976 nm) strong coupling is possible.

For now, one could argue that the low frequency increase in Fig. 5.8 is caused by pump spectral noise. To check this assumption the amplifier was operated at an output power of 30 W and the wavelength of the pump diode was tuned by changing its temperature. For each temperature the RPN of the amplifier and the RPN of the pump diode as well as its optical spectrum was measured. In the process the wavelength was swept over the 976 nm absorption band, so the impact of pump spectral noise changes depending on the average operating wavelength of the pump diode. The result is shown in Fig. 5.9. The pump RPN did not change noticeably during this process, therefore only one curve is shown in Fig. 5.9 for better clarity. It can be seen that the temperature and thus the center wavelength had no impact on the RPN at low frequencies. Therefore, this contribution was not caused by spectral noise. On the other hand there was a small difference in the high frequency region. In case of 37°C the RPN was lowest and for 35°C and 40°C it was slightly increased. When comparing the power spectral density of the pump power with the ytterbium absorption, one notices that at 37°C the pump wavelength was exactly at the center and that the ytterbium absorption band was broader. Therefore, there was no coupling to output power in first order. On the other hand for 35°C and 40°C the pump spectrum was closer to the edge of the ytterbium absorption band, so the coupling was of first order. Of course one could argue that such a small change is not significant, however, a temperature dependence of the amplifier RPN was reproduced at other operating power as well and always in this frequency range.

Since only in the best case the amplifier RPN was equal to pump RPN, which was measured at the same time, pump spectral noise is the most reasonable assumption to explain this effect.

Incoupling noise

While the measurement indicates an influence of pump spectral noise at high frequencies, it does not explain the increase at low frequencies. However, remembering the increased seed power RPN after passing through the single mode fiber a similar effect is likely. The multimode pump has to be coupled into the cladding of the fiber and therefore pointing instabilities will lead to additional power noise of the power in the fiber due to variations of the incoupling ratio. Due to the multimode character the impact could actually be much worse than for the single mode NPRO. Because of the strong absorption of 976 nm in the active fiber this can unfortunately not be measured directly in this system.

Further investigation of incoupling noise using appropriate passive fibers will be a valuable topic for future investigation. Since different coupling methods could also influence the severity of the effect, free-space and all-fiber configurations should also be compared.

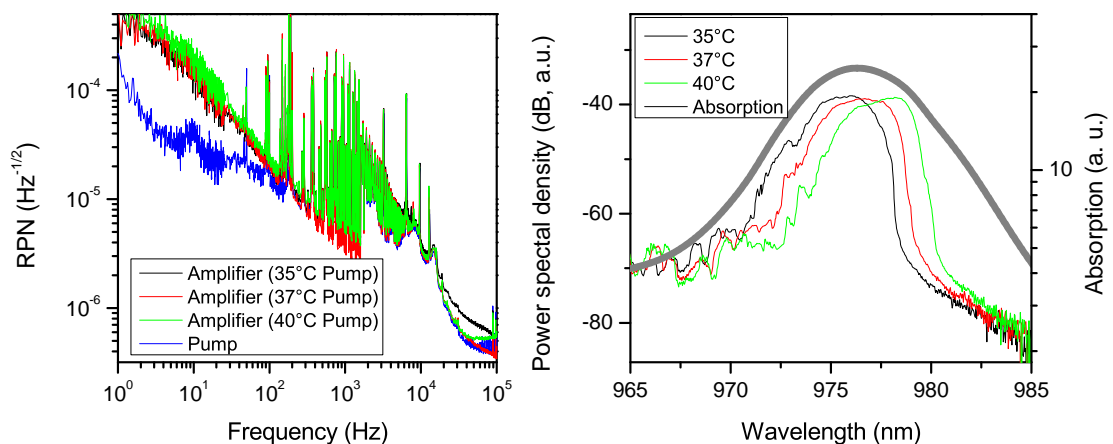


Figure 5.9: (a) Additional noise contribution in the 10 - 100 kHz region in dependence of temperature (b) Pump spectra at these temperatures and ytterbium absorption band.

5.2 Power Noise of Coherently Combined Beams

Coherent beam combining adds additional noise components, which have to be considered for the power noise. The main issue to consider is residual relative phase noise of the two amplifiers, because it leads to additional power noise according to equation (2.2). To coherently combine multiple fiber amplifiers an active feedback loop to control the phase is mandatory, but even then the control loop cannot control the phase perfectly. In case of phase detection errors or noise, the control loop itself introduces phase noise. Even if the phase detection is working perfectly, the operating bandwidth of feedback loops is finite and above the unity gain frequency the phase cannot be stabilized. This leads to residual relative phase noise between the overlapping fields. This residual phase noise is converted to power noise and thus leads to an increase of power noise of the combined beam.

Ideally, the impact of phase noise converted to power noise is very small compared to the amplifier RPN originating from pump and seed power noise. In this case the phase mismatch can be neglected and the RPN of the single amplifier dominates. As shown earlier the amplifier noise at low frequencies is typically dominated by pump RPN. Since different pump diodes are used for each amplifier, this noise component is uncorrelated. In case of equal output power and equal power noise of n individual amplifiers the total noise is $S_{\text{total}} = \sqrt{S_1^2 + S_2^2 \dots + S_n^2} = \sqrt{n}S$. On the other hand the power increases linearly: $P_{\text{total}} = nP$. Therefore, the RPN $S_{\text{total}}/P_{\text{total}}$ decreases by a factor of \sqrt{n} in the low frequency region dominated by the pump power noise. At high frequencies seed RPN is dominating, which is correlated, because one common seed is used. Therefore, the noise is added linearly and no decrease of RPN can be expected in the high frequency region.

These assumptions were verified in a very simple low power system¹ (Fig. 5.10). The seed was split into two channels (10 mW each) and the amplifiers were pumped by two different pump diodes (350 mW). The output power of a single amplifier was about 130 mW. The phase stabilization was a very simple lock-in based control loop

¹ A more realistic prototype for coherent beam combining in a laser system for GWD is presented in chapter 7.

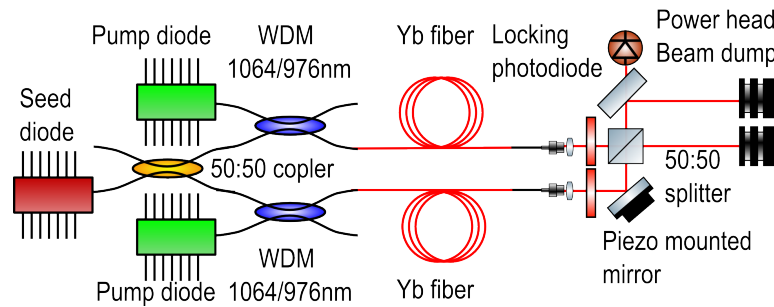


Figure 5.10: Setup for the comparison of CBC RPN and the single amplifiers' RPN.

with a phase modulation frequency of 10 kHz. The PID parameters were manually tuned to optimize the performance, but no detailed analysis of this control loop was realized. The unity gain frequency can be estimated to be slightly below 1 kHz.

The resulting RPN of the combined beam was increased over the single amplifiers (Fig. 5.11). This was due to imperfect phase control of the overlapping fields. At first glance it might seem odd that there is no excess noise at frequencies above 1 kHz although these frequencies are not even in the control loop bandwidth. However, the relative phase noise of two fiber amplifiers S_ϕ is typically proportional to $1/f$ (see for

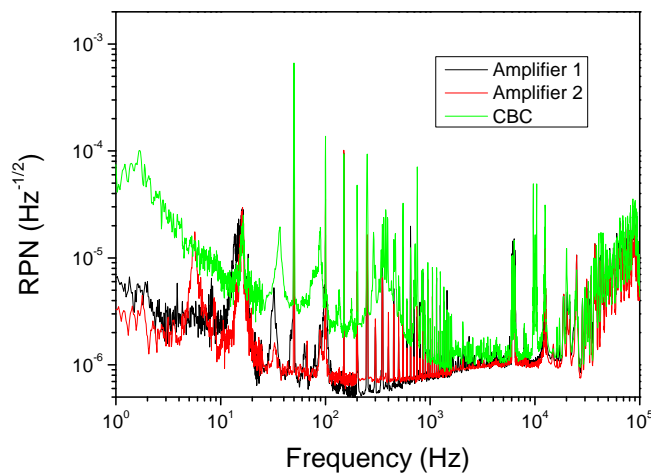


Figure 5.11: Comparison of CBC RPN and the single amplifiers' RPN.

example the measurement in chapter 7). Therefore, phase noise at high frequencies becomes small enough that there is no noticeable coupling to power noise. On the other hand the $1/f$ trend compensates the increasing phase noise suppression of the control loop towards low frequencies and thus enables the coupling of phase noise to power noise at low frequencies.

The performance was still much better than the 50 W single amplifier and therefore this effect was only noticeable because of the low noise pump diodes used in this experiment. It also shows decent results can already be achieved with very simple off the shelf control loops and comparatively slow actuators; more care should be taken, if the RPN is critical.

On the other hand slightly decreased RPN is to be expected, if the control system does not add significant RPN. As this can only be observed, if pump RPN is the dominant noise source, the pump noise was artificially increased by adding current noise to the pump diodes. The result can be seen Fig. 5.12. The combined RPN is slightly decreased as expected. However, with only two amplifiers the effect is only a factor of $\sqrt{2}$ and therefore significant improvements can only be expected for a high number of amplifier channels.

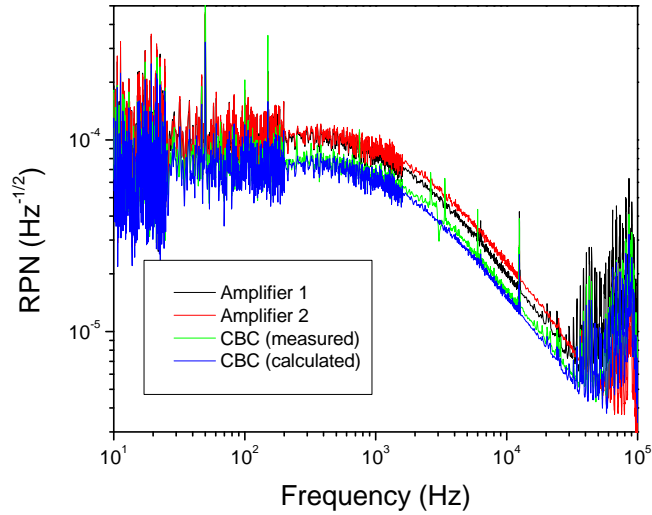


Figure 5.12: Comparison of CBC RPN and the single amplifiers RPN, the pump RPN was artificially increased.

5.3 Summary

In this chapter the most relevant power noise sources in fiber amplifiers were discussed. Two major influences are pump and seed power noise. Potential additional influences like incoupling noise and pump spectral noise were discussed as well as they can have non negligible contributions in high power amplifiers. CBC enables the coupling of phase noise to the overall RPN, however, if the dominant noise source is pump power noise, CBC can also decrease the RPN in this frequency region. Overall, the coupling mechanisms in fiber amplifiers are now equally well understood as in bulk lasers, which is quite remarkable given the amount of development work that went into the noise characterization of bulk solid state lasers and amplifiers [63].

6 Phase Modulation

As already discussed in the previous chapters, a change of pump or seed power changes the population of the upper laser level, which will eventually change the output power. But besides this influence on the signal power an influence on the signal phase is also possible due to dynamic refractive index changes in fiber amplifiers. In the past the refractive index change Δn in fiber amplifiers and corresponding shifts of the signal phase have been investigated in time domain. From these time domain measurements [20, 65], it is known that the optical phase shift in most rare earth doped active fibers is a result of the wavelength dependent gain changes and Kramers-Kronig-Relations (KKR) [65] and temperature contributions. Besides mechanical vibrations these refractive index changes contribute to phase noise [50] and beam quality degradation, [44] but they can also be exploited by using fiber amplifiers as phase actuators [65, 66].

6.1 Phase Shift Induced by Kramers-Kronig-Relations

To understand the physical origin of the coupling mechanism via KKR, it is useful to reconsider the origin of the refractive index itself. Matter consists of positive and negative charges. If a light wave travels through matter, the charges are separated and electric dipole moments are generated. Together these dipole moments form the polarization. The polarization follows the electro-magnetic field according to the convolution [67]

$$P(t) = \varepsilon_0 \int u(\tau) E(t - \tau), \quad (6.1)$$

where $u(\tau)$ is the temporal response of the polarization. In the Fourier domain this convolution is simply the product of the susceptibility $\chi(\omega)$ and the Fourier transform of the field:

$$P(\omega) = \varepsilon_0 \chi(\omega) E(\omega). \quad (6.2)$$

Since the polarization cannot react to a change ΔE , before it happens, the system is causal and therefore $u(\tau < 0)$ has to be 0. This means the Fourier transform of $u(\tau)$ – the susceptibility $\chi(\omega)$ – is analytic. Therefore, the imaginary part of χ can be calculated using the Hilbert transform. This leads to the equations called the KKR [68].

Because the refractive index depends on the susceptibility (in case of weak absorption $n(\omega) \approx 1 + \chi(\omega)/2$), the refractive index can be calculated, once the absorption spectrum is known. A change of absorption or gain will therefore change the refractive index $n(\omega)$. The resonances responsible for the various absorption bands in matter can usually be described with the complex Lorentz function

$$L_{\omega_0}(\omega) = \frac{i\alpha}{1 - i\frac{\omega - \omega_0}{\Delta\omega}}, \quad (6.3)$$

where ω_0 is the resonance frequency, α the oscillator strength and $\Delta\omega$ the linewidth of the resonance. An exemplary plot of the real and imaginary part of the refractive index around such a resonance is shown in Fig. 6.1. From this plot one would only expect a significant refractive index change near $\omega = \omega_0 \pm \Delta\omega$ and no refractive index change directly at the resonance or far from the resonance. However, in many rare earth doped glasses this is not the case because of very strong resonances in the ultraviolet [18, 69, 70]. While these resonances are not directly involved in the laser transition, the transition strength of the ultraviolet resonances depends on the number of ions in the upper laser level. Because these resonances are very strong, their impact on the refractive index can still be observed in the near infrared – e.g. at 1064 nm and 1550 nm.

This contribution to the refractive index change depends on the number of ions in the upper laser level, which changes in time like a low pass as shown in chapter

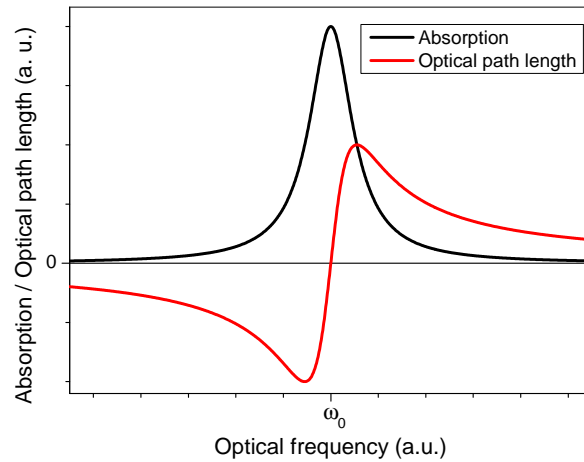


Figure 6.1: Phase shift induced by a resonance.

3. At 1550 nm, employing the KKR induced phase shift of ytterbium doped fibers for coherent beam combining has been demonstrated [66, 71]. The KKR induced phase shift in erbium fibers was measured by Digonnet et al. for wavelengths from 760 nm through 970 nm [65]. So far, the wavelength range around 1064 nm, which is important for high power amplifiers, was not investigated. Therefore, the phase response of pumped erbium doped fibers at 1064 nm and their suitability as an all fiber phase actuator in coherent beam combining was studied. The temporal dynamics of this effect was also measured as a transfer function, which was then compared with the predictions from chapter 3.

6.1.1 Erbium Fiber Induced Phase Shift at 1064 nm

First, an erbium fiber as a potential phase actuator at 1064 nm was investigated. As shown in Fig. 6.2, a 1064 nm distributed feedback (DFB) laser diode with 2 MHz linewidth was fed into a fiber based Mach-Zehnder interferometer with 3.4 m erbium doped fiber (nLight Liekki Er30-4/125) in one arm and a passive balancing fiber in the other. The erbium fiber was core pumped by two polarization combined 1480 nm diodes. The balancing fiber was used to ensure the length difference between both

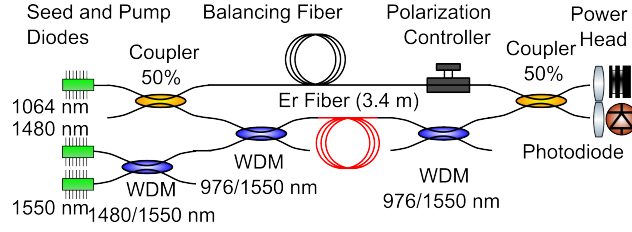


Figure 6.2: Fiber based Mach-Zehnder interferometer used in the experiment.

arms was less than 2 cm to avoid excessive coupling of the DFB diode's frequency noise into the output phase signal. Because of the narrow emission linewidth, better balancing was not required for the measurements, but could potentially reduce the noise coupling.

To measure the effect of erbium pump modulation on the optical phase at 1064 nm, a step modulation was added to the 1480 nm pump power and the output of the interferometer was monitored with a photodiode. The phase was directly retrieved from the photodiode signal $U(t)$, using the equation

$$\Phi = \arcsin \left(\frac{2U(t) - U_{\max} - U_{\min}}{U_{\max} - U_{\min}} \right). \quad (6.4)$$

Since the interferometer was stable enough on a second time scale, it was not stabilized actively. Note that the absolute sign and integer multiples of π are not retrieved explicitly with this method. To obtain a well defined trace the modulation parameters used in the experiments resulted in a phase shift in the range of π .

Two different time scales were observed: a fast but small step on sub-ms time scale followed by a slow drift in the second range with a large magnitude (Fig. 6.3). The slow drift can be attributed to thermal effects (see section 6.2). If the fast phase change is caused by the KKR contribution to the refractive index, it should be proportional to the population of the upper laser level [65].

The change of population is described by the rate equations. Therefore, it should be possible to use the model derived in chapter 3. The equations for the resulting

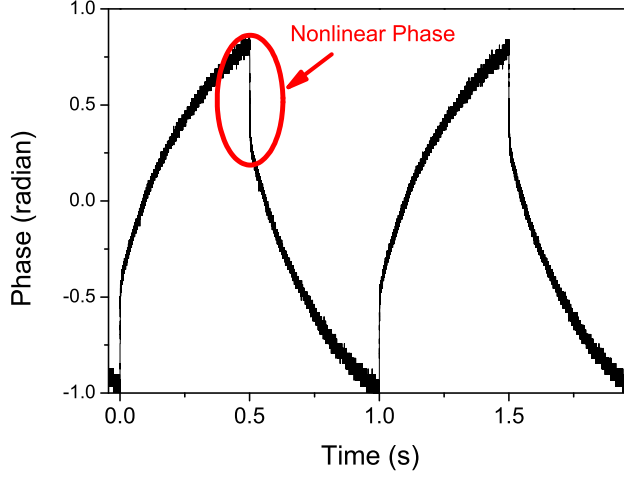


Figure 6.3: Phase shift induced by the erbium fiber (40 mW average pump power ± 8 mW step modulation). Fast: KKR induced refractive index change. Slow: thermal drift.

modulation are

$$N_2^0 \delta = m_p \frac{[P_p^0(0) - P_p^0(L)]}{\sqrt{\omega^2 + \omega_{\text{eff}}^2}} \quad (6.5)$$

in case of pump modulation and

$$N_2^0 \delta = m_s \frac{[P_s^0(0) - P_s^0(L)]}{\sqrt{\omega^2 + \omega_{\text{eff}}^2}}, \quad (6.6)$$

in case of seed modulation with the N_2 modulation fraction δ .

In the case of low pump power and no signal, as described by Fotiadi et al. [20, 66], the dominating time scale is the fluorescence lifetime τ , because the output power and the unabsorbed pump power are zero, thus $\omega_{\text{eff}} = 1/\tau$. In the case of erbium τ is about 10 ms. From an exponential fit to the fall time at 10 mW average pump power and 9 mW modulation amplitude, a decay time of 10.4 ms was deduced.

But this approximation only applies for very low pump power levels. To observe the effective lifetime in dependence of average pump power, the modulation power

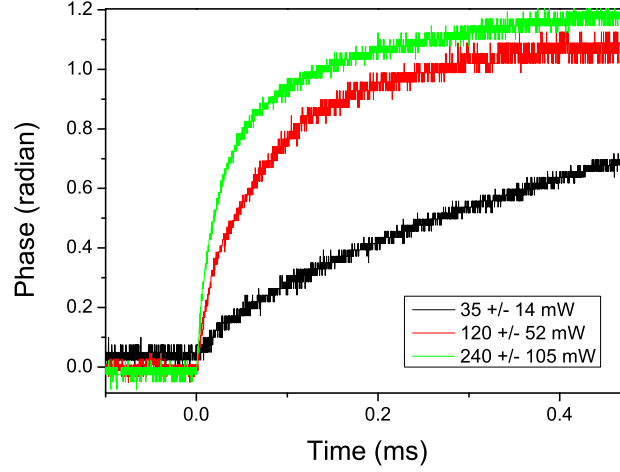


Figure 6.4: Pump modulation (increased modulation power relative to pump power)

was increased proportionally to the average power as shown in Fig. 6.4. The response time decreased with average pump power. The model developed in chapter 3 can also be used to explain this effect. In case of high pump power, the amount of unabsorbed pump power $P_p^0(L)$ increases and therefore also ω_{eff} increases. Only in the very low pump power limit, when the pump light is completely absorbed, the response is dominated by the natural fluorescence lifetime.

As the average pump power was increased, the phase shift per mW modulation decreased (Fig. 6.5). Increasing average pump power decreases the change in inversion and thus also decreases the refractive index change. This also means that the gain in a potential control loop depends on the operating point. Using the equations from chapter 3 it becomes clear that there are actually two reasons for this effect: rewriting $m_p = P_p^{\text{mod}}/P_p^0(0)$ equation (6.5) becomes

$$N_2^0 \delta = \frac{P_p^{\text{mod}} \left[1 - \frac{P_p^0(L)}{P_p^0(0)} \right]}{\sqrt{\omega^2 + \omega_{\text{eff}}^2}}. \quad (6.7)$$

When increasing the pump power either the unabsorbed pump power (no seed) or

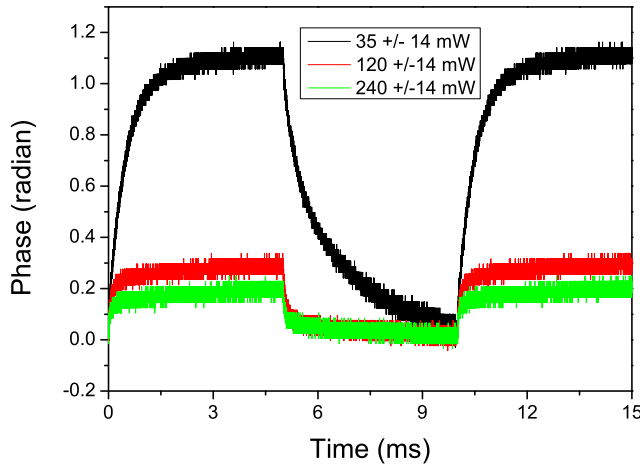


Figure 6.5: Pump modulation (fixed modulation power)

the amplifier output power (with seed) increases. This leads to an increased ω_{eff} , which is usually desired, but already decreases the actuator range. Additionally, the term $[1 - \frac{P_p^0(L)}{P_p^0(0)}]$ approaches zero as the fraction of absorbed pump light becomes small. This second effect is prevented by an additional seed, which reduces the amount of unabsorbed pump light and $[1 - \frac{P_p^0(L)}{P_p^0(0)}]$ stays close to one.

Another option to modulate the excitation of an erbium amplifier is via a modulated 1550 nm seed. If the seed is used without any pump light, it acts like a pump and increases the inversion. If the amplifier is pumped and seeded at the same time, increasing the seed power decreases the inversion. Therefore, the direction of the KKR-induced phase shift should change between both regimes. When stabilizing the interferometer by tuning the wavelength of the 1064 nm seed, these different signs were apparent in the 1064 nm actuator signal. The 1550 nm seed beam was then modulated with an average power of 6 ± 5 mW and no pump. In this case, the phase shift was slow like in the low pump power case (Fig. 6.6). When the seeded amplifier was pumped with 600 mW, the phase response became significantly faster and the amplitude of the phase shift per mW seed modulation did not decrease.

The larger phase shift in the amplified regime can also be explained by the seed

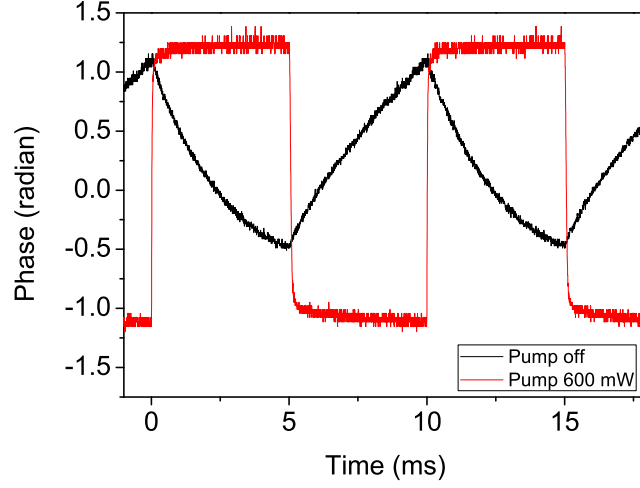


Figure 6.6: Seed modulation with and without pump.

equivalent of equation (6.7)

$$N_2^0 \delta = \frac{P_s^{\text{mod}} \left[1 - \frac{P_s^0(L)}{P_s^0(0)} \right]}{\sqrt{\omega^2 + \omega_{\text{eff}}^2}}, \quad (6.8)$$

which is of the same type. However, for seed power modulation the absolute value of $\left[1 - \frac{P_s^0(L)}{P_s^0(0)} \right]$ can become much larger, if $P_s^0(L) \gg P_s^0(0)$. The equation also predicts two regimes for seed modulation, depending on the pump power the seed can either be amplified or absorbed ($P_s^0(L) < P_s^0(0)$). This means for low seed and high pump power a fast phase response time is obtained without compromising the KKR induced phase shift per mW modulation power.

Altogether, the observed behavior of the fast phase change and its dependence on pump and seed power fit to the response predicted by the rate equations and the model developed in chapter 3. This indicates the fast phase shift observed here is induced by the KKR.

6.1.2 Ytterbium Fiber Induced Phase Shift: Frequency Domain

For comparison with the results from chapter 3 a direct measurement of the frequency dependent transfer from seed and pump modulation to the signal phase is most useful.

For this measurement the opposite wavelength combination was used: a 1550 nm probe laser was used in a Mach-Zehnder configuration to detect the refractive index change induced in an ytterbium doped fiber (Fig. 6.7). Again, the probe wavelength was not amplified in the ytterbium fiber and therefore not affected by the gain or group velocity effects. One could argue that the phase shift does not have the same magnitude at 1064 nm – which is true – but only a frequency independent conversion factor is expected. Due to large the absorption bands in the ultraviolet, a change of the N_2 population causes a phase shift at 1064 nm as well as 1550 nm [65], therefore the temporal dynamics should be the same for both wavelengths.

Due to the short measurement times for the time domain traces, there was no need to stabilize the Mach-Zehnder interferometer in the previous measurements. But to measure a frequency response down to 0.1 Hz stabilization is required, because a stable operating point is necessary throughout the measurement. This was realized by using unequal interferometer arm lengths (~ 2 cm) and a mid-fringe feedback loop controlling the current of the 1550 nm DFB diode, which tunes its frequency

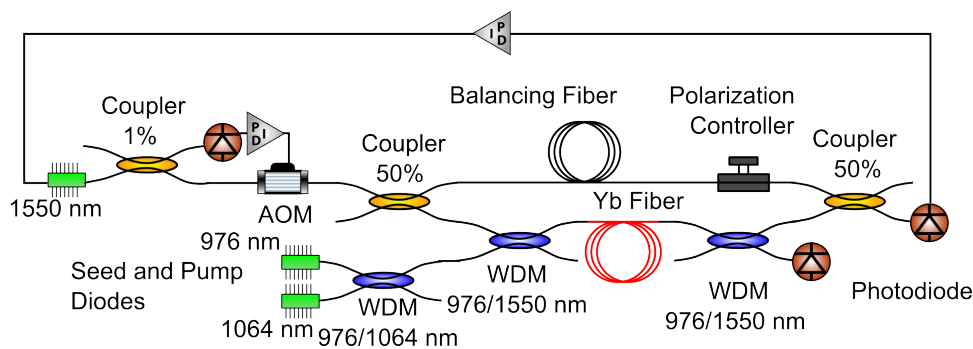


Figure 6.7: Phase measurement of an ytterbium doped fiber amplifier pumped at 976 nm and seeded by a 1064 nm DFB diode. Additionally, a 1550 nm single frequency probe beam was used in a Mach-Zehnder configuration to measure the refractive index change.

and power. As a power modulation of the probe signal is undesired, an acousto optic modulator (AOM) was used together with a second feedback loop to remove this power modulation. Then the 976 nm pump or the 1064 nm seed power were modulated and the control and error signal of the first feedback loop were monitored.

If the model is suitable, both optical phase transfer functions, i.e. seed and pump power modulation, should be a low pass with the same corner frequency as the output power transfer function for pump modulation. The measured transfer functions are shown in Fig. 6.8 for 105 mW average pump power and 10 mW average seed power. As predicted, all of them show a low pass behavior and almost the same corner frequency. Compared to the output power, the phase transfer functions show additional features in the low frequency range up to 3.5 Hz. These features can be attributed to thermal effects, which are not accounted for in a model only based on KKR. These effects will be treated in section 6.2 instead.

Additionally, there should be a 180° phase flip for seed power modulation between amplified and absorbed regime, because the phase shift changes its sign between both regimes. To verify this, the influence of seed modulation on the refractive index including pump light and without the pump were measured as shown in Fig. 6.9

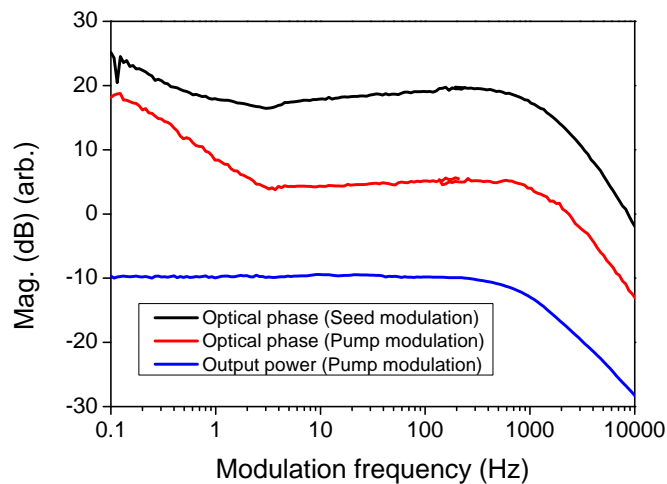


Figure 6.8: Frequency response of the 1550 nm phase / refractive index change.

(black, red). As predicted, there was a phase flip of 180° between both regimes. When increasing the pump power the magnitude of the phase shift decreased at first, before it increased again.

Nevertheless, thermal effects are noticeable in the low frequency region (<1 Hz), although this was a very low power fiber amplifier and the temperature change was very small. For this reason temperature could become the dominating contribution in higher power amplifiers. Therefore, additional experiments and simulations dedicated to the temperature contribution of the refractive index were carried out as described in the next section.

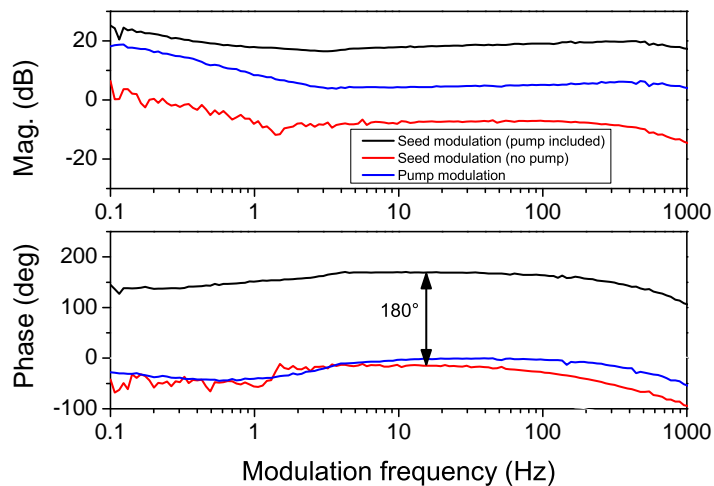


Figure 6.9: The effect of seed modulation on the optical phase with and without pump light (black, red). For comparison the effect of pump modulation is also shown (blue).

6.2 Temperature Induced Phase Shift

Amplification of an optical signal in a fiber amplifier introduces heat into fibers, which increases the temperature. Since the refractive index depends on the temperature, the optical length of the fiber changes.

The energy difference between the pump photons and the signal photons leads to the heat deposition in the fiber. This effect is called quantum defect heating and it is the most common way to model heat load in fiber amplifiers. While it is one of the major effects, it does not always lead to useful results.

This can be shown by examination of the heat contribution in the experiment described in the previous section. When the pump power was modulated, the sign of the temperature induced phase shift and KKR induced phase shift were the same and the temperature induced refractive index change was usually larger than the KKR induced refractive index change as depicted in Fig. 6.3. Assuming pump absorption saturation and neglecting the amplifier saturation due to ASE, increasing seed power would always increase the temperature, if the quantum defect was the only source of heat.

But interestingly, the measurement of the transfer function for seed modulation on optical phase suggests otherwise, since between amplified and absorbed regime the low frequency temperature contribution also flipped its phase as can be seen in Fig. 6.9. Furthermore, the sign of the phase change for seed power modulation without pump light is the same as for pump power modulation. Therefore, a seed power increase increased the fiber's temperature, when the pump diode was switched off, and decreased the temperature, when the pump diode was switched on. This is in contrast to a pure quantum defect heating model.

Similar effects have been observed in many solid state lasers: the heat load decreases, once laser or amplifier operation starts [72, 73]. Reasons for this behavior include the quantum efficiency, concentration quenching, non-radiative sites and energy transfer upconversion, which can lead to additional heat load [73]. Thus, increasing seed power can decrease or increase the heat load depending on the regime and the dominating thermal effects in the amplifier. Therefore, the magnitude and

sign of seed modulation is less predictable than for pump modulation and while most thermal simulations for fiber amplifiers assume quantum defect heating today, this might be not correct in many of cases.

6.2.1 Heat Diffusion in Fibers

In the experiments presented so far, the temperature contribution to the optical phase was only considered as a slow low pass, which is negligible at frequencies above 10 Hz, because in this region the KKR induced phase shift took over. But what if the KKR induced phase shift is very small, for example, because the amplifier is almost saturated? Since an accurate modeling of the thermal effects in a fiber also has to account for the heat diffusion through the fiber, the transfer function of the thermally induced phase shift could be more complex than just a low pass with a corner frequency around 1 Hz. To understand the impact of diffusion the time dependent heat equation has to be solved:

$$c_p(r)\rho(r)\frac{\partial T(r,t)}{\partial t} = \frac{1}{r}\frac{\partial}{\partial r}\left[rk(r)\frac{\partial T(r,t)}{\partial r}\right] + q(r,t). \quad (6.9)$$

Here $T(r,t)$ is the temperature, k the thermal conductivity, ρ the density of the material, c_p the specific isobaric heat capacity, and q is the heat density. A model for the static temperature distribution ($\frac{\partial T(r,t)}{\partial t} = 0$) inside a pumped fiber was developed by Brown et al. [74]. Assuming uniform heating in the core and no heating in the cladding leads to the differential equations

$$0 = k\frac{1}{r}\frac{\partial}{\partial r}\left(r\frac{\partial T(r)}{\partial r}\right) + q_0 \quad (6.10)$$

for the core and

$$0 = k\frac{1}{r}\frac{\partial}{\partial r}\left(r\frac{\partial T(r)}{\partial r}\right) \quad (6.11)$$

for the cladding. Assuming the fiber is subject to Newton's law of cooling with a heat transfer coefficient h at the interface between silica and air ($r = r_0$) the

equation

$$\frac{\partial T(r,t)|_{r=r_0}}{\partial r} = \frac{h}{k}(T(r_0) - T_{\text{air}}) \quad (6.12)$$

leads to a function for the temperature inside the core ($T_I(r)$) and in the cladding ($T_{II}(r)$):

$$\begin{aligned} T_I(r) &= T_0 - \frac{q_0 r^2}{4k} \\ T_{II}(r) &= T_0 - \frac{q_0 r_{\text{core}}^2}{4k} - \frac{q_0 r_{\text{core}}^2}{4k} \ln\left(\frac{r}{r_{\text{core}}}\right), \end{aligned} \quad (6.13)$$

where r_{core} is the core radius and r_{clad} is the cladding radius. These equations show that the temperature profile is parabolic in the core and logarithmic in the cladding. The temperature at the center can be related to the environment temperature T_{air} by

$$T_0 = T_{\text{air}} + \frac{q_0 r_{\text{core}}^2}{4k} \left[1 + 2 \ln\left(\frac{r_{\text{clad}}}{r_{\text{core}}}\right) + \frac{2k}{r_{\text{clad}} h} \right]. \quad (6.14)$$

At this point the steady state temperature distribution is described analytically. However, the equation becomes more complex when also considering the time dependent influence on the phase shift. The homogeneous heat equation

$$\rho c_p \frac{\partial T(r,t)}{\partial t} = k \nabla^2 T(r,t) \quad (6.15)$$

can be solved by separating the variables $T(r,t) = T(r)U(t)$, which leads to the equation

$$\frac{1}{U(t)} \frac{\partial U(t)}{\partial t} = \frac{D}{T(r)} \nabla^2 T(r) = C, \quad (6.16)$$

with a constant C and the thermal diffusivity $D = k/(\rho c_p)$. The solution of these differential equations are exponential decay and, in case of radial symmetry, the Bessel functions. But there is no closed solution for the inhomogeneous time dependent

radial heat equation. Davis et al. [19, 75] derive the properties of the phase shift for ultrafast laser systems using a Bessel series. Especially the time required until equilibrium temperature is reached after the pulse gives a good overview of the involved timescales. However, they did not calculate the transfer functions, which are of interest here.

The results presented in this chapter were obtained by solving the radial heat equation numerically using the finite volume method [76]. The temperature $T(r,t)$ was calculated for a constant average heat density in the core with a sinusoidal modulation ($q(t) = q_0 + q_{\text{mod}} \sin(\omega t)$ with $q_0 = 1/(4r_{\text{core}}^2 \pi) \text{W/m}$ and $q_{\text{mod}} = q_0/10$), as this is a good approximation for a fiber amplifier with modulated pump power. In the representative calculation shown in Fig. 6.10, the response of the radial temperature profile depends on the heating power's modulation frequency ω .

For frequencies lower than approximately 1 Hz the dominating effect is the increase and decrease of the average temperature, which can be seen in Fig. 6.10 (top). On the other hand, for frequencies around 40 Hz (Fig. 6.10, bottom), the temperature change in the center of the fiber is much larger than the temperature change in the outer regions. Therefore, the radial distribution changes significantly. Comparing the lines of equal temperature on short timescales (Fig. 6.10, bottom), the time the heat needs to travel through the glass becomes noticeable. For example, the maximum temperature at $r = 8 \mu\text{m}$ is reached after 8 ms, while the maximum temperature at $r = 50 \mu\text{m}$ is not reached until additional 3 ms have passed. This delay is relevant for the phase shift between heating power and temperature, which is critical for control systems stabilizing the optical phase but also when considering mode conversion via a thermal index grating.

This frequency dependence can be described with transfer functions. These were calculated by modulating the heating power with frequencies from 0.02 Hz to 100 kHz. Then, a sine fit was used for each frequency and radial position (r/r_0) to obtain magnitude and phase of the resulting temperature modulation. The result is shown in Fig. 6.11. Because the lateral dynamic of the heat distribution depends on the modulation frequency, the transfer functions depend on the radial position.

The only temperature directly experimentally accessible is the one at the fiber

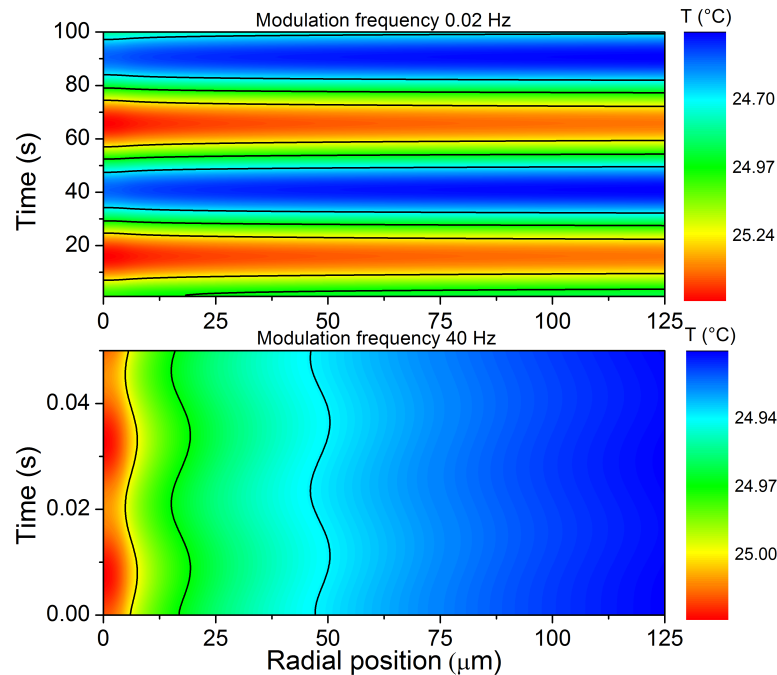


Figure 6.10: Temperature as a function of radial position and time for 0.02 Hz modulation (top) and 40 Hz modulation (bottom).

boundary r_0 . Here, the transfer function is very similar to a simple low pass, although the magnitude decreases faster than that for frequencies larger than 5 Hz. The corner frequency at 0.1 Hz corresponds to heating up and cooling down the complete fiber and is possibly the reason why thermal effects in fibers are often considered as slow. But this is not the whole truth, as in the center of the fiber, where diffusion actually plays a role, the transfer function shows additional features in the region from 1 Hz to about 2 kHz. This is not simply a low pass filter with a distinct cut-off frequency, but the magnitude continues to decrease, although at a much lower rate than in a low pass. The actual rate and the frequency cutoff depend on the radial position in the fiber. When moving away from the fiber center, the slope increases and the cutoff shifts to lower frequencies as well. The same behavior can be seen in the phase, which is related to the magnitude via causality. At 1 Hz the phase shift approaches -90° . In the core the phase shift then changes back to -25° , before it increases again.

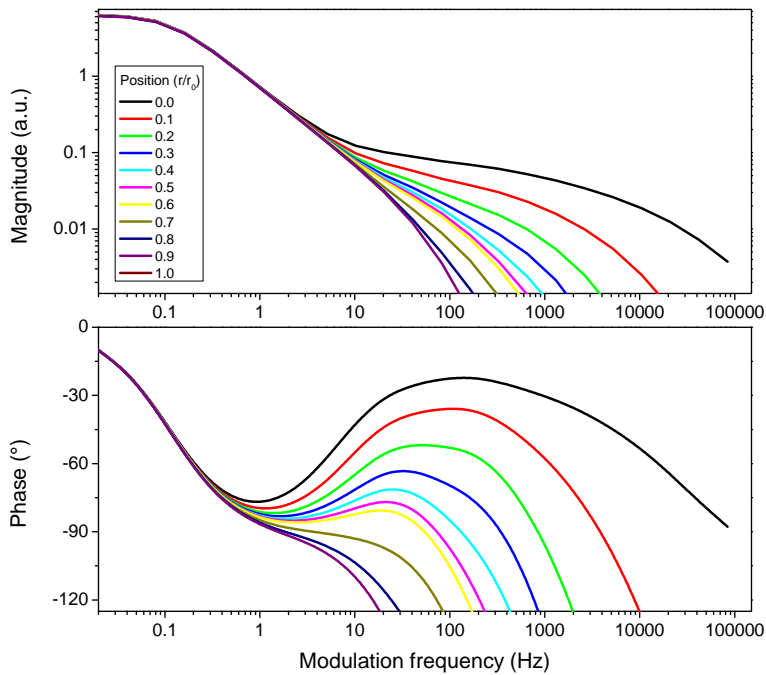


Figure 6.11: Magnitude and phase of the induced temperature modulation for different radial positions.

Naturally, the diffusion time can be changed by changing the fiber parameters and geometry. Since the transfer function severely depends on the radial position in the fiber (Fig. 6.11) and the relevant temperature for the optical properties is the core temperature, the temperature in the center was evaluated. The transfer function for different core sizes, which corresponds to different mode field diameters, is given in Fig. 6.12 (a). The behavior is almost the same as for different radial positions: the slope in the region from 2-1000 Hz increases with core size. In Fig. 6.12 (b) the thermal conductivity was varied. While there is no practical relevance to it, it is still very instructional to understand the difference, since it shows the frequency region dominated by conductivity through the fiber. It can be seen that the magnitude changes in this frequency region. In the limit of very high thermal conductivity the transfer function would become a simple low pass. Fig. 6.12 (c) shows the impact of the heat transfer coefficient. This property can be changed very easily by having the fiber cooled by air, on a spool, on a spool with thermal conductance paste, or

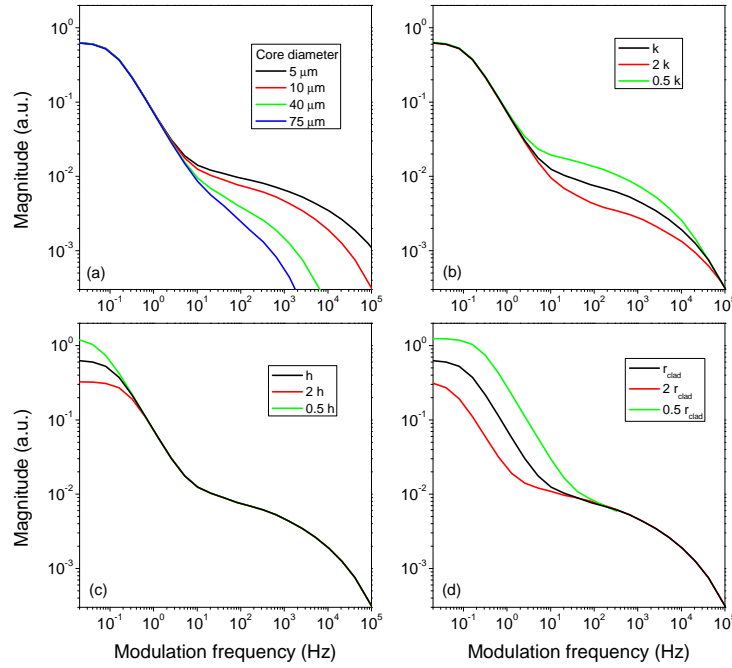


Figure 6.12: Dependence of the transfer function on fiber parameters (a) core size / mode field diameter (b) thermal conductivity k (c) heat transfer coefficient h (d) cladding radius.

by water cooling. It can be seen that this only influences the magnitude in the low frequency range. Lower heat transfer coefficients shift the corner frequency to lower frequencies. Instead of changing the heat transfer it is also possible to increase the fiber diameter (Fig. 6.12 (d)). This also changes the low frequency region, but the corner frequency shifts to higher frequencies for smaller fibers, because the heat capacity of large fibers is larger, and thus more time is needed to reach steady state.

Modal instabilities, which are currently the main limitation for power scaling of fiber amplifiers [40–42], are also caused by dynamic temperature induced refractive index changes. While this is not the main point of interest in this chapter, the dynamic radial heat flow described here has implications on this topic. There are currently two concepts to explain modal instabilities: the theoretical model by Smith et al. [43, 77] does not rely on the low frequency contribution and thus different cladding size or cooling should not matter. On the other hand experimental data

suggests otherwise [46], which makes a strong point for the model presented in the same article, which includes heat flow and correct boundary conditions. In this model, the mode fluctuations decrease above 1.5 kHz even for pump power way above the mode instability threshold – which is consistent with radial heat flow predicting a corner frequency between 1-2 kHz for fibers with 40-75 μm core diameter. It is worth noting that the rapid fall-off at high frequencies is also a limit for the maximum mode fluctuation frequencies. According to Fig. 6.12 (a) the fall-off depends on the core diameter, which explains why higher mode fluctuation frequencies are observed in fiber amplifiers with smaller cores [41].

6.2.2 Experimental Results

To validate the model experimentally, the relative phase of two ytterbium doped fiber amplifiers was measured as shown in Fig. 6.13. Then, the pump power of one amplifier was modulated. For the phase readout frequency sidebands at 12 MHz were used in a heterodyne scheme. To keep the interferometer at a fixed operating point, the interferometer was locked, either using a feedback loop to the pump diode or with a fiber stretcher.

When using a feedback loop to the pump diodes, the pump modulation was injected using an adder just before the pump diode driver and the gain between the injected voltage and the error signal was measured. When the fiber stretcher was used to stabilize the loop, the control signal of the fiber stretcher was monitored. The transfer function includes the low pass of the current driver, but this was accounted for in the calibration of the signal. One could argue that, if the heating was exclusively due to quantum defect, an additional low pass should be present because of the effective ion lifetime in the amplifier. However, the cutoff frequency would only occur at about 10 kHz as seen in chapter 3. So, it is not relevant for this measurement. At the same time it is also not quite clear, if only the quantum defect is a good approximation for this amplifier.

Depending on the amplifier parameters the majority of the phase shift is either caused by thermal effects or Kramers-Kronik-Relations (KKR). In these measurements the pump modulation caused sufficient thermal load, but did not change

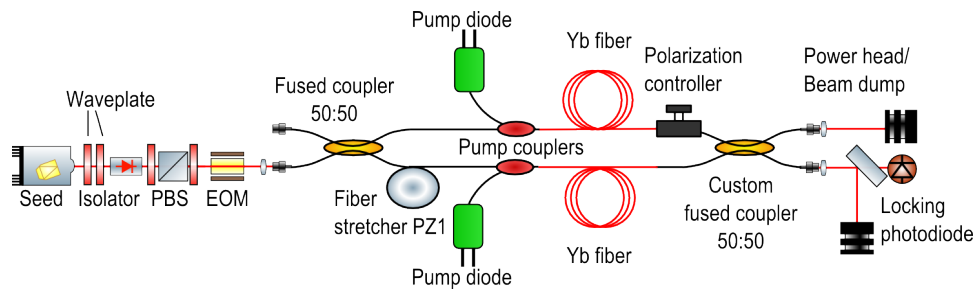


Figure 6.13: Interferometric setup for the optical phase measurement.

the gain strongly. This allowed the measurement of the phase shift induced by the temperature shift. Besides that if KKR were the dominant contribution to the phase shift, the magnitude would depend on the operating point of the amplifier. In this case the gain depends on the number of ions in the upper laser level. With more average pump power the population saturates and the same change of pump power will cause a smaller change in the occupation of the upper laser level. This causes the KKR contribution to become smaller at higher average pump power. On the other hand the thermally induced phase shift stays the same. The average temperature in the fiber increases, but this does not change the temperature modulation, at least when neglecting second order effects like the temperature dependence of thermal conductivity, density and heat transfer coefficient. In this experiment the measured transfer function was also widely independent of the pump power.

Compared to the theoretical predictions, the experimental data (Fig. 6.14) showed an additional dip at around 2 kHz, which could be caused by heat dissipated in the cladding, since the simulation does not account for this. The heat transfer coefficient assumed for the simulation ($h = 65 \text{ W}/(\text{m}^2\text{K})$) was apparently slightly too low, which caused the mismatch at low frequencies. Besides that, the behavior of the measured optical phase shift was nicely reproduced by the simulation of the simulated $10 \mu\text{m}$ core double clad fiber, for which the only fit parameter was a constant factor for the temperature to phase shift conversion. Especially the slope in the frequency region from 3 - 1000 Hz, which is characteristic for this core diameter, was well reproduced.

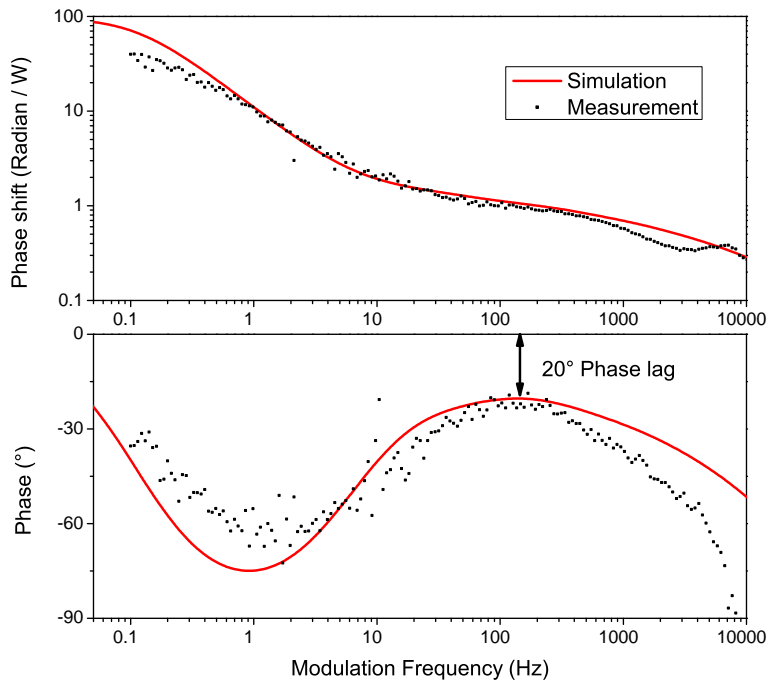


Figure 6.14: Comparison of simulated temperature transfer function and measured optical phase shift.

6.3 Summary

The temporal dynamics of refractive index changes in fiber amplifiers and the corresponding phase shift of the signal wave were analyzed in this chapter. Two major coupling mechanisms were identified: fiber amplifier gain, which couples to the signal phase via KKR and thermal effects. The model for the coupling of pump and seed power modulation to output power derived in chapter 3 can also be applied for the KKR effect and describes all the important features.

Thermal effects can be even more important. In the low frequency range the complete fiber heats up and cools down. If the gain change is low and the heat load high enough, even the higher frequency region can be dominated by heat, which was discussed in the second part of the chapter. It was shown that besides the comparatively slow heat up of the complete fiber the heat diffusion through the fiber must be considered as well. This results in significant contributions in the frequency

region at about 2-1000 Hz. Depending on the fiber geometry and cooling specific characteristics of the transfer function change.

These insights on temporal dynamics of the phase shift will help with the design of phase control systems as well as the description of any effect which depends on the temperature induced dynamic refractive index change.

7 Collinear Coherent Combining of Two 10 W Fiber Amplifiers

One possibility to avoid the difficulties arising in very high power single frequency amplifiers is the use of two or more amplifiers and to coherently combine their output beams. In recent years, many improvements were reported in this field [50, 78–80]. Contrary to SBS suppression, the narrow linewidth required for gravitational wave detectors is also an advantage for coherent beam combining. For use in gravitational wave detectors the resulting beam has to be close to the diffraction limit, because only the power in the fundamental Gaussian mode can be used in the resonant cavities utilized by the interferometer. Therefore, the combined beams must overlap in both near and far field. Thus, a tiled aperture approach is not an option. Instead, the beams have to be overlapped collinearly in both the near and far field.

Previously, two collinearly combined injection locked Nd:YAG oscillators with an output power of 3 W each were investigated in terms of power and phase noise by Musha et al. [81] and three Raman amplifiers were collinearly combined for use in a frequency doubling cavity by Taylor et al. [82]. Uberna et al. proposed the use of polarizers [54] for collinear coherent combining. For this thesis collinear combining in a Mach-Zehnder configuration using two 10 W ytterbium doped fiber amplifiers seeded by a single-frequency Nd:YAG nonplanar ring oscillator (NPRO) was investigated. At this power level significant thermal effects can already be expected, but at the same time single mode fibers can still be used, which avoids issues like imperfect beam quality and pointing of the individual amplifiers.

The experiments described here emphasize on power and frequency noise and the achievable beam quality, since these are the main concerns when using coherent

beam combining in a laser system for gravitational wave detectors.

7.1 Setup

An NPRO with an output power of 600 mW was used as a seed laser. The seed power was divided using a 50:50 beam splitter as depicted in Fig. 7.1. Each of the separated beams was amplified in a 4 m long double clad polarization maintaining ytterbium doped fiber (Nufern PLMA-YDF-10/125). Both amplifiers were co-pumped by a fiber coupled 25 W, 976 nm pump diode. Each amplifier achieved an output power of 11.4 W and a polarization extinction ratio (PER) of 16-18 dB. To combine the two beams with the best possible beam quality and combining efficiency, a free space 50:50 beam splitter was used. Therefore, the beam combination was realized in a Mach-Zehnder configuration with one amplifier in each arm. Assuming that the majority of the effects will be similar for high power amplifiers the setup should be a realistic prototype to demonstrate the concept and to learn about associated challenges. To stabilize the relative phase between both interferometer arms, a standard heterodyne technique was used. An electro optic phase modulator (EOM) in one interferometer arm induced 12 MHz phase modulation sidebands. These sidebands were used as phase references in a heterodyne readout scheme to measure the relative phase between the two interfering light fields on the combining beam splitter. A mirror mounted on a piezo electric transducer ($\sim 50 \mu\text{m}$ stroke) was placed in the other arm to stabilize this phase and to achieve stable interference of the two amplified beams. In the interferometer control loop the unity gain frequency

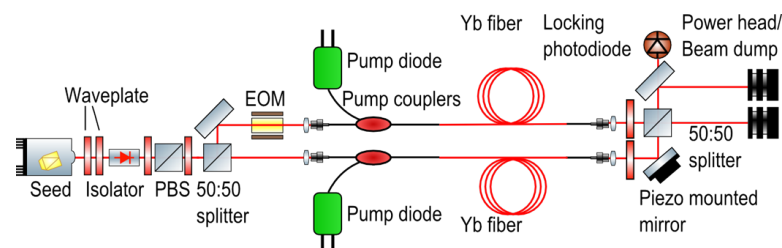


Figure 7.1: Schematical overview of the beam combining setup. PBS: Polarizing beam splitter, EOM: electro optical modulator.

was at 7 kHz.

After measuring the output power of each amplifier (Fig. 7.2, triangles), the two beams were combined with a combining efficiency of 95-97% over the whole amplifier slope (Fig. 7.2, squares). During the measurement the pump power of one amplifier was fine-tuned to maximize the combining efficiency. At a pump power of 16 W per amplifier, the combined signal power was 21.8 W. Only 0.88 W left through the dark port of the interferometer. The system was stable under laboratory conditions and the duration of continuous operation was limited by actuator range. After a warm-up time of a few minutes the system stayed at its operation point for more than half an hour. It was possible to cause a relock with intentional flicks to the fiber or a knock on the optical table. Even though the long term performance was sufficient for the characterization, the employment of an actuator with larger dynamic range for the interferometer control could increase the continuous operation time significantly.

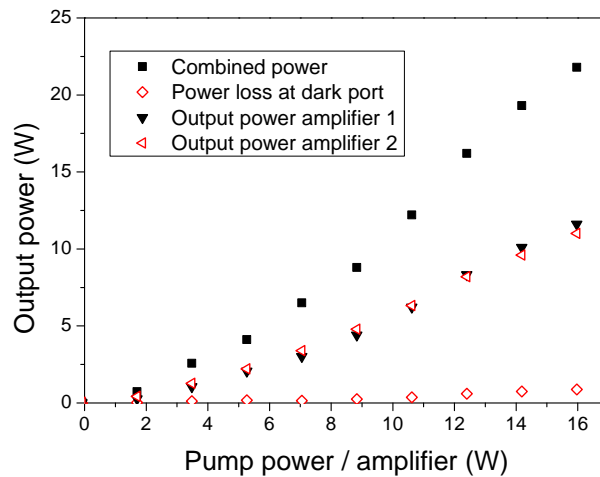


Figure 7.2: Power of the amplifiers and the coherently combined output power of the system. When the slope of the combined beam was measured, the pump power of the second amplifier was fine tuned to optimize the combining efficiency.

7.2 Beam Quality

To evaluate the beam quality, a non-confocal three mirror ring cavity with non-degenerate TEM_{nm} eigenmodes (mode-cleaner cavity) [83] was used in a setup as depicted in Fig. 7.3. By scanning the cavity length over one free spectral range, the power in the different spatial modes can be separated and the power fraction in the fundamental Gaussian mode can be obtained. First, both amplifiers were individually mode matched to the cavity. This procedure also ensures a good spatial overlap between the two beams at the combination beam splitter and therefore supports a good combining efficiency. Then, the length of the resonator was scanned and the power at the reflecting port was measured with a photodiode. From the ratio of the reflected power, when the cavity was resonant for TEM_{00} and the power reflected by the non-resonant cavity, the power fraction in TEM_{00} can be obtained. In this case the TEM_{00} fraction was 97% for the single amplifiers as well as for the coherently combined beam. Since neither the single amplifiers nor the combined beam was in a pure linear polarization state (16-18 dB PER) and since the modecleaner cavity's resonance condition is polarization dependent, the remaining 3% were most likely dominated by TEM_{00} light in the second polarization state. Furthermore, the 12 MHz sidebands already present in the combined beam were used to lock the cavity to the fundamental mode using the Pound-Drever-Hall technique [7, 8]. In this way a linearly polarized, pure Gaussian beam with an output power

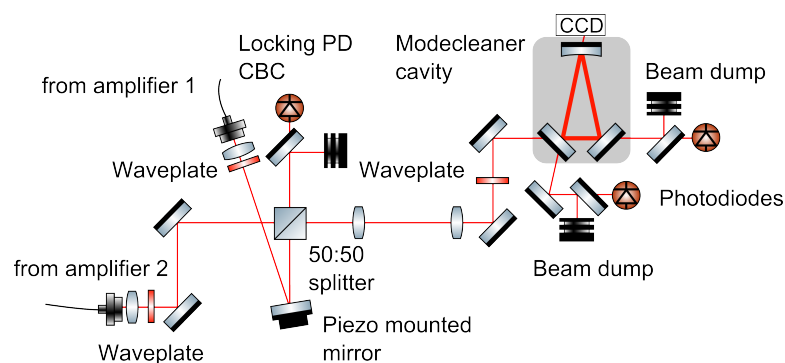


Figure 7.3: Combining part of the setup, including the mode cleaner cavity for the beam quality measurement.

of 21.3 W was obtained in transmission of the cavity and 0.72 W was reflected, consisting of TEM₀₀ light in the second polarization state and higher order modes. This value is consistent with the 97% obtained from scanning the cavity. These results show that a well aligned collinear beam combination does not degrade the beam quality.

7.3 Power and Frequency Noise

To measure the power noise, the beam transmitted by a mirror between the combining beam splitter and the mode cleaner cavity was used. Since the relevant properties are noise properties of a linearly polarized output beam, a polarizing beam splitter cube was added in front of the highly reflective mirror (not shown in Fig. 7.3). Then, the noise spectra of the single amplifiers as well as of the combined beam were measured with a low noise photodetector. In Fig. 7.4 the relative power noise (RPN) of the NPRO (blue), a single amplifier (red), and the combined beam (black) are shown. In the frequency range from 1-1000 Hz the RPN of the single amplifier was significantly

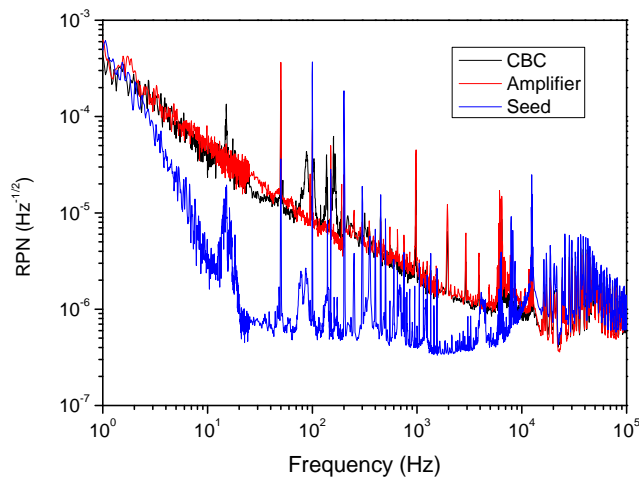


Figure 7.4: Relative power noise of combined beam, single amplifier and NPRO seed laser. For the largest part of the spectrum the RPN is dominated by the single amplifiers.

increased compared to the seed. The reason for this is most probably coupling of pump light power noise into the amplifiers output. Since different pump diodes have different levels of RPN, the amplifiers had different RPN as well. The amplifier shown in Fig. 7.4 is the one with the larger RPN. For frequencies above 10 kHz the amplifier's RPN was dominated by the seed noise. As shown in Fig. 7.4, the RPN of the combined beam was very close to the RPN of a single amplifier. For frequencies larger than 10 kHz the power noise was dominated by the seed source, such that it should be possible to reduce the RPN of the combined beam in this frequency range to a level below $10^{-6}\text{Hz}^{-1/2}$ with a more stable seed source. The combined beam's power noise spectrum reveals an additional peak at approximately 15 Hz and some excess noise in the region of 100 Hz. The RPN in the frequency range dominated by pump noise is not decreased by a factor of $\sqrt{2}$ as demonstrated with the core pumped system in chapter 5. However, even when incoherently overlapping multimode pump diodes with a fiber bundle, such a decrease is not reliably obtained [63]. Besides, except for these few distinct peaks, there was no power noise added by the beam combining, which is a quite promising result.

To measure the frequency noise, the mode cleaner cavity was stabilized to the fundamental mode as described in section 7.2 and the calibrated piezo control signal together with the calibrated Pound-Drever-Hall error signal was used. From an earlier measurement [84] it is known that the length noise of the cavity causes equivalent frequency noise smaller than the level measured here. As one can see in Fig. 7.5, the frequency noise was almost identical for both, the combined beam and the single amplifier. The measured $1/f$ slope is characteristic for the seed source [85]. The 15 Hz bump was probably caused by the seed laser, because it is visible in the RPN of the NPRO as well.

For a better understanding of the dynamics and the origin of the small additional noise features in the combined beam, actuator- and error signal of the interferometer control loop were monitored. From these signals, the free running differential phase noise (black curve in Fig. 7.6) and the in-loop stabilized phase noise (Fig. 7.6, blue curve) were derived. Since the arm lengths were only balanced to a length difference of about 1 m, frequency noise of the seed laser coupled into differential phase noise.

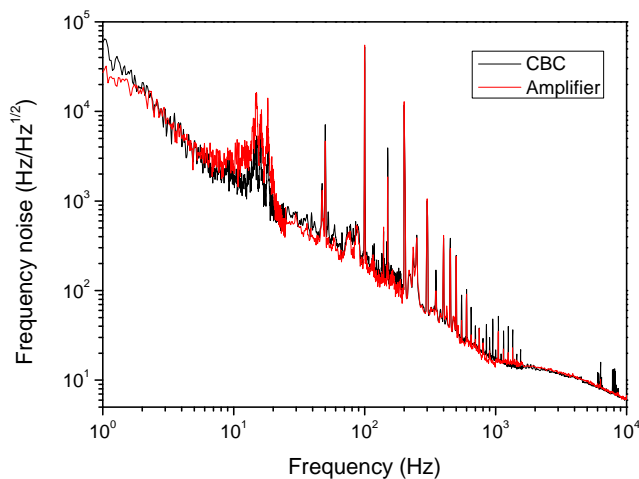


Figure 7.5: Frequency noise of single amplifier and combined beam.

The magnitude of this effect was calculated by projecting the single amplifiers frequency noise to the interferometer's phase noise and is shown in Fig. 7.6 (red curve). It can be seen that the phase noise measurement was not influenced by the frequency noise of the seed laser. The additional peaks in the power noise spectrum were also present in the differential phase noise of the interferometer. They could be caused by mechanical or electrical disturbances of the interferometer.

Neglecting the distinct peaks in the spectrum, the free-running phase noise power spectral density can be approximated as $S_\varphi = 10^{-1} \text{rad} \sqrt{\text{Hz}}/f$. In a phase locked system with a control loop gain $\propto 1/f$ this noise becomes approximately constant for frequencies lower than unity gain frequency. The phase variance $\langle \varphi^2 \rangle$ in dependence of the unity gain frequency f_u can then be obtained by integration of S_φ^2 from unity gain frequency to infinity and adding the integrated constant noise below unity gain. This results in $\langle \varphi^2 \rangle = 2 \cdot 10^{-2} \text{rad}^2 \text{Hz}/f_u$. With this, the contribution of the phase variance to the combining loss can be estimated by means of equation (2.3). For example, to keep this contribution below 1%, a phase variance $\langle \varphi^2 \rangle \leq 4 \cdot 10^{-2} \text{rad}^2$ is needed, i.e. a unity gain frequency above 0.5 Hz would be sufficient.

For a projection of phase noise to power noise the square of the phase noise

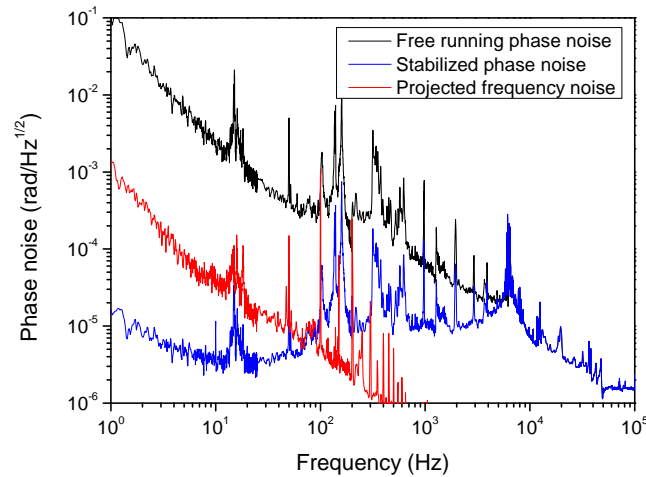


Figure 7.6: Differential phase noise of the two amplifiers (free running, stabilized and the projection of frequency noise of the seed laser). The peak at 15 Hz and the ones around 100 Hz, which can be seen in the RPN of the combined beams, are also present here.

in the time domain and thus a convolution in the frequency domain would be required. However, the self convolution of S_φ cannot be obtained without the phase information. As a rough estimation the 15 Hz peak should be included within the control bandwidth for increased system stability. A unity gain frequency of 100 Hz will still be sufficient for this. Thus, even a very simple interferometer control loop can fulfill these moderate requirements.

7.4 Summary

In this chapter collinear coherent beam combining at 1064 nm using two ytterbium doped fiber amplifiers was discussed. The achieved combining efficiency was larger than 95% and the combined power was 21.8 W. The setup was stable under laboratory conditions and the long term performance was limited by the available range of the length control actuator of the interferometer. 97% of the output power was emitted into the fundamental Gaussian mode. Apart from some small additional peaks, the

RPN was dominated by the single amplifiers. In terms of frequency noise there was almost no difference between a single amplifier and the combined beam.

When combining high power fiber amplifiers, potentially more thermally and gain induced phase noise will have to be compensated. However, it has already been shown that differential phase stabilization is possible even at the kW power level [29]. Since the fibers used in high power amplifiers are not strictly single mode, combining efficiency and fundamental mode content will likely degrade compared to the single mode fibers used in these experiments. The influence of beam pointing might also be more significant in high power amplifiers, which could degrade the combining efficiency and therefore contribute to the power noise. Overall, coherent beam combining is probably the most promising approach to realize the laser sources to be used in 3rd generation gravitational wave detectors, since additional technical noise sources are not an issue.

8 All-Fiber Coherent Beam Combining

The most obvious step towards a more simple setup for coherent beam combining is moving to an all fiber configuration. This eliminates the need for mode matching of the output beams to each other and potentially reduces the sensitivity to environmental noise. Naturally, this introduces new challenges as well, because the power handling capabilities of fiber components are often not as good as those of their free space counterparts. For example piezo mounted mirrors can be replaced with piezo driven fiber stretchers, but these usually require comparatively large fiber lengths, which can cause problems due to nonlinear effects. Alternatively, ytterbium doped fiber amplifiers have been used as phase actuators at the erbium wavelength [66]. This is a very elegant solution, because it does not rely on any moving parts and does not require any high voltage sources. It is also capable of handling higher power, because it is a true all fiber method with low loss.

All fiber CBC and novel phase actuation methods are evaluated in this chapter, starting with an erbium fiber amplifier as a phase actuator for low power CBC at 1064 nm and continuing with an all fiber version of the 20 W system from chapter 7. This system was phase stabilized using fiber stretchers and alternatively even without a dedicated phase actuator at all. In this case pump power modulation of the ytterbium amplifiers was used instead. These methods are also an impressive showcase of the potential of the phase shift dynamics discussed in chapter 6. It also shows that even a comparatively slow temperature induced phase drift can be helpful for phase control using fiber amplifiers, because it increases the actuator range.

8.1 Erbium Doped Fiber Amplifier as a Phase Actuator at 1064 nm

To demonstrate all fiber beam combining and the suitability of an erbium doped fiber amplifier as a phase actuator at 1064 nm, two ytterbium doped fiber amplifiers pumped at 975 nm were combined in a Mach-Zehnder configuration and the interferometer was stabilized with an erbium doped fiber amplifier (Fig. 8.1). Because of the large temperature induced phase shift, modulation of the 1480 nm pump diode was chosen to stabilize the interferometer (400 mW average pump power, ~ 3 mW average seed power). No additional measures were taken to increase thermal isolation or conductivity of any fibers. The interferometer was locked using a standard off-the-shelf locking electronics (Toptica DigiLock 110) with a PID servo and a Lock-In detector module. To generate a heterodyne error signal, the $1.55 \mu\text{m}$ seed power was modulated at 48 kHz, resulting in a corresponding modulation of the optical phase at 1064 nm. All laser diodes were modulated using the modulation port of the laser diode driver (Thorlabs LDC 8040, 50 kHz bandwidth).

The output power of a single ytterbium amplifier was 238 mW. When combined, an output power of 451 mW and 7 mW at the dark port was achieved. Therefore, the overall losses were about 5%. The symmetric losses could be caused by the 50% coupler at the output and the additional splices. Typical coupler losses are around 2-3%. When neglecting this symmetric loss, the combining efficiency was better than 98%. The remaining 2% consist of ASE, which cannot be combined, polarization mismatch, uneven separation of the couplers and the control sidebands to generate

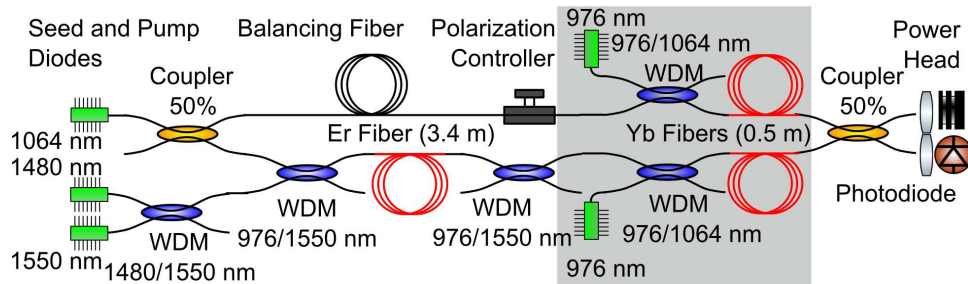


Figure 8.1: Fiber based Mach-Zehnder interferometer used in the experiment.

the error signal.

This setup stayed in lock for longer than 4 hours (Fig. 8.2). A relock was forced when the control signal was close to maximum range to reset the actuator to its center position. On short time scales (Fig. 8.3, frequency range 10 Hz – 250 kHz, given by AC coupling and the sampling rate of 500 kHz of the oscilloscope used), the relative peak-to-peak power noise was less than 2% and the relative RMS noise was 0.1%. Assuming all power noise was caused by phase noise, the RMS phase error was about 0.04 radian. Without active stabilization the output power fluctuated strongly (Fig. 8.4).

Besides phase noise generated in the amplification process and mechanical fluctuations of the setup one major noise source was frequency noise of the 1064 nm seed diode. This frequency noise was then converted to intensity noise in the interferometer due to the unequal arm lengths ($\Delta L \approx 2$ cm). It should be possible to reduce this noise contribution with more symmetric arms or by using a seed source with intrinsically less frequency noise.

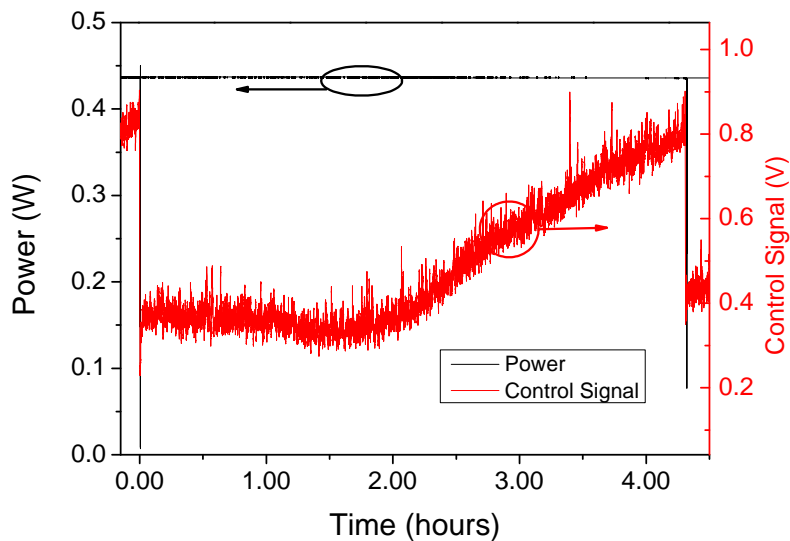


Figure 8.2: Long term stability of the lock. Output power of the locked interferometer and the corresponding control signal.

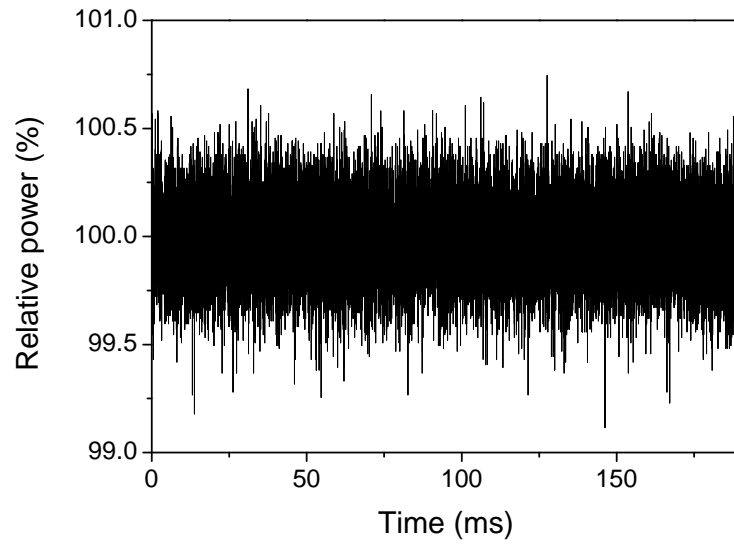


Figure 8.3: Short term noise in time domain.

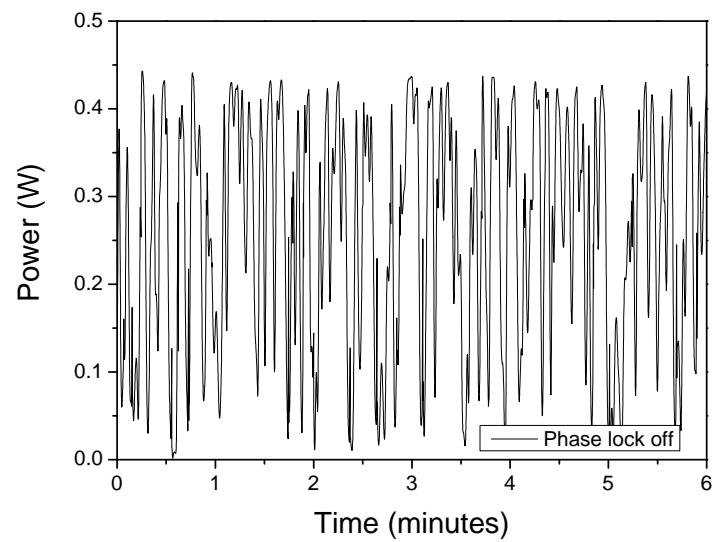


Figure 8.4: Unstabilized output.

Overall, it was successfully demonstrated that KKR and thermal effects in an erbium doped fiber amplifier can be used effectively to realize all-fiber CBC of two ytterbium amplifiers. The suitability of an erbium doped fiber amplifier as a phase actuator at 1064 nm has never been demonstrated before, making this system the first proof of concept. However, for a detailed analysis of power and phase noise the CBC system presented in chapter 7 was used, as it is a much more realistic prototype. As both systems cannot be compared directly because of the different power levels, a more detailed analysis of this proof of concept system was not useful.

8.2 All-Fiber CBC at Medium Power

In the free space system used to evaluate prospects and challenges of CBC in laser systems for GWD (chapter 7) relocks were usually caused by limited actuator range ($\sim 50\mu\text{m}$). Thus, one obvious improvement to this system would be to include an actuator with larger dynamic range. This was realized in an all-fiber configuration using fiber stretchers, which can easily deliver optical path length differences on the mm scale.

Overall, the system was quite similar to the one presented in chapter 7. The amplifiers were seeded by an NPRO with an output power of 600 mW. The seed beam was coupled into a fiber and the power was divided using a commercial 50:50 polarization maintaining (PM) fused coupler (Fig. 8.5). The separated beams were amplified in two 4 m long double clad ytterbium doped fibers (Nufern PLMA-YDF-10/125). Both amplifiers were co-pumped by a fiber coupled 25 W, 976 nm pump diode, each. For an all fiber setup a fiber based actuator and a combining element is needed. For good beam quality a filled aperture combining element has to be used [53, 54]. To keep even this step fiber based, a fused coupler was chosen as the combining element. To avoid stimulated Brillouin scattering in the coupler and the associated fiber, a custom single mode non-PM fused coupler with a 10 μm core diameter was developed, which can tolerate more than 25 W of output power [86]. It was the only non-PM component in the setup.

Two different piezo driven fiber stretchers were used (Optiphase, types PZ1 and

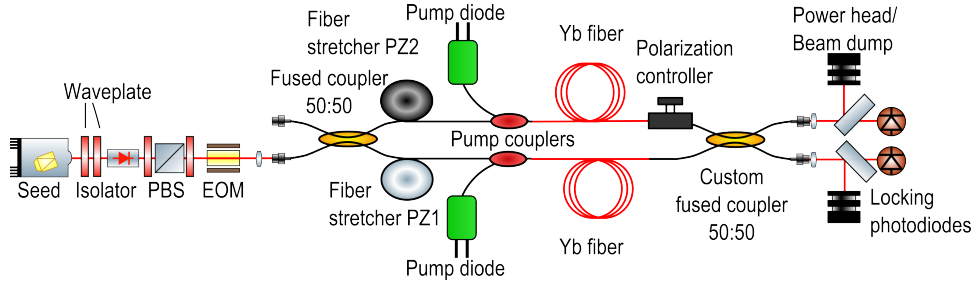


Figure 8.5: Setup used for the all-fiber coherent beam combining of two 10 W signals.

PZ2) to realize a large actuator range in an all fiber configuration. The error signal for the interferometer length control was generated with a heterodyne readout scheme. For this, an electro optic modulator (EOM) added 12 MHz frequency sidebands to the seed beam, before it entered the CBC setup. Because of the arm length difference in the interferometer (~ 30 m), these sidebands could be used as a phase reference for the heterodyne readout scheme to measure the relative phase of the two interfering fields in the coupler. This signal was used with a PID servo to control the fiber stretcher PZ1 ($\sim 40 \mu\text{m}$ dynamic range). The second fiber stretcher (~ 1 mm dynamic range) was used in a slow second control loop to keep the faster PZ1 stretcher at the center of its range.

With this scheme an output power of up to 25 W at the bright and only 0.38 W at the dark port was achieved (Fig. 8.6). Over the whole amplifier slope the power loss at the dark port was less than 2%.

However, the first iteration of this system showed some excess noise compared with the original free space design (Fig. 8.7 (a)). Even careful tuning of the PZ1 and PZ2 control loops did not yield the desired results (red curve). The additional peak visible in the RPN at about 18 kHz corresponds to the first mechanical resonance of the PZ2 stretcher. Although a dedicated low pass (1.5 kHz) was already included in the high voltage circuit driving the PZ2 stretcher, the large phase shift ($> 5 \mu\text{m} / \text{V}$) still allowed excessive current noise coupling to the optical phase. A change to a low pass with a corner frequency of about 20 Hz brought the desired result (Fig. 8.7 (b), black curve) and did not hinder performance, because high frequency

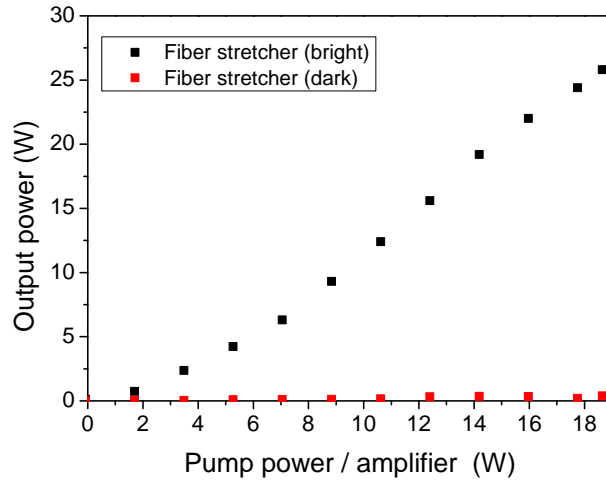


Figure 8.6: Output power of dark and bright port vs. input pump power per fiber amplifier.

fluctuations were compensated by the PZ1 stretcher anyway. For comparison the RPN of a single amplifier (Fig. 8.7 (b), blue curve) and the RPN of the free space system covered in chapter 7 (red curve) are shown in Fig. 8.7 as well. The RPN of the optimized system was dominated by the single amplifier, again. The additional peaks around 100 Hz visible in the free space system’s RPN were not present in the RPN of the all fiber CBC setup.

The long term stability of the system was also measured. It was possible to lock the system, then turn up the pump power of both fiber amplifiers and operate it for 12 hours without any relocks (Fig. 8.8). Polarization mismatch of the two amplified beams due to the non-PM combiner caused the fluctuations during the first hours. It should therefore be possible to avoid these fluctuations when using only PM components with highest possible polarization extinction ratios. After the initial fluctuations the system’s output power was within $\pm 2\%$ of its average output power for more than 6 hours even without this optimization.

It should be possible to stabilize this system using an erbium fiber amplifier as well. However, one major downside is that the actuator range depends on heat load and a medium power erbium fiber amplifier would be required to combine two

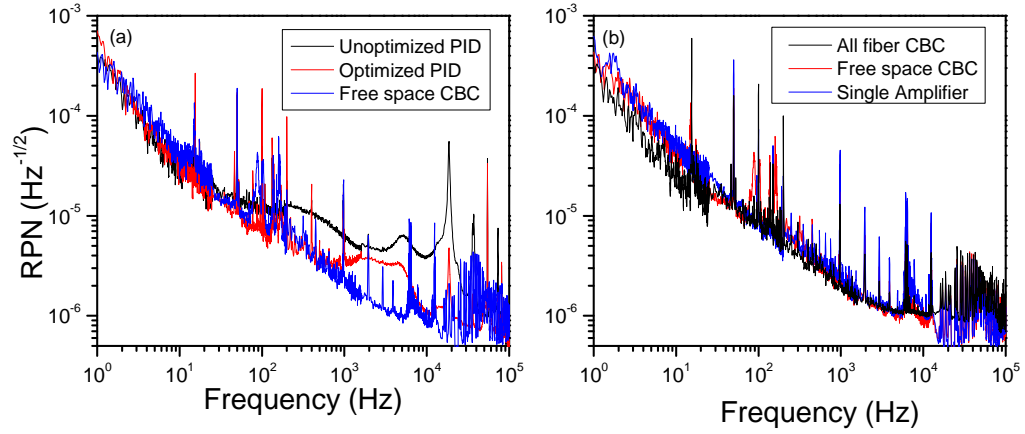


Figure 8.7: (a) RPN of the unoptimized fiber stretcher system compared with the free space CBC system (b) RPN of a single amplifier, free space and optimized all fiber CBC.

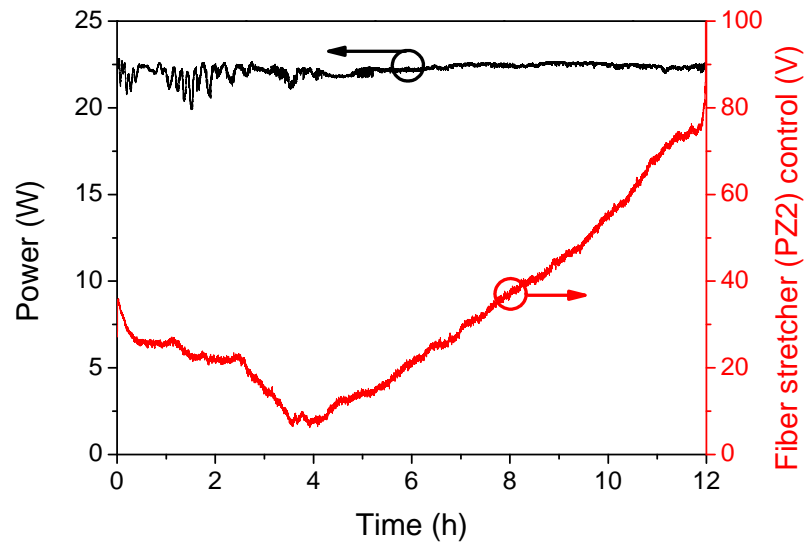


Figure 8.8: Longterm measurement with the fiber stretcher.

medium power ytterbium amplifiers, which would make the overall system neither simple nor cost effective. However, when operating at medium or higher average power using the ytterbium amplifiers to also induce the phase shift [87] and thus eliminating the need for a dedicated phase actuator altogether, becomes a viable option.

The penalty for this approach is the conversion of phase drifts to power noise. Assuming perfectly matching phases in the combining element, coherent addition of two fields with a small amplitude modulation ($A_1 + \Delta A_1$ and $A_2 + \Delta A_2$) yields the output power at the bright/dark port

$$P = \frac{1}{2} \left((A_1 + \Delta A_1) \pm (A_2 + \Delta A_2) \right)^2. \quad (8.1)$$

If both mean fields are the same ($A_1 = A_2 = A = \sqrt{P}$) and only amplifier 1 is modulated to compensate the phase drift ($\Delta A_1 = \Delta A$, $\Delta A_2 = 0$), the total power is $P_{\text{bright}} \approx 2A^2 + 2A\Delta A = 2P + \Delta P$. If instead of using one amplifier both amplifiers are controlled differentially ($\Delta A_1 = -\Delta A_2 = \Delta A$), there is no coupling to the bright port at all ($P_{\text{bright}} = 2A^2$) and power modulation is only present at the dark port ($P_{\text{dark}} = 2\Delta A^2$). Unfortunately, a linear controller will usually control the power and not the field, which adds a second order combining loss term to the bright port. However, differential pump power control is still a significant improvement over the linear coupling in the single amplifier case. Assuming the induced phase shift to be linear with the output power ($\Delta P \propto \Delta \phi$) and the majority of the phase noise to be caused by environmental effects, the relative power noise induced by phase stabilization decreases with average power, for both methods.

The differential control signal was generated with a combination of an analog adder and a subtractor (Fig. 8.9 (a)) and the result was fed back to the pump diodes. When inverting the sign of the control signal for one pump diode, the phase can be controlled (asymmetric path). The power can be stabilized simultaneously by feeding the same signal to both pump diodes (symmetric path). This concept can be scaled either by stacking up 2^n amplifiers, but also with a 1xN-combiner and summation over all control signals for a first order feed forward power correction as

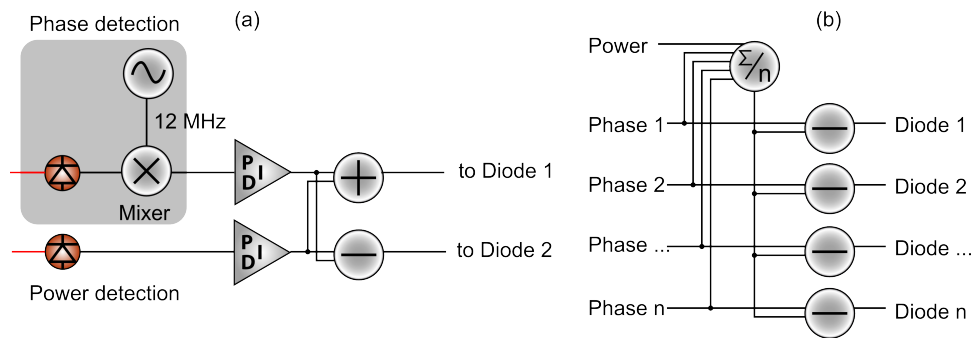


Figure 8.9: Stabilization via pump power modulation: (a) control path implementation in our setup, (b) possible extension to n amplifiers.

shown in Fig. 8.9 (b). One could argue that this feed forward control is not necessary when stabilizing the power anyway, but the reduced cross coupling between phase and power stabilization will be beneficial when optimizing the feedback loops. Due to the current supply used, the unity gain frequency was limited to 1 kHz. This was lower than the bandwidth of the fiber stretcher control loop (≈ 9 kHz), but it should be possible to reach a comparable control bandwidth with more optimized electronics.

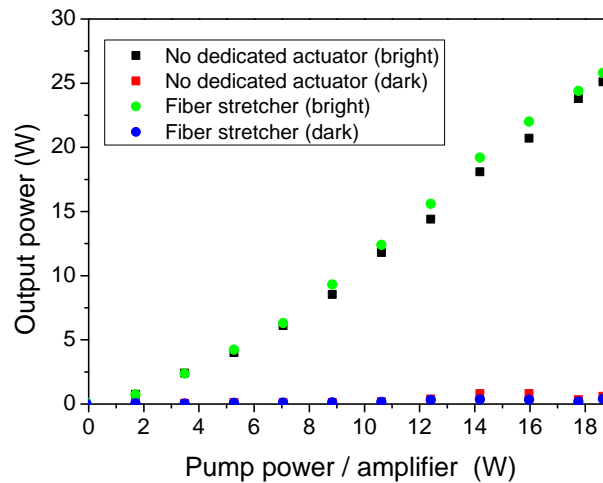


Figure 8.10: Output power of bright and dark port in dependence of launched average pump power per amplifier.

Even with this stabilization scheme 25 W at the bright and less than 0.6 W at the dark port were achieved (Fig. 8.10)). Over the whole amplifier slope the power loss at the dark port was less than 5%. Naturally, the pump power had to be set before enabling the phase stabilization in this setup. Furthermore, one has to note that the combining efficiency eventually becomes worse when using the amplifiers to stabilize the phase, since the average power imbalance increases with time. However, the bright port usually stayed within 5% of the operating power even when locking for half an hour or more and the combining efficiency can easily be reset to the optimum value by allowing for a short relock. Nevertheless, for long term operation without any relocks an additional actuator would be recommended. Even a simple thermal phase actuator such as a Peltier element should be sufficient.

In Fig. 8.11, the relative power noise (RPN) of the system using fiber stretchers (red) and pump power modulation (black) is shown. In the frequency range from 1-10 kHz the performance of the fiber stretcher based control loop is about a factor of two better. When stabilizing the phase using the ytterbium amplifiers, the unity gain frequency was 1 kHz, so this region is not in the control loop bandwidth. Overall, the noise is mostly limited by the single amplifier noise, which was also the case in

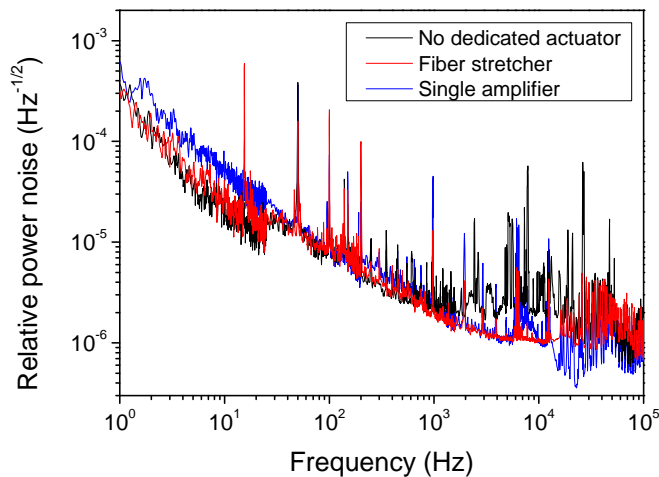


Figure 8.11: Relative power noise in the frequency range from 1 Hz to 100 kHz.

the free space system (Chapter 7). This is quite surprising considering the pump stabilization scheme converts phase noise to power noise. Yet, the low fractional pump power modulation required to compensate the phase drifts and the differential pump power stabilization scheme prevent the power noise from increasing above the level of a single amplifier.

Because the power noise was dominated by the single amplifier, the conversion of phase noise to power noise was compared for direct pump modulation of one amplifier and differential pump power modulation by injection of a frequency dependent phase modulation into the setup. Since there is no first order coupling in the differential stabilization scheme, there should be a large difference in phase noise to power noise coupling between the two locking schemes. An artificial phase modulation was induced using the PZ1 fiber stretcher and the resulting modulation of the output power was monitored. A frequency dependent plot of the induced relative power modulation divided by the driving phase modulation is shown in Fig. 8.12. Since the unity gain frequency was 1 kHz in the control loop, the performance was similar above this frequency. For lower frequencies, the difference quickly became more than one order of magnitude, demonstrating the improvement due to the differential pump power control.

This linear measurement is useful for the characterization of the differential pump power control, in spite of the fact that only a second order contribution can be expected. When neglecting phase noise only the second harmonic of the modulation frequency would be expected in the output power noise. But the induced phase modulation is small compared to the real phase noise at very low frequencies. Therefore, the phase noise cannot be neglected. Since a multiplication in the time domain is a convolution in the frequency domain, the largest output power modulation can be expected at the modulation frequency due to the mixing terms with the phase noise around 0 Hz. This is illustrated in Fig. 8.13. Fig. 8.13 (a) shows the expected characteristics of the relative phase noise in such system, which were estimated as a low pass $S = 1/\sqrt{f^2 + f_0^2}$ and the induced modulation at ω_{mod} . In case of a first order contribution, this can simply be projected to power noise. Fig. 8.13 (b) shows the self convolution of the phase noise, which corresponds

to the induced power noise in case of second order coupling¹. It can be seen that the main contribution is still at ω_{mod} . The peak is slightly broadened due to the convolution with the low frequency phase noise. The second harmonic is also visible but much less distinct.

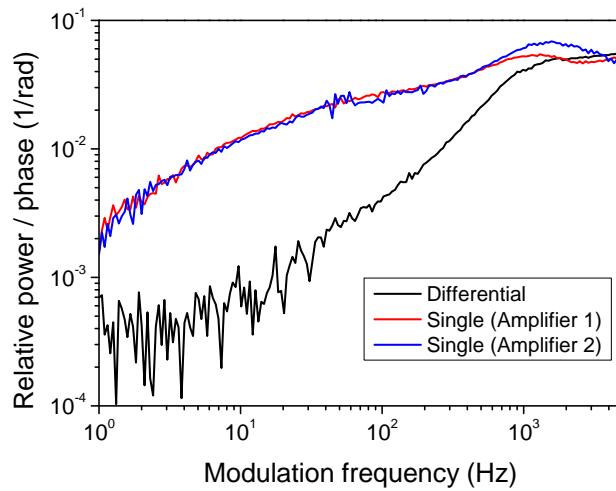


Figure 8.12: Noise coupling from phase to power noise with the differential and single amplifier stabilization.

¹ For quantitative calculations f_0 and the phase of the phase noise spectrum are required in addition to the magnitude.

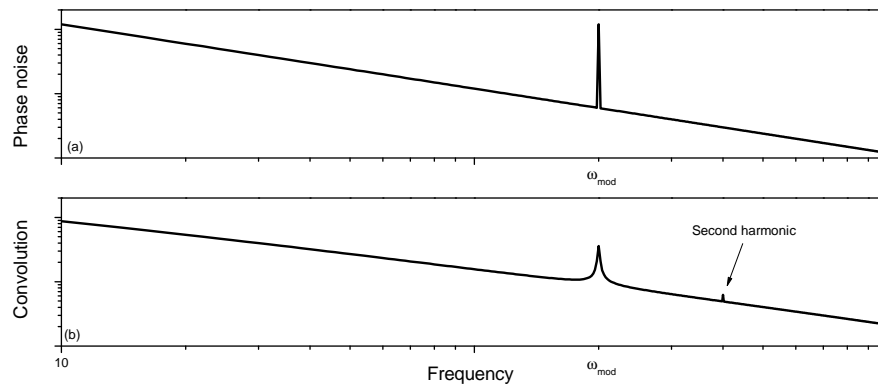


Figure 8.13: (a) Phase noise in the CBC system when adding a phase modulation, (b) self convolution of (a).

8.3 Summary

In this chapter all fiber coherent beam combining at 1064 nm at two different power levels was demonstrated. A low power scheme was used to demonstrate the utility of the KKR and thermal effects in an erbium fiber amplifier for coherent beam combining at 1064 nm. In a medium power system (25 W) the use of fiber stretchers for long term stable CBC was demonstrated. Furthermore, it was shown that the pump power induced thermal refractive index change can be used to effectively stabilize the relative phase of two fiber amplifier channels. Using differential pump power control, the coupling of phase noise to power noise can be minimized until there is no significant power noise increase noticeable in the region from 1 - 100 kHz. This is quite remarkable considering that this stabilization scheme converts phase noise to power noise by design.

9 Conclusion

The main goal of this thesis was the characterization and comprehension of the fiber amplifier gain dynamics and their impact on the signal output power and phase. For this, multiple fiber amplifier systems were characterized and suitable models were established to explain the observed effects. Furthermore, the prospects of power scaling via coherent beam combining in laser systems for GWDs were examined. It was shown that beam quality, power noise, and frequency noise can be preserved in CBC systems.

The impact of pump and seed power modulation on the output power was investigated first. The low pass observed in case of pump modulation as well as the damped high pass observed in case of seed modulation could be modeled with laser rate equations and even be derived analytically. For most single frequency amplifiers additional approximations enable the estimation of the dynamic behavior directly from the output and input power levels. The limitations, in particular low seed power compared to the saturation power, were discussed as well, but should rarely affect the modeling of high power single frequency amplifiers. It was shown that these methods can be applied to calculate the RPN of fiber amplifiers, if the power noise of the seed and the pump source is known. However, for a more accurate description of high power amplifiers additional effects like incoupling noise and pump spectral noise have to be considered as well.

In the next part the impact of pump and seed power fluctuations on the optical phase was analyzed. Here, two coupling mechanisms were observed. First, there is the gain which also changes the signal phase via Kramers-Kronig-Relations. This KKR phase shift was successfully modeled with the dynamic amplifier model developed for power modulation. Secondly, there is the heat generated by the amplification process, which changes the fiber temperature. Since the refractive index depends

on the temperature, this also changes the signal phase. It was shown that heat diffusion through the fiber cladding has to be considered as well, because it influences the dynamic properties of this effect. It was found that heat can be the dominant contribution to the signal phase and it was shown how its dynamic depends on the fiber geometry.

The prospects of coherent beam combining for laser systems for gravitational wave detectors were analyzed in an additional experiment. Two fiber amplifiers with an output power of 10 W each were combined with diffraction limited beam quality and preserved relative power noise and frequency noise. According to these experiments, the requirements for a suitable CBC control loop are very moderate. Therefore, coherent beam combining is a very promising power scaling method to reach the high power levels required for 3rd generation gravitational wave detectors.

Since fiber amplifiers influence the optical phase, they can also be used as phase actuators. This was demonstrated using an erbium doped fiber amplifier for all-fiber coherent beam combining at 1064 nm. Relative phase control of two ytterbium fiber amplifiers was even realized by using these ytterbium fiber amplifiers as phase actuators and amplifiers at the same time. Even in this configuration, a combining efficiency better than 95% was maintained for several minutes. A longterm stable all-fiber system using fiber stretchers as phase actuators was also demonstrated.

Overall, single frequency fiber amplifiers are a very promising laser concept for future gravitational wave detectors. So far, the main focus in the development of single frequency fiber amplifiers was on the power scaling and diffraction limited beam quality. However, the dynamic properties are equally important when regarding the use in GWDs. Here, several essential steps towards the use of fiber amplifiers in gravitational wave detectors were realized: the dynamic influence of pump and seed power fluctuations on the signal power and the signal phase – including the underlying physical processes such as gain dynamics in fiber amplifiers and heat diffusion in the fiber – are now well understood and therefore an effective stabilization is feasible. Furthermore, it could be shown that the beam quality and noise properties can be preserved when using coherent beam combining as a power scaling method. This enables output power levels beyond the single amplifier limitations which could be necessary for 3rd generation gravitational wave detectors.

10 Outlook

Single frequency fiber amplifiers enable high power high efficiency laser sources at reasonable system complexity. These advantages make them very attractive as laser sources for GWDs. However, a single frequency fiber amplifier meeting both the long term stability and output power of the advanced LIGO laser system has yet to be demonstrated. Such a fiber amplifier is already in development and once this system is sufficiently stable, noise characterization will be the obvious next step. Eventually, this system will also be power and phase stabilized. Active stabilization using pump diodes and the seed laser power is possible with the help of the transfer functions for seed and pump power fluctuations. Therefore, it should be possible to stabilize this system very efficiently. At this point a fiber based system surpassing the advanced LIGO laser will exist, but at a fraction of the cost, space and with a much higher efficiency.

Of course, the main challenge is not to replicate the advanced LIGO laser system, but the development of suitable sources for 3rd generation GWDs. With this in mind there are several important topics related to the temporal dynamics of fiber amplifiers which should be investigated in the future.

Mode fluctuations

For power scaling of large mode area fibers modal instabilities are now the most limiting effect. In single frequency fiber amplifiers the large mode area is required to suppress stimulated Brillouin scattering. But especially these few mode LMA fibers are prone to modal instabilities. Modal instabilities are a dynamic effect caused by the heat deposited in the fiber. The dynamic nature of the effect can be shown by introducing a pinhole into the beam of the fiber amplifier. This converts

the mode fluctuations into power noise. Above the modal instability threshold, a massive power noise increase can be observed (Fig. 10.1, [41]). Alternatively, the beam profile can be observed with a high speed camera [41].

Therefore, a deeper understanding of dynamic thermal effects in fiber amplifiers is not only desirable because of phase noise but also for power scaling. For modal instabilities the heat flow in z direction is most important. However, the results from radial heat flow can estimate up to which frequencies significant temperature fluctuations can be supported by the fiber. The mode cleaning cavity, which was originally designed to filter the modes entering a gravitational wave detector, could be used for real time analysis of the fundamental mode fraction. However, obtaining a sufficiently high measurement bandwidth and avoiding pointing are challenges which will have to be overcome to use these cavities for this purpose.

Erbium and Thulium

Besides the power scaling at 1064 nm, wavelengths beyond 1064 nm are in discussion for 3rd generation gravitational wave detectors. The corresponding dopants are

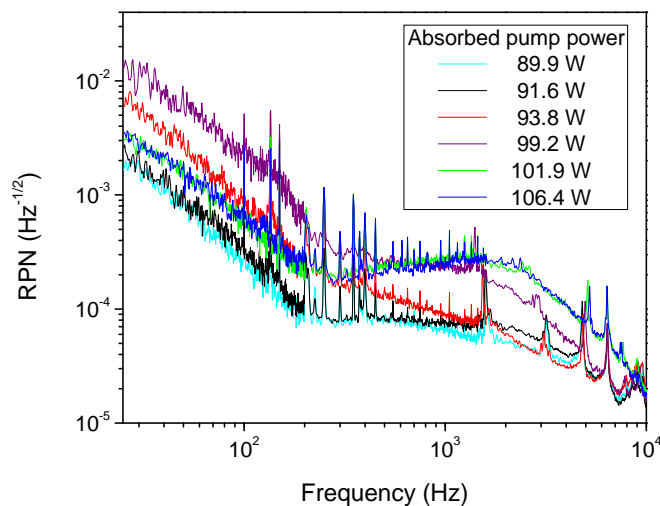


Figure 10.1: Modal instabilities converted to RPN using a pinhole. For this amplifier the threshold was at about 94 W of absorbed pump power.

erbium, erbium-ytterbium and thulium. For example erbium-ytterbium co-doped fibers could show more complex dynamic behavior due to the additional energy transfer from the ytterbium to erbium ions. Furthermore, it has been shown that the performance of erbium-ytterbium co-doped fibers can be improved by introducing a 1064 nm co-seed [88]. The induced phase shift due to the gain of ytterbium ions has yet to be analyzed as well. In this case the 1064 nm co-seed could be modulated to imprint phase shifts on the 1550 nm signal.

The limitations of such systems at high power are not clear yet, as previous erbium fiber amplifiers were limited by efficiency and available pump power [89]. Due to the high thermal load, the modal instability threshold could occur quite soon. While this would be a severe limitation on the power scalability of such systems, it would also offer possibilities to re-evaluate the lessons learned about modal instabilities from ytterbium doped fibers.

High Power CBC

Although further power scaling of single amplifiers is an important topic, it is possibly not sufficient for the realization of the laser systems for third generation GWDs. However, as shown in this thesis, it is possible to combine multiple beams to a single mode single frequency output beam with noise properties identical to the individual free running laser systems. For an actual kilowatt class system four 300 W class fiber amplifiers will have to be combined.

The main challenges remaining here are the combination of more than two beams and the fact that the beam quality can be slightly worse compared to single mode fibers. However, this does not seem to be a major issue as more than two beams have already been coherently combined [29] and even CBC of rod type fibers has shown to be possible with good combining efficiency [48]. Regardless of the fact that power scaling using CBC might seem straightforward, the actual realization of such a system will be challenging technologically.

With this in mind, it is pretty clear that fiber amplifiers and especially their dynamic properties will remain an exciting field in the future.

Bibliography

- [1] G. Harry, “Advanced LIGO: the next generation of gravitational wave detectors,” *Classical and Quantum Gravity* **27**, 084006 (2010).
- [2] K. Kuroda, “Status of LCGT,” *Classical and Quantum Gravity* **27**, 084004 (2010).
- [3] L. Winkelmann, O. Puncken, R. Kluzik, C. Veltkamp, P. Kwee, J. Poeld, C. Bogan, B. Willke, M. Frede, J. Neumann, P. Wessels, and D. Kracht, “Injection-locked single-frequency laser with an output power of 220 W,” *Applied Physics B: Lasers and Optics* **102**(3), 529–538 (2011).
- [4] P. Kwee, C. Bogan, K. Danzmann, M. Frede, H. Kim, P. King, J. Pöld, O. Puncken, R. Savage, F. Seifert, P. Wessels, L. Winkelmann, and B. Willke, “Stabilized high-power laser system for the gravitational wave detector advanced LIGO,” *Optics Express* **20**(10), 10617–10634 (2012).
- [5] M. Abernathy, F. Acernese, P. Ajith, B. Allen, P. Amaro-Seoane, N. Andersson, S. Aoudia, P. Astone, B. Krishnan, *et al.*, “Einstein gravitational wave Telescope conceptual design study,” (2011). Available online at <http://www.et-gw.eu/etdsdocument>.
- [6] M. Punturo, M. Abernathy, F. Acernese, B. Allen, N. Andersson, K. Arun, F. Barone, B. Barr, M. Barsuglia, M. Beker, *et al.*, “The Einstein Telescope: a third-generation gravitational wave observatory,” *Classical and Quantum Gravity* **27**, 194002 (2010).
- [7] R. Drever, J. Hall, F. Kowalski, J. Hough, G. Ford, A. Munley, and H. Ward, “Laser phase and frequency stabilization using an optical resonator,” *Applied Physics B: Lasers and Optics* **31**(2), 97–105 (1983).
- [8] E. Black, “An introduction to Pound–Drever–Hall laser frequency stabilization,” *American Journal of Physics* **69**, 79 (2001).

- [9] I. Zawischa, M. Brendel, K. Danzmann, C. Fallnich, M. Heurs, S. Nagano, V. Quetschke, H. Welling, and B. Willke, “The GEO 600 laser system,” *Classical and Quantum Gravity* **19**, 1775 (2002).
- [10] M. Frede, R. Wilhelm, M. Brendel, C. Fallnich, F. Seifert, B. Willke, and K. Danzmann, “High power fundamental mode Nd:YAG laser with efficient birefringence compensation,” *Optics Express* **12**(15), 3581–3589 (2004).
- [11] M. Frede, B. Schulz, R. Wilhelm, P. Kwee, F. Seifert, B. Willke, and D. Kracht, “Fundamental mode, single-frequency laser amplifier for gravitational wave detectors,” *Optics Express* **15**(2), 459–465 (2007).
- [12] C. Basu, P. Weßels, J. Neumann, and D. Kracht, “High power single frequency solid state master oscillator power amplifier for gravitational wave detection,” *Optics Letters* **37**(14), 2862–2864 (2012).
- [13] M. Karow, C. Basu, D. Kracht, J. Neumann, and P. Weßels, “TEM₀₀ mode content of a two stage single-frequency Yb-doped PCF MOPA with 246 W of output power,” *Optics Express* **20**(5), 5319–5324 (2012).
- [14] T. Theeg, H. Sayinc, J. Neumann, and D. Kracht, “All-fiber counter-propagation pumped single frequency amplifier stage with 300 W output power,” *Photonics Technology Letters* **24**(20), 1864–1867 (2012).
- [15] M. Tröbs, P. Wessels, and C. Fallnich, “Power-and frequency-noise characteristics of an Yb-doped fiber amplifier and actuators for stabilization,” *Optics Express* **13**(6), 2224–2235 (2005).
- [16] S. Novak and A. Moesle, “Analytic model for gain modulation in EDFAs,” *Journal of Lightwave Technology* **20**(6), 975 (2002).
- [17] M. Tröbs, P. Wessels, and C. Fallnich, “Phase-noise properties of an ytterbium-doped fiber amplifier for the Laser Interferometer Space Antenna,” *Optics Letters* **30**(7), 789–791 (2005).
- [18] M. Digonnet, R. Sadowski, H. Shaw, and R. Pantell, “Experimental evidence for strong UV transition contribution in the resonant nonlinearity of doped fibers,” *Journal of Lightwave Technology* **15**(2), 299–303 (1997).
- [19] M. Davis, M. Digonnet, and R. Pantell, “Thermal effects in doped fibers,” *Journal of Lightwave Technology* **16**(6), 1013–1023 (1998).

- [20] A. Fotiadi, O. Antipov, and P. Mégret, “Dynamics of pump-induced refractive index changes in single-mode Yb-doped optical fibers,” *Optics Express* **16**(17), 12658–12663 (2008).
- [21] I. Zawischa, K. Plamann, C. Fallnich, H. Welling, H. Zellmer, and A. Tünnermann, “All-solid-state neodymium-based single-frequency master-oscillator fiber power-amplifier system emitting 5.5 W of radiation at 1064 nm,” *Optics Letters* **24**(7), 469–471 (1999).
- [22] S. Höfer, A. Liem, J. Limpert, H. Zellmer, A. Tünnermann, S. Unger, S. Jetschke, H. Müller, and I. Freitag, “Single-frequency master-oscillator fiber power amplifier system emitting 20 W of power,” *Optics Letters* **26**(17), 1326–1328 (2001).
- [23] A. Liem, J. Limpert, H. Zellmer, and A. Tünnermann, “100-W single-frequency master-oscillator fiber power amplifier,” *Optics Letters* **28**(17), 1537–1539 (2003).
- [24] Y. Jeong, J. Nilsson, J. Sahu, D. Soh, C. Alegria, P. Dupriez, C. Codemard, D. Payne, R. Horley, L. Hickey, L. Wanzcyk, C. E. Chryssou, J. A. Alvarez-Chavez, and P. W. Turner, “Single-frequency, single-mode, plane-polarized ytterbium-doped fiber master oscillator power amplifier source with 264 W of output power,” *Optics Letters* **30**(5), 459–461 (2005).
- [25] Y. Jeong, J. Nilsson, J. Sahu, D. Payne, R. Horley, L. Hickey, and P. Turner, “Power scaling of single-frequency ytterbium-doped fiber master-oscillator power-amplifier sources up to 500 W,” *Selected Topics in IEEE Journal of Quantum Electronics* **13**(3), 546–551 (2007).
- [26] S. Gray, A. Liu, D. Walton, J. Wang, M. Li, X. Chen, A. Ruffin, J. DeMeritt, and L. Zenteno, “502 Watt, single transverse mode, narrow linewidth, bidirectionally pumped Yb-doped fiber amplifier,” *Optics Express* **15**(25), 17044–17050 (2007).
- [27] C. Robin, I. Dajani, C. Vergien, C. Zeringue, and T. Shay, “Experimental and theoretical studies of single frequency PCF amplifier with output of 400 W,” in *Proceedings of SPIE*, vol. 7580, p. 75801I (2010).
- [28] C. Zhu, I. Hu, X. Ma, L. Siiman, and A. Galvanauskas, “Single-frequency and single-transverse mode Yb-doped CCC fiber MOPA with robust polarization SBS-free 511W output,” in *Advanced Solid-State Photonics* (Optical Society of America, 2011).

- [29] A. Flores, T. Shay, C. Lu, C. Robin, B. Pulford, A. Sanchez, D. Hult, and K. Rowland, “Coherent beam combining of fiber amplifiers in a kW regime,” in *2011 Conference on Lasers and Electro-Optics (CLEO)* (IEEE, 2011).
- [30] D. Gapontsev and I. Photonics, “6kW CW Single mode Ytterbium fiber laser in all-fiber format,” *Solid State and Diode Laser Technology Review* (2008).
- [31] R. Boyd, *Nonlinear optics* (Academic Press, 2003).
- [32] P. Weßels and C. Fallnich, “Highly sensitive beam quality measurements on large-mode-area fiber amplifiers,” *Optics Express* **11**(25), 3346 (2003).
- [33] Y. Feng, L. Taylor, and D. Calia, “25 W Raman-fiber-amplifier-based 589 nm laser for laser guide star,” *Optics Express* **17**(21), 19021–19026 (2009).
- [34] Y. Feng, L. Zhang, J. Wang, and J. Hu, “Single frequency and mode-locked Raman fiber lasers,” in *8th Asia Pacific Laser Symposium (SIOM, 2012)*.
- [35] M. Chen, A. Shirakawa, X. Fan, K. Ueda, C. Olausson, J. Lyngsø, and J. Broeng, “Single-frequency ytterbium doped photonic bandgap fiber amplifier at 1178 nm,” *Optics Express* **20**(19), 21044–21052 (2012).
- [36] C. Robin and I. Dajani, “Acoustically segmented photonic crystal fiber for single-frequency high-power laser applications,” *Optics Letters* **36**(14), 2641–2643 (2011).
- [37] M. Hildebrandt, “Brillouin scattering in high-power narrow-linewidth fiber amplifiers,” Ph.D. thesis, Leibniz Universität Hannover (2009).
- [38] F. Jansen, F. Stutzki, H. Otto, T. Eidam, A. Liem, C. Jauregui, J. Limpert, and A. Tünnermann, “Thermally induced waveguide changes in active fibers,” *Optics Express* **20**(4), 3997–4008 (2012).
- [39] K. Hansen, T. Alkeskjold, J. Broeng, and J. Lægsgaard, “Thermo-optical effects in high-power ytterbium-doped fiber amplifiers,” *Optics Express* **19**(24), 23965–23980 (2011).
- [40] T. Eidam, C. Wirth, C. Jauregui, F. Stutzki, F. Jansen, H. Otto, O. Schmidt, T. Schreiber, J. Limpert, and A. Tünnermann, “Experimental observations of the threshold-like onset of mode instabilities in high power fiber amplifiers,” *Optics Express* **19**(14), 13218–13224 (2011).

- [41] H. Otto, F. Stutzki, F. Jansen, T. Eidam, C. Jauregui, J. Limpert, and A. Tünnermann, “Temporal dynamics of mode instabilities in high-power fiber lasers and amplifiers,” *Optics Express* **20**(14), 15710–15722 (2012).
- [42] N. Haarlammert, O. de Vries, A. Liem, A. Kliner, T. Peschel, T. Schreiber, R. Eberhardt, and A. Tünnermann, “Build up and decay of mode instability in a high power fiber amplifier,” *Optics Express* **20**(12), 13274–13283 (2012).
- [43] A. Smith and J. Smith, “Mode instability in high power fiber amplifiers,” *Optics Express* **19**(11), 10180–10192 (2011).
- [44] C. Jauregui, T. Eidam, H. Otto, F. Stutzki, F. Jansen, J. Limpert, and A. Tünnermann, “Temperature-induced index gratings and their impact on mode instabilities in high-power fiber laser systems,” *Optics Express* **20**(1), 440–451 (2012).
- [45] C. Jauregui, T. Eidam, H. Otto, F. Stutzki, F. Jansen, J. Limpert, and A. Tünnermann, “Physical origin of mode instabilities in high-power fiber laser systems,” *Optics Express* **20**(12), 12912–12925 (2012).
- [46] B. Ward, C. Robin, and I. Dajani, “Origin of thermal modal instabilities in large mode area fiber amplifiers,” *Optics Express* **20**(10), 11407–11422 (2012).
- [47] G. Goodno, L. Book, and J. Rothenberg, “Low-phase-noise, single-frequency, single-mode 608 W thulium fiber amplifier,” *Optics Letters* **34**(8), 1204–1206 (2009).
- [48] L. Daniault, M. Hanna, D. Papadopoulos, Y. Zaouter, E. Mottay, F. Druon, and P. Georges, “High peak-power stretcher-free femtosecond fiber amplifier using passive spatio-temporal coherent combining,” *Optics Express* **20**(19), 21627–21634 (2012).
- [49] G. Goodno, C. Shih, and J. Rothenberg, “Perturbative analysis of coherent combining efficiency with mismatched lasers,” *Optics Express* **18**(24), 25403–25414 (2010).
- [50] S. Augst, T. Fan, and A. Sanchez, “Coherent beam combining and phase noise measurements of ytterbium fiber amplifiers,” *Optics Letters* **29**(5), 474–476 (2004).
- [51] C. Yu, S. Augst, S. Redmond, K. Goldizen, D. Murphy, A. Sanchez, and T. Fan, “Coherent combining of a 4 kW, eight-element fiber amplifier array,” *Optics Letters* **36**(14), 2686–2688 (2011).

- [52] P. Zhou, Z. Liu, X. Wang, Y. Ma, H. Ma, X. Xu, and S. Guo, "Coherent beam combining of fiber amplifiers using stochastic parallel gradient descent algorithm and its application," *IEEE Journal of Selected Topics in Quantum Electronics* **15**(2), 248–256 (2009).
- [53] E. Cheung, J. Ho, G. Goodno, R. Rice, J. Rothenberg, P. Thielen, M. Weber, and M. Wickham, "Diffractive-optics-based beam combination of a phase-locked fiber laser array," *Optics Letters* **33**(4), 354–356 (2008).
- [54] R. Uberna, A. Bratcher, T. Alley, A. Sanchez, A. Flores, and B. Pulford, "Coherent combination of high power fiber amplifiers in a two-dimensional re-imaging waveguide," *Optics Express* **18**(13), 13547–13553 (2010).
- [55] T. Fan, "Laser beam combining for high-power, high-radiance sources," *Selected Topics in IEEE Journal of Quantum Electronics* **11**(3), 567–577 (2005).
- [56] G. Goodno, C. Asman, J. Anderegg, S. Brosnan, E. Cheung, D. Hammons, H. Injeyan, H. Komine, W. Long, M. McClellan, S. McNaught, S. Redmond, R. Simpson, J. Sollee, M. Weber, S. Weiss, and M. Wickham, "Brightness-scaling potential of actively phase-locked solid-state laser arrays," *Selected Topics in IEEE Journal of Quantum Electronics* **13**(3), 460–472 (2007).
- [57] E. Seise, A. Klenke, J. Limpert, and A. Tünnermann, "Coherent addition of fiber-amplified ultrashort laser pulses," *Optics Express* **18**(26), 27827–27835 (2010).
- [58] L. Daniault, M. Hanna, L. Lombard, Y. Zaouter, E. Mottay, D. Goular, P. Bourdon, F. Druon, and P. Georges, "Coherent beam combining of two femtosecond fiber chirped-pulse amplifiers," *Optics Letters* **36**(5), 621–623 (2011).
- [59] L. Siiman, W. Chang, T. Zhou, and A. Galvanauskas, "Coherent femtosecond pulse combining of multiple parallel chirped pulse fiber amplifiers," *Optics Express* **20**(16), 18097–18116 (2012).
- [60] C. Giles and E. Desurvire, "Propagation of signal and noise in concatenated erbium-doped fiber optical amplifiers," *Journal of Lightwave Technology* **9**(2), 147–154 (1991).
- [61] A. Bononi and L. Rusch, "Doped-fiber amplifier dynamics: A system perspective," *Journal of Lightwave Technology* **16**(5), 945–956 (1998).

- [62] J. Jou and C. Liu, “Equivalent circuit model for erbium-doped fibre amplifiers including amplified spontaneous emission,” *Optoelectronics, IET* **2**(1), 29–33 (2008).
- [63] O. Puncken, “Pumpkopfdesign für den Advanced LIGO Laser,” Ph.D. thesis, Leibniz Universität Hannover (2011).
- [64] C. Ottenhues, “Untersuchung zur Stimulierten Brillouin Streuung in einem Ytterbium dotierten longitudinal und transversal einmodigen Faserverstärkersystem,” (2011). Bachelor thesis.
- [65] M. Digonnet, R. Sadowski, H. Shaw, and R. Pantell, “Resonantly enhanced nonlinearity in doped fibers for low-power all-optical switching: A review,” *Optical Fiber Technology* **3**(1), 44–64 (1997).
- [66] A. Fotiadi, N. Zakharov, O. Antipov, and P. Mégret, “All-fiber coherent combining of Er-doped amplifiers through refractive index control in Yb-doped fibers,” *Optics Letters* **34**(22), 3574–3576 (2009).
- [67] B. Saleh, M. Teich, and B. Saleh, *Fundamentals of Photonics*, vol. 22 (Wiley New York, 1991).
- [68] R. Kronig, “On the theory of dispersion of x-rays,” *Journal of the Optical Society of America* **12**(6), 547–556 (1926).
- [69] R. Pantell, M. Digonnet, R. Sadowski, and H. Shaw, “Analysis of nonlinear optical switching in an erbium-doped fiber,” *Journal of Lightwave Technology* **11**(9), 1416–1424 (1993).
- [70] J. Arkwright, P. Elango, G. Atkins, T. Whitbread, and M. Digonnet, “Experimental and theoretical analysis of the resonant nonlinearity in ytterbium-doped fiber,” *Journal of Lightwave Technology* **16**(5), 798 (1998).
- [71] A. Fotiadi, O. Antipov, and P. Mégret, “All-fiber coherent Combining of Er-doped amplifiers via refractive index control in Yb-doped fibers by two-wavelengths optical signal,” in *CLEO Europe-EQEC 2009* (IEEE, 2009).
- [72] W. Clarkson, “Thermal effects and their mitigation in end-pumped solid-state lasers,” *Journal of Physics D: Applied Physics* **34**, 2381 (2001).
- [73] D. Brown, “Heat, fluorescence, and stimulated-emission power densities and fractions in Nd:YAG,” *IEEE Journal of Quantum Electronics* **34**(3), 560–572 (1998).

- [74] D. Brown and H. Hoffman, "Thermal, stress, and thermo-optic effects in high average power double-clad silica fiber lasers," *IEEE Journal of Quantum Electronics* **37**(2), 207–217 (2001).
- [75] M. Davis and M. Digonnet, "Measurements of thermal effects in fibers doped with cobalt and vanadium," *Journal of Lightwave Technology* **18**(2), 161–165 (2000).
- [76] J. Guyer, D. Wheeler, and J. Warren, "Fipy: Partial differential equations with python," *Computing in Science & Engineering* **11**(3), 6–15 (2009).
- [77] A. Smith and J. Smith, "Influence of pump and seed modulation on the mode instability thresholds of fiber amplifiers," *Optics Express* **20**(22), 24545–24558 (2012).
- [78] S. Augst, J. Ranka, T. Fan, and A. Sanchez, "Beam combining of ytterbium fiber amplifiers," *Journal of the Optical Society of America B* **24**(8), 1707–1715 (2007).
- [79] T. Shay, V. Benham, J. Baker, B. Ward, A. Sanchez, M. Culpepper, D. Pilkington, J. Spring, D. Nelson, and C. Lu, "First experimental demonstration of self-synchronous phase locking of an optical array," *Optics Express* **14**(25), 12015–12021 (2006).
- [80] G. Goodno, S. McNaught, J. Rothenberg, T. McComb, P. Thielen, M. Wickham, and M. Weber, "Active phase and polarization locking of a 1.4 kW fiber amplifier," *Optics Letters* **35**(10), 1542–1544 (2010).
- [81] M. Musha, T. Kanaya, K. Nakagawa, and K. Ueda, "Intensity and frequency noise characteristics of two coherently-added injection-locked Nd:YAG lasers," *Applied Physics B: Lasers and Optics* **73**(3), 209–214 (2001).
- [82] L. Taylor, Y. Feng, and D. Calia, "50W CW visible laser source at 589nm obtained via frequency doubling of three coherently combined narrow-band Raman fibre amplifiers," *Optics Express* **18**(8), 8540–8555 (2010).
- [83] P. Kwee, F. Seifert, B. Willke, and K. Danzmann, "Laser beam quality and pointing measurement with an optical resonator," *Review of Scientific Instruments* **78**(7), 073103–073103 (2007).
- [84] P. Kwee, "Laser Characterization and Stabilization for Precision Interferometry," Ph.D. thesis, Leibniz Universität Hannover (2010).

-
- [85] M. Heurs, V. Quetschke, B. Willke, K. Danzmann, and I. Freitag, “Simultaneously suppressing frequency and intensity noise in a Nd:YAG nonplanar ring oscillator by means of the current-lock technique,” *Optics Letters* **29**(18), 2148–2150 (2004).
- [86] T. Theeg, K. Hausmann, M. Frede, H. Sayinc, J. Neumann, and D. Kracht, “High power fused single mode optical fiber coupler,” in *The European Conference on Lasers and Electro-Optics* (Optical Society of America, 2011).
- [87] M. Minden, “Phase control mechanism for coherent fiber amplifier arrays,” (2002). US Patent 6,400,871.
- [88] V. Kuhn, P. Weßels, J. Neumann, and D. Kracht, “Stabilization and power scaling of cladding pumped Er:Yb-codoped fiber amplifier via auxiliary signal at 1064 nm,” *Optics Express* **17**(20), 18304–18311 (2009).
- [89] V. Kuhn, D. Kracht, J. Neumann, and P. Weßels, “Er-doped photonic crystal fiber amplifier with 70 W of output power,” *Optics Letters* **36**(16), 3030–3032 (2011).

Publications in Peer-Reviewed Journals

- [90] O. Puncken, H. Tünnermann, J. Morehead, P. Weßels, M. Frede, J. Neumann, and D. Kracht, “Intrinsic reduction of the depolarization in Nd:YAG crystals,” *Optics Express* **18**(19), 20461–20474 (2010).
- [91] H. Tünnermann, J. Neumann, D. Kracht, and P. Weßels, “All-fiber phase actuator based on an erbium-doped fiber amplifier for coherent beam combining at 1064 nm,” *Optics letters* **36**(4), 448–450 (2011).
- [92] H. Tünnermann, O. Puncken, P. Weßels, M. Frede, J. Neumann, and D. Kracht, “Linearly polarized single-mode Nd:YAG oscillators using [100]-and [110]-cut crystals,” *Optics Express* **19**(14), 12992–12999 (2011).
- [93] H. Tünnermann, J. Pöld, J. Neumann, D. Kracht, B. Willke, and P. Weßels, “Beam quality and noise properties of coherently combined ytterbium doped single frequency fiber amplifiers,” *Optics Express* **19**(20), 19600–19606 (2011).
- [94] H. Tünnermann, Y. Feng, J. Neumann, D. Kracht, and P. Weßels, “All-fiber coherent beam combining with phase stabilization via differential pump power control,” *Optics Letters* **37**(7), 1202–1204 (2012).
- [95] H. Tünnermann, J. Neumann, D. Kracht, and P. Weßels, “Gain dynamics and refractive index changes in fiber amplifiers: a frequency domain approach,” *Optics Express* **20**(12), 13539–13550 (2012).
- [96] H. Tünnermann, J. Neumann, D. Kracht, and P. Weßels, “Frequency resolved analysis of thermally induced refractive index changes in fiber amplifiers,” *Optics Letters* **37**(17), 3597–3599 (2012).
- [97] M. Karow, H. Tünnermann, J. Neumann, D. Kracht, and P. Weßels, “Beam quality degradation of a single-frequency Yb-doped photonic crystal fiber amplifier with low mode instability threshold power,” *Optics Letters* **37**(20), 4242–4244 (2012).

Publications in Conference Proceedings

- [98] H. Tünnermann, O. Puncken, P. Weßels, M. Frede, D. Kracht, and J. Neumann, “Intrinsische Reduktion von Depolarisationsverlusten in Nd:YAG Kristallen,” in *DPG Frühjahrestagung* (Deutsche Physikalische Gesellschaft, 2009).
- [99] H. Tünnermann, O. Puncken, P. Weßels, M. Frede, D. Kracht, and J. Neumann, “Intrinsic Reduction of the Depolarization in Nd:YAG Crystals,” in *Advanced Solid-State Photonics* (Optical Society of America, 2010).
- [100] H. Tünnermann, J. Neumann, D. Kracht, and P. Wessels, “Coherent Beam Combining at 1064 nm Employing an Erbium Doped Fiber Amplifier for Phase Control,” in *Advanced Solid-State Photonics* (Optical Society of America, 2011).
- [101] H. Tünnermann, J. Pödl, J. Neumann, D. Kracht, B. Willke, and P. Weßels, “Collinear Coherent Beam Combining of Two Ytterbium Doped Single Frequency Fiber Amplifiers,” in *CLEO: Science and Innovations* (Optical Society of America, 2011).
- [102] H. Tünnermann, J. Neumann, D. Kracht, and P. Weßels, “Frequency domain analysis of dynamic refractive index changes in fiber amplifiers,” in *Photonics West* (SPIE, 2012).
- [103] H. Tünnermann, T. Theeg, K. Hausmann, J. Neumann, D. Kracht, and P. Wessels, “All-fiber Coherent Beam Combining of Two Ytterbium Doped Single Frequency Fiber Amplifiers,” in *Advanced Solid-State Photonics* (Optical Society of America, 2012).
- [104] H. Tünnermann, Y. Feng, T. Theeg, K. Hausmann, J. Neumann, D. Kracht, and P. Wessels, “All-fiber Coherent Beam Combining of Two Ytterbium Doped Single Frequency Fiber Amplifiers,” in *8th Asia Pacific Laser Symposium* (SIOM, 2012).
- [105] H. Tünnermann, J. Neumann, D. Kracht, and P. Wessels, “Temperature Induced Dynamic Refractive Changes in Fiber Amplifiers,” in *Europhoton* (European Physical Society, 2012).

- [106] M. Karow, H. Tünnermann, J. Neumann, D. Kracht, and P. Wessels, “Beam quality degradation of a strongly pumped Yb-doped photonic crystal fiber amplifier,” in *Europhoton* (European Physical Society, 2012).

Curriculum Vitae

Personal Data

Name Henrik Tünnermann
Date of birth 06.12.1984
Place of birth Hannover

Education

1991 - 1995 Grundschule Bonner Straße
1995 - 1997 Geschwister-Jacobs-Schule
1997 - 2004 Elsa-Brandström-Schule

University Education

10/2004 - 10/2009 Physics, Leibniz Universität Hannover
10/2009 Diploma with distinction, thesis title
 Intrinsische Reduktion der Depolarisation in Nd:YAG
 Kristallen

Professional Affiliations

2006 - 2008 Teaching assistant at Institute for Theoretical Physics
 Leibniz Universität Hannover
09/2008 - present Laser development, Laser Zentrum Hannover e.V.
04/2012 - 06/2012 Researcher at Institute for Laser Science
 University of Electro Communications, Tokyo, Japan

 Reviewer for Optics Express (Optical Society of America)
 Reviewer for Optics Communications (Elsevier)
 Member of Optical Society of America (OSA)
 Member of Deutsche Physikalische Gesellschaft (DPG)

Scholarships and Awards

10/2009 - 09/2012 HALOSTAR scholarship

Acknowledgements

First I would like to thank Prof. Karsten Danzmann for the supervision of my work and the coordination of the HALOSTAR program. Furthermore I'd like to thank Prof. Karsten Danzmann, Prof. Uwe Morgner, Prof. Akira Shirakawa, Prof. Detlev Ristau, and Prof. Milutin Kovacev for the evaluation of my work.

Special thanks go to Peter Weßels, for many discussions about results, possible conclusions, and valuable feedback.

I'd like to take this chance to thank Mingchen Chen, Xinyan Fan, Prof. Yan Feng, Katharina Hausmann, Malte Karow, Hiroaki Nakao, Jan Hendrik Pöld, Oliver Puncken, Thomas Theeg, Hans Wilke, and Benno Willke.

Additional thanks go to Jörg Neumann and Dietmar Kracht for ensuring a good working environment and all the other colleagues in the Laser Zentrum Hannover. Finally I'd like to thank my family and friends for their support.

These three years have been a fantastic experience which would not have been possible without your support. Thank you!